technische universität
dortmund

Development and Fabrication of Functional Layers for Cardiac Biosensor Application

Vorgelegt in der Fakultät Physik der Technishe Universität Dortmund zur Erlangung des akademischen Grades eines Doktors der Naturwissenschaften

von
Master of Science

Hanna Hlukhova

aus Kharkiv, Ukraine

2019

Gutachter 1: Prof. Dr. Svetlana Vitusevich

Gutachter 2: Prof. Dr. Dmitry Yakovlev

Vorsitzender der Prüfungskommission: Prof. Dr. Götz Uhrig

Vertreterin der wissenschaftlichen Mitarbeiter: Dr. Gerald Schmidt

Tag der mündlichen Prüfung:: 02. July 2019

Abstract

In this work, several types of biosensors are fabricated, characterized, and utilized for the reliable and accurate detection of specific biomolecules that playing a crucial role in biochemical processes inside the human organism. During the work, different types of biosensing techniques, including whispering-gallery-mode (WGM) resonators and field-effect transistors (FETs), as well as electrolyte-insulator-semiconductor (EIS) sensors were introduced and used as highly sensitive tools to study a set of biomolecules that are of particular interest for the understanding of heart dysfunctions and for cardiac disease diagnosis.

A whispering–gallery–mode resonator with Zeonex-based microfluidic channel was designed for complex permittivity measurements of biological and chemical liquids. The WGM technique allows to obtain a distinct difference of resonance characteristics between calibration liquids: water, acetone, methanol, ethanol, and propanol in the fluidic chamber. Moreover, high sensitivity detection was achieved in the study of the system's response to aqueous solutions of glutathione and ascorbate, the two most important antioxidant-specific biomarkers, with concentrations down to 10 μg/L.

The capacitive electrolyte-insulator-semiconductor sensors, where silicon is covered with a thin dielectric layer is exposed to liquid analyte solution, represents a reproducible and extremely sensitive technique. Robust surface modification protocols have been developed for the immobilization of specific antibodies onto the topmost ultra-thin silicon dioxide layer, consequently attributing to the C-reactive protein (CRP) and Troponin biomarkers with different concentrations down to 1 μg/L. Moreover, the introduction of aptamers, instead of antibodies, onto the surface of EIS biosensors allowed to demonstrate an extremely high sensitivity to biomarkers with concentrations down to 0.01 μg/L.

Field-effect transistor-based biosensors, including those made of silicon and graphene, have also been used to study the C-reactive protein molecules as well as Troponin-I molecules with concentrations down to 0.1 μg/L. The reusability of silicon-based

FET biosensors was shown to be of great advantage for biosensing. Meanwhile, graphene-based FETs have been successfully used to study the dynamic processes during the induced cardiac ischemia arrest in HL-1 cell culture, grown in the reservoir, directly on top of the chip. The findings open prospects for the detection of ischemia at early stages, and monitoring of cardiac disease development *in vivo*. Application of graphene material is essential for the development of such kind of biosensing devices, since they can be easily fabricated in the form of flexible and even stretchable devices for utilization as implantable structures into living tissue.

Zusammenfassung

In dieser Arbeit werden verschiedene Arten von Biosensoren hergestellt, charakterisiert und für den zuverlässigen und genauen Nachweis spezifischer Biomoleküle verwendet, die eine entscheidende Rolle bei biochemischen Prozessen im menschlichen Organismus spielen. Während der Arbeit wurden verschiedene Arten von Biosensortechniken, darunter Whispering-Gallery-Mode (WGM) Resonatoren und Feldeffekttransistoren (FETs) sowie Elektrolyt-Isolator-Halbleiter (EIS) Sensoren eingeführt und als hochempfindliche Werkzeuge eingesetzt, um eine Reihe von Biomolekülen zu untersuchen, die für das Verständnis von Herzstörungen und die Diagnose von Herzerkrankungen besonders interessant sind.

Ein Flüsternde-Galerie-Modus-Resonator mit Zeonex-basiertem Mikrofluidikkanal wurde für komplexe Permittivitätsmessungen von biologischen und chemischen Flüssigkeiten entwickelt. Die WGM-Technik ermöglicht es, eine deutliche Differenz der Resonanzeigenschaften als Reaktion auf die eingeführten Kalibrierflüssigkeiten: Wasser, Aceton, Methanol, Ethanol und Propanol in der Fluidkammer zu erhalten. Darüber hinaus wurde ein hochempfindlicher Nachweis in der Untersuchung der Reaktion des Systems auf wässrige Lösungen von Glutathion und Ascorbat, den beiden wichtigsten antioxidanspezifischen Biomarkern mit Konzentrationen bis zu 10 µg/L, erzielt.

Die kapazitiven Elektrolyt-Isolator-Halbleitersensoren, bei denen Silizium mit einer dünnen dielektrischen Schicht bedeckt ist und einer flüssigen Analytenlösung ausgesetzt ist, stellen eine reproduzierbare und extrem empfindliche Technik dar. Für die Immobilisierung spezifischer Antikörper auf der obersten ultradünnen Siliziumdioxidschicht wurden robuste Oberflächenmodifikationsprotokolle entwickelt, die auf das C-reaktive Protein (CRP) und die Troponin-Biomarker mit unterschiedlichen Konzentrationen bis zu 1 µg/L zurückgeführt werden. Darüber hinaus konnte durch die Einführung von Aptameren anstelle von Antikörpern auf die Oberfläche von EIS-Biosensoren eine extrem hohe Sensitivität gegenüber Biomarkern mit Konzentrationen bis zu 0.01 µg/L nachweisen werden.

Biosensoren auf Basis von Feldeffekttransistoren, einschließlich solcher aus Silizium und Graphen, wurden verwendet, um die C-reaktiven Proteinmoleküle sowie Troponin-I-Moleküle mit Konzentrationen bis zu 0.1 µg/L zu untersuchen. Die Wiederverwendbarkeit von siliziumbasierten FET-Biosensoren erwies sich als großer Vorteil für die Biosensorik. Inzwischen wurden graphenbasierte FETs erfolgreich eingesetzt, um die dynamischen Prozesse während des induzierten kardialen Ischämie-Stillstands in der HL-1-Zellkultur, die im Reservoir direkt auf dem Chip wächst, zu untersuchen. Die Ergebnisse eröffnen Perspektiven für den Nachweis von Ischämie im Frühstadium und die überwachung der Entwicklung von Herzerkrankungen *in vivo*. Die Anwendung von Graphenmaterial ist für die Entwicklung solcher Biosensorik-Bauelemente unerlässlich, da sie sich leicht in Form von flexiblen und sogar dehnbaren Bauelementen für die Verwendung als implantierbare Strukturen in lebendem Gewebe herstellen lassen.

Contents

Chapter 1

Introduction and Motivation

The research towards integrated sensing instruments based on biological assays for biomolecules has a great impact on such properties as speed, efficiency, selectivity, sensitivity with which analytical and diagnostic biosensors [1]. Biological assays can provide an important information about the absolute or relative concentration of a specific target biomolecule in a biologically relevant substance. Specific target biomolecule of interest is called *analyte* or *antigen* when an active analyte or a virus is considered. With the research progress in sensing instruments, there comes the possibility to perform measurement down to significantly small volumes and concentrations. Biological assays are often characterized via the direct correlation between the quantity of a target analyte or antigen in the given sample and a measurable signal. Devices, that use such kind of interaction between biomolecules on a surface and allow to record the received signal are called *biosensors*. Nowadays, a lot of research, closely related to living organisms and their processes, has been performed in the field of biosensors, bioelectronics, and biotechnology. The processes that occur in living organisms are complex structural biochemical reactions that are caused by various factors that affect them. The cells of living organism are responsible for various functions of biochemical processes and metabolic transport reactions through their membranes. The human body is a unique complex where many different processes in living cells occur. Internal organs, including such vital organs as *brain* and *heart*. In these complex systems, many cells are involved in biochemical processes, which are attractive from point of view of understanding and investigating internal processes. Each type of cells has its own specific functions and properties. What is distinctive for cells of the brain and heart, these cells are subject to electrical processes due to the exchange of ions flowing through the channels in

the cell membrane. Such flow generates electrical potential, that can be recorded by the tools of modern nanotechnology.

Since metabolic transport processes occur inside and outside the cells, it is possible to define two types of electrical potential – *intra*cellular and *extra*cellular. Depending on the changes occurring in the cell membrane, there are also changes in the cellular potential present. Such kind of changes can be the result of violations from such processes as ionic transport, reproductive function, or as a protective reaction to an infiltrated bacterium, a virus, or substance [2]. Fundamentally, the cells are based on proteins. Proteins are biomolecules that can play many different roles and perform a lot of different functions and processes. Biomolecules are responsible for biochemical processes inside cells. To perform their functions, the biomolecules take certain three-dimensional shape to be biologically active [3]. In the case of improper folding and overlaying of protein biomolecules, this can lead to various diseases, such as Parkinson [4], Alzheimer, Acute Myocardial Infarction (AMI) [5], and other disorders. In particular, in recent years, the numbers of cardiovascular diseases have dramatically increased. Currently, all studies are aimed towards creation of specifically sensitive devices, (often called *biosensors*), and understanding of protein folding during different biochemical processes. In addition to the basic functions of protein molecules as an exchange, transport, and regulation, it is worth paying attention to such function as protection.

When a foreign substance, so-called *antigen*, penetrates to the cell, the organism's immune system receives a signal about disturbances and malfunctions in biochemical processes, and therefore, special protective proteins are formed. Produced by immune system, those protective proteins such as immunoglobulin (IgG), are often called *antibodies* [6]. The antibodies have a three-dimensional structure with binding sites, that allows them to identify and bind to very specific foreign biomolecules – *antigens* [7]. Such kind of binding systems with specific recognition regions allow using their properties in the development of biosensors based on antigens for quick detection and consequently improved treatment of diseases and inflammations. Proposed biosensors are used as sensitive dielectric devices for various measurements and studies of complex biomolecules.

Despite the progress in modern medicine, a lot of diseases yet continue to threaten human health. According to the World Health Organization statistics, heart diseases are the major cause of death and disability worldwide. Among them, the

most serious illness with the potentially lethal outcome is acute myocardial infarction (AMI) [8]. The operational definition of AMI is currently based in their symptoms, as well as ECG changes indicative of new ischemia, and the detection of a rise or fall in biochemical markers of myocardial necrosis [9]. However, biomarkers are fundamental for the diagnosis of AMI because symptoms may be atypical or nonexistent, making electrocardiogram (ECG) changes to be absent or nonspecific. At the same time, monitoring of the elevated concentration of biomarkers related to heart disease, particularly cardiac troponin, provides reliable, convenient and non-invasive tools to gain insight into AMI prognosis. And this approach really improves substantially clinical decision-making and outcomes in patients with acute coronary syndrome [10].

This introduction continues with Chapter 2 that will describe the heart tissue, its structure, and importance for the operational properties of proteins, such as aptamers and antibodies. Chapter 3 will introduce to the readers the surface modification techniques that are required to immobilize the biomarkers and successfully fabricate a biosensor. The main goal of the work is to develop novel kinds of biosensors and evaluate their sensitivity, reliability, accuracy, and (ideally) re-usability for detection of specific biomolecules that are involved in important biochemical processes inside the human organisms. The first kind of such biosensors are WGM resonator-based ones, and they are introduced and discussed in Chapter 4. The second kind of biosensors, capacitive electrolyte-insulator semiconductor (EIS) sensors is introduced in Chapter 5 of the work. These biosensors are very interesting due to their simplicity in fabrication and overall high sensitivity acquired during the work. Different kinds of EIS-based biosensors, including antibody-based ones and aptamer-based ones, successfully fabricated, tested, and the results are explained in the chapter. The next kind of biosensors that were developed and used in the work are Si-FETs and Graphene- field-effect-transistor (GFETs) based biosensors. They are presented in Chapter 6. Si-FETs have been used for antibody-based biosensing of CRP and cardiac troponin, while GFETs have been successfully used for direct interfacing with heart tissue cell in order to record changes in membrane potential as a result of cardiac ischemia.

Chapter 2

Heart and Cardiac Cells

In order to clearly understand the main object under study of this work, one should pay attention to an extremely important organ - the heart. Heart plays one of the most important roles in any living organism and is responsible for the blood flow through the body (see Figure 2.1). A human heart consists of four cardiac muscular chambers: left and right atrium as well as left and right ventricles. The right part of the heart is responsible for the pumping of the oxygenated blood from organs to the lungs. After reaching the lungs, the blood is getting enriched with the new oxygen and flows back to organs through the left ventricle.

If we look at the heart as at the functional complex system, we can say that the heart is a multi-component polymeric heterogeneous with an originally natural active medium. Motion of cardiac muscles in this a complex system is caused by the movement of blood and the renewal of oxygen. An important role is also represented by the cells that for the cardiac muscles, which are called cardiomyocytes. The ability of cardiac tissue cells to provide an excitation process is the basis of the heart functions. Cardiomyocytes are generating an electrical potential as a response to a particular irritant (electrical, chemical, mechanical or any other). Moreover, the cells can be excited spontaneously, regardless of the natural process of the excitation. The main mechanism of spontaneous excitation and generation of potentials by cells is related to the exchange processes and changes in the permeability of cell membranes. According to the special structure of each cell membrane, the exchange of different ions (calcium, potassium, sodium) through the ion channels occurs. The contraction of the heart cardiac tissue or muscle is the spreading process of continuous electrical potentials that occur in certain cardiac cells. The heart muscle consists of two main groups of cardiac cells:

- the cells of the working myocardium, the main role of which lies in the rhythmic contractions ensuring the pumping function of the heart;
- the cells of the conducting system.

The conduction system layer, in turn, consists of

1. a sinus node located in the right atrium;
2. atrioventricular node located on the border of the atria and ventricles
3. directly conducting system, including the Guissa bundle, located on the border of the ventricles and passing into the left and right legs and Purkinje fibers, penetrating the cells of the working ventricular myocardium.

The special electrical contact between the cells is the main feature of the heart tissue. These types of contacts are formed by parts of cell membranes by neighboring cells. Due to their special properties, such as low resistance at the inside and high resistance at the outside of the cell membrane, an electrical current flows through the cell membrane and spreads from cell to cell. As a result, after a spread electrical signal, complex heart tissue is contacting and behaves almost like one big complete cell. The conductive electrical cellular system generates electrical current pulses with a specific shape and size. Such signals are called electrical action potentials (AP) of the cell.

Potentials arising in the sinus node cause a process of excitation in cardiomyocytes. The process of excitation is the basis of myocardial function since the process of contraction is one of the components of a complex process of excitation. The excitability of the heart muscle changes during the process of excitation - it goes through phase changes. A unique feature of the heart muscle at the phase changes in excitability in the myocardium occur for hundreds of milliseconds and coincide with the main components of the excitation process - bioelectric phenomena and the contraction process. The advantage of the cardiac cells is their ability to contract without any external stimulation, thus the heart can contract without the nerve impulse.

For the analysis of the heart function, measurements of the electrical activity are usually performed. The non-invasive and reliable method is an electrography that is “a measurement of electrical activity in the heart using electrodes placed on the skin of the limbs and chest”. Such fine heart organization and its structure

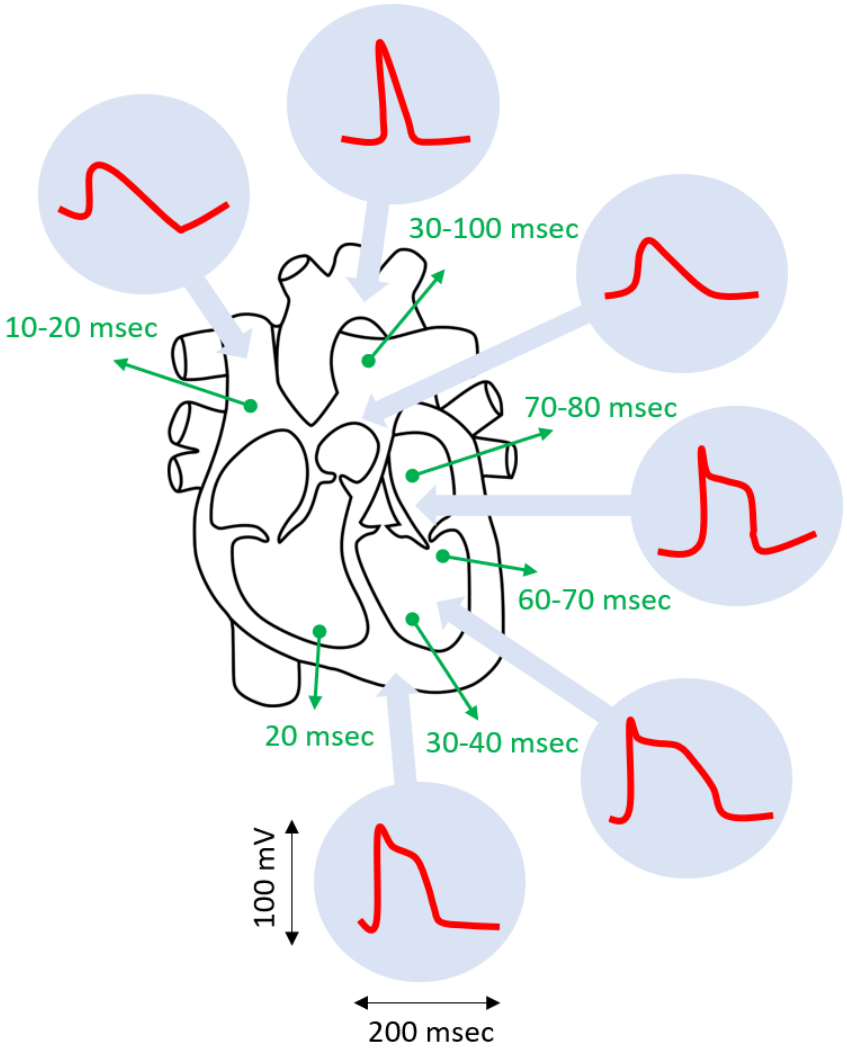

Figure 2.1: Schematic representation of human heart.

were repeatedly confirmed by different methods, including usage of electrophysiology methods and computational biology methods. Electrocardiogram (ECG) is then a graphic representation of the electrical activity of the heart. The pattern of the electrical activity of the heart was discovered a long time ago and usually is recorded as changes in the voltage as a function of time. Figure 2.2 represents the basic pattern of the electrical activity of the heart. It has three important waves that are P, QRS, which is a complex wave, and T wave (see Figure 2.2). Analyzing the amplitude, shape, and timing of the events in cardiogram can give an answer on the functionality of the heart and possible present abnormalities.

The small P wave represents the depolarization of the right and left atriums. This depolarization causes the contraction of the atria. The QRS complex corresponds

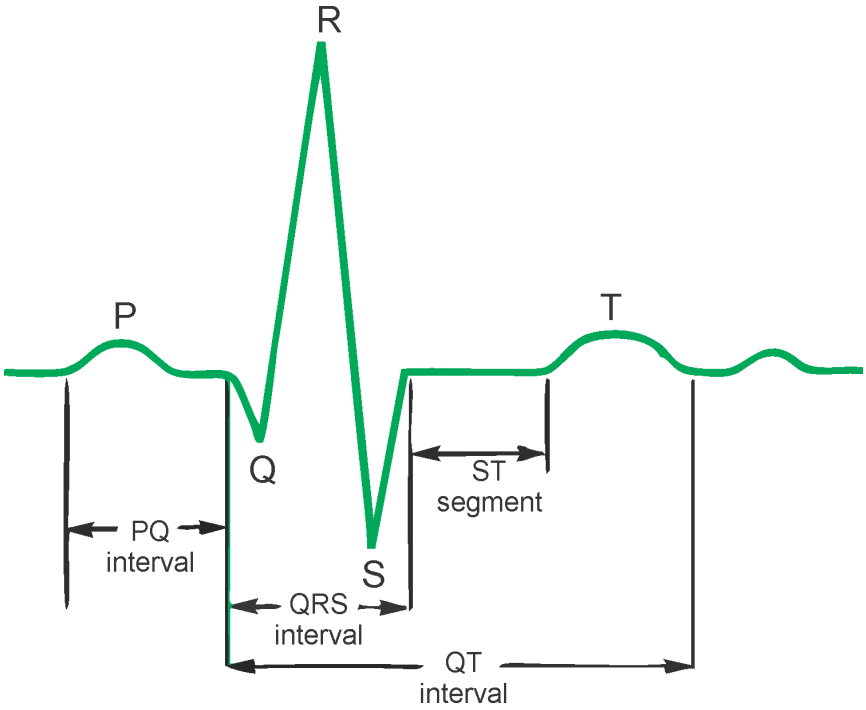

Figure 2.2: The typical electro-physiological pattern of cardiac heart tissue.

to the depolarization of the ventricles that is the larger cardiac muscle. Both ventricles contract at the same time and thus pump the same amount of the blood into both circuits. The T wave represents the repolarization of the ventricles. The repolarization of the atria occurs during the QRS complex phase which masks this event. Marked on the figure 2.2 ST segment corresponds to the region between two waves, S and T, and intervals PR, QRS and QT, represent one segment plus one or more waves.

Every single pattern of the electrical activity of the heart represents a real-time characterization of the heart. Thus, all strange behavior and changes in depolarization or contractions are indicated the changes in the heart. Since the heart is a complex system, it is not so easy to determine the nature of each violation that has arisen, as well as the cause of the violation. In such cases, it can be said that disturbances of metabolic processes inside the cells and their membranes have occurred. If problems are not detected in time and problems are not identified, then such a situation can lead to such bad processes as stopping metabolic cellular processes, disrupting the transmission of electrical signals from the cell to the cell, random confusion of the cardiac tissue, stopping the ionic processes, improper blood circulation, and as a result lead to a severe state of cardiac dysfunction, and in some

cases to death. However, the reasons can be not only external but also internal stimuli.

As a response, or rather a defensive reaction, the cells release various substances through the cell membrane, which help to eliminate the imbalance. Some of these substances become informative in respect of detecting dysfunctions of the heart muscle and diagnostics for a patient. Thanks to such substances and molecules, research in the field of cardiac-biophysics and biology offers new methods for the qualitative detection of abnormalities in the heart muscle. "Cardiac biomarkers"- this name was given to auxiliary molecules.

In this thesis, I utilized and studied two biomoleciles, that are of great interest for understanding the cardiac processes and their role in cardiac functionality:

- *ascorbate*, well known as vitamin C, which is quite common in food, as well also helps to overcome disease;

- *glutathione*.

Antioxidants are widely distributed in plant foods, particularly in fruits and vegetables. Certain antioxidants can cause deficiency diseases and increase the risk of developing cardiovascular diseases (CVD). Therefore, high intakes of antioxidants may reduce CVD risk in humans by preventing oxidative damage and may inhibit the main underlying process that leads to CVD and atherosclerosis. Reactive oxygen species (ROS) play an important role in the regulatory functions of all biological systems. These molecules are chemically reactive and contain oxygen which is the product of the normal oxygen metabolism responsible for a number of reduction-oxidation reactions, cell signaling and homeostasis. However, under the oxidative stress conditions, an imbalance in the ROS level preset. This results in the excitation of the system to detoxify the ROS intermediates and to repair the damaged locations in the cells. It is well known that such imbalance in oxidation-reduction reactions plays a major role in aging processes and many diseases, such as cancer, diabetes, hepatitis, cardiovascular and neurodegenerative diseases, including Alzheimer and Parkinson. As a result of an imbalance state of the cell, ROS may damage the sub-cellular compartments. This can lead to the process of programmed cell death by activating free-acting proteins by a chain reaction. The effect of ROS on cell metabolism includes not only programmed cell death, but also positive induction of host defense genes and mobilization of ion transport systems, including

the implication of mediators in cardiovascular diseases (ischemic injury, stroke and heart attack). Thus, ROS are playing a dual role as deleterious and simultaneously beneficial species. Any dysfunction of the cell may be recorded as an increase in ROS level causing oxidative stress. Understanding ROS sources and ROS-balance reactions are crucial for the analysis of cell signaling pathways at intracellular and extracellular exchange process levels. It is very important to create new methods for detection and characterization of molecules, responsible for reduction-oxidation reactions in ROS-balance reactions. The main aim of our studies is the measurement and analysis of characteristic parameters of antioxidant specific biomarkers in solutions with different concentrations.

Heart cardiac biomarkers *C-reactive protein* (CRP) and Troponin have also attracted much interest. Cardiac biomarkers are found directly at certain stages of heart disease. Quantitative analysis of the concentration of substances will allow to determine the degree and stage of inflammation.

C-reactive protein (CRP) is a plasma protein involved in a process of the acute phase response. It was discovered in 1930, from the cell wall by the poly-saccharides precipitation. CRP is interesting because it plays not the last role as a biomarker in a number of diseases. Analysis of research results has shown that the CRP is not just an inflammation marker, but also a functional complex that may directly modify the inflammatory process itself [11]. Since then, the protein has been involved in interactions with various other ligands, activations the complement pathways, stimulations of phagocytosis and binding to Fc region of immunoglobulin receptors. CRP comes from the family of oligomeric calcium-binding proteins exhibiting high sequence homologies, also known as pentraxins [12]. Originally, it was observed that CRP was produced by liver hepatocytes. However, followed reports showed the variety of extra-hepatic sources of human CRP. The sources includes the neurons from patients with Alzheimer disease [13], normal arterial smooth muscles [14], adipose tissue from patients with coronary artery disease. CRP has a pentameric cyclically symmetrical structure, shown schematically in Fig. 2.3, and consists of five identical subunits of 206 amino acids, which is non-covalently arranged around the central pore.

The structure can be divided into two parts: face and back-face. The face contains concave recognition phosphocholine-binding site and two binding sites of calcium ions. The back-face is the effector‘s face, it is believed that a deep cleft is mediated

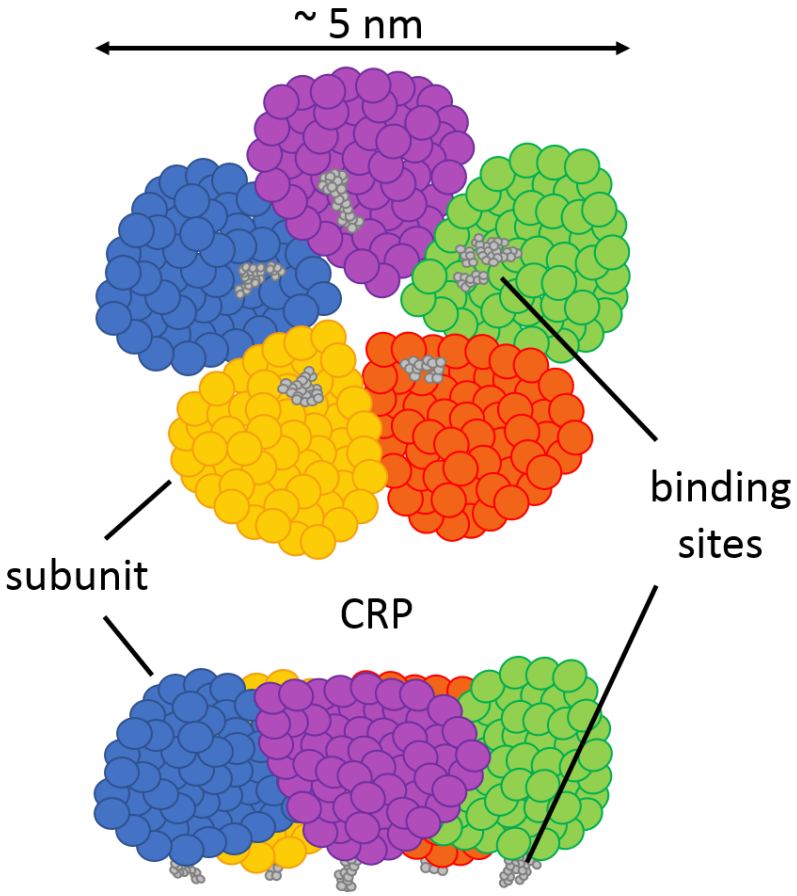

Figure 2.3: Schematic of cyclically symmetrical pentameric structure of C-reactive protein.

to bind with complement parts of recognition receptors. Native C-reactive protein exists in a pentameric form of five identical subunits [15]. However, in the absence of calcium or due to changes caused by a denaturing environment, native CRP may undergo structural changes, by dissociating from its pentameric arrangement [16]. Separated modified forms of CRP subunits often called monomeric (mCRP). They can express different epitopes compared to the native CRP [17], and they have distinct properties [16] as well as the native protein. Commercial CRP is derived from recombinant human CRP produced in Escherichia-coli microbe and has concentrated sodium azide added as a preservative. Research suggests that CRP has both pro- and anti-inflammatory effects. A wide variety of different properties, such as complement activation, inflammatory cell recruitment, cell activation, cytokine release and more has been confirmed by research to this protein.

Troponin is a protein complex that consists of three subunits (I, C and T) that

modulate the calcium-mediated interaction between actin and myosin in skeletal and cardiac muscle tissue (see Figure 2.4). Subunit I is ideal biomarker for necrosis diagnosis due to highly cardiac specificity, fast realization time and high elevation level [18]. Heart damage progresses very fast and delayed medical treatment increases the probability of mortality. Therefore, rapid and accurate diagnosis of cardiac cells necrosis and early treatment are critical to increase the survival rate.

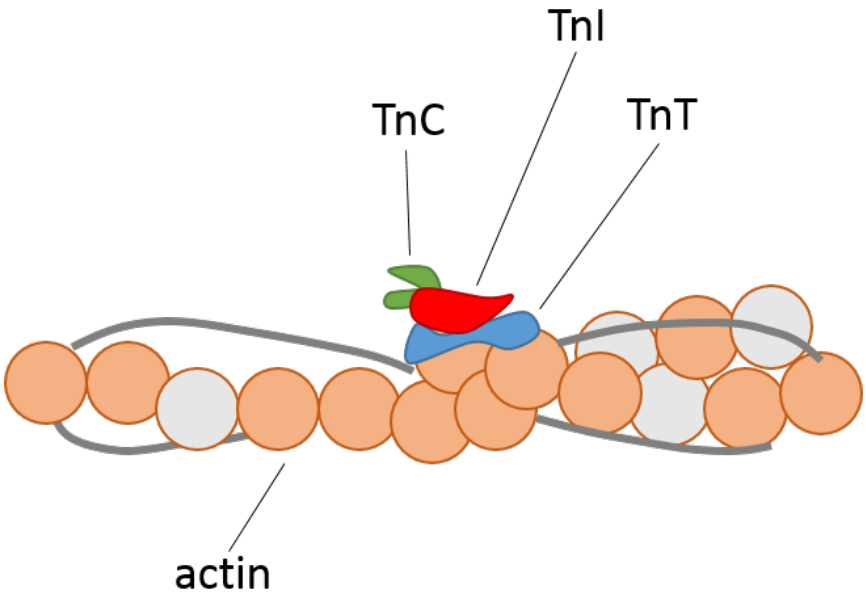

Figure 2.4: Troponin complex: sub-proteins troponin C, troponin I and troponin T. Adapted from [19], [20], [21].

The Troponin complex is a complex of proteins which is controlling the calcium-mediated molecular interactions between actin and myosin in a striated heart muscle. This complex consists of three important sub-proteins: troponin-C, troponin-I and troponin-T. All proteins from complex occur in cardiac and skeletal muscles, but not in smooth muscles [22]. Troponin-C is a cardiac slow troponin expressed in a skeletal muscle. Troponin-T is identical to cardiac troponin-C, but unlike it, this protein is specific to the heart and plays an important role. Comparing to other cardiac troponins, the Troponin-I (cTnI) is a small myofibrillar protein associated with the sarcomeres of thin filaments. Noteworthy is the fact that the troponin-I is the only troponin from the complex which is uniquely expressed in the myocardial cells. It plays a role in the activity of actin-myosin interactions by preventing myofibrillar contractions during some specific phases of the cycle of cardiac muscle relaxations and contractions as shown in Fig. 2.5. Both troponin-T and troponin-I have an

informative role as indicators of myocardial infarctions.

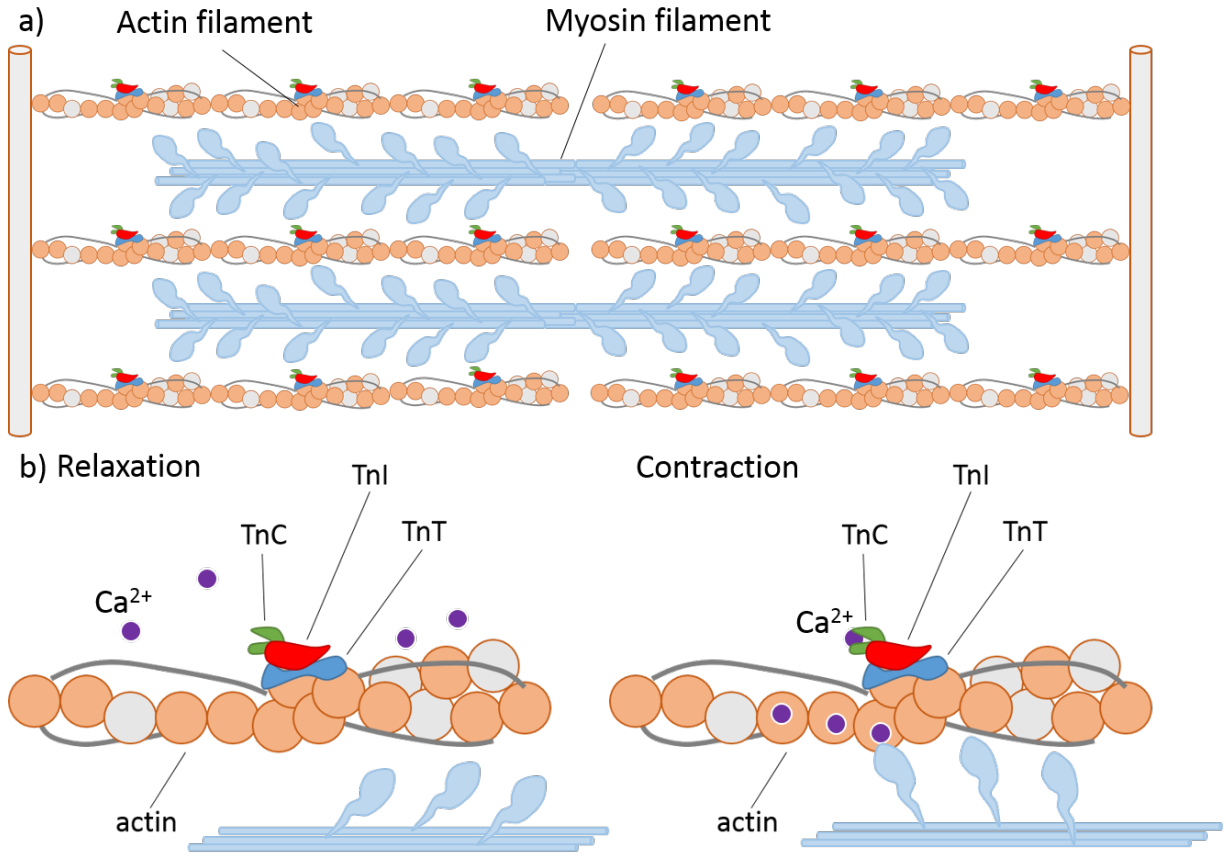

Figure 2.5: a) Troponin complex with three sub-proteins: b) relaxation and contraction of skeletal muscle troponin C; troponin T and troponin I; Adapted from [19], [20], [21].

In addition, they also are known to be essentials in the diagnosis of heart failures. Recent studies have been reported that there are correlations between the troponin concentrations in blood and acute ischemic stroke. For the early diagnosis of patients with acute ischemic stroke, it was recommended the assessment of cardiac biomarkers. The use of cardiac troponin-I as a biomarker for the detection of myocardial injury has resulted in a substantial increase of efforts in the development and research of fast and sensitive sensors for diagnosing acute myocardial infarction in a human. Various studies demonstrated that cardiac troponin-I should be detected at very low concentrations below the detection limit of available commercial assays. This protein exists both in the cytoplasm and in sarcomeres of the cardiomyocytes. However, in cytoplasm cTnI exist in unbound free form and only between 3 % and 7 % from concentration state. The major amount of cardiac troponin-I present in the cardiomyocytes. This cytosolic component mostly released into the extracel-

lular space during the process of ischemia or after an insult resulting in necrosis. During the myocardial injury, there are two possible ways of troponin release: one is a transient release and one a persistent release of cTnI. The transient release of troponins is occurring from the cytosolic pool due to leakage, which results in increased circulation of the cTnI. Followed increasing permeability of a membrane by reversible oxygen circulation generates inflammation and even toxic damage, leading to degradation and leakage of cardiac proteins. The transient release is associated with reversible ischemia [23], [24], [25]. Due to ischemic necrosis with subsequent reperfusion present a damaged cardiac tissue and an irreversible loss of the cardiac myocytes. Wounded tissues can prolong the persistent release of cardiac troponin I. Furthermore, recent studies with commercially available assays have shown that cTnI concentrations do not rise immediately after an acute myocardial insult. The release of cTnI may take up from 4 to 6 hours to become diagnostically measurable. While the damaged myocardium is on the way of undergoing reperfusion and repair, cTnI is prolonged to continuously release into the bloodstream. The cardiac troponin concentration in blood can remain elevated up to 14 days before decreasing to previous non-injury levels. Therefore, this cardiac biomarker can be used as an indicator of myocardial injury due to its stability and a longer period of a lifetime than other proposed cardiac biomarkers.

In this thesis, we show you new techniques that will constitute a great competition in the field of cardio biophysics research.

2.1 Antibodies

As it was mentioned earlier, within the heart inflammation many different types of molecules and substances are released into the extracellular space and even into the bloodstream.

It is clearly understandable that the main goal in this research is to detect the molecules of interest. Some types of molecules do not require addition receptors or binding sites, mainly because such molecules are usually large in size. However, when for measurement you have a mixture of several different molecules, it becomes difficult to select the target one. To be able to take out the proper molecule you will need some extra catcher. Therefore the recognition receptors have to be applied.

Proteins are also formed into antibodies, so-called immunoglobulin (IgG, see the

Figure 2.6), as protective proteins produced by the immune system as a response to an exterior biomolecule or substance, called an antigen.

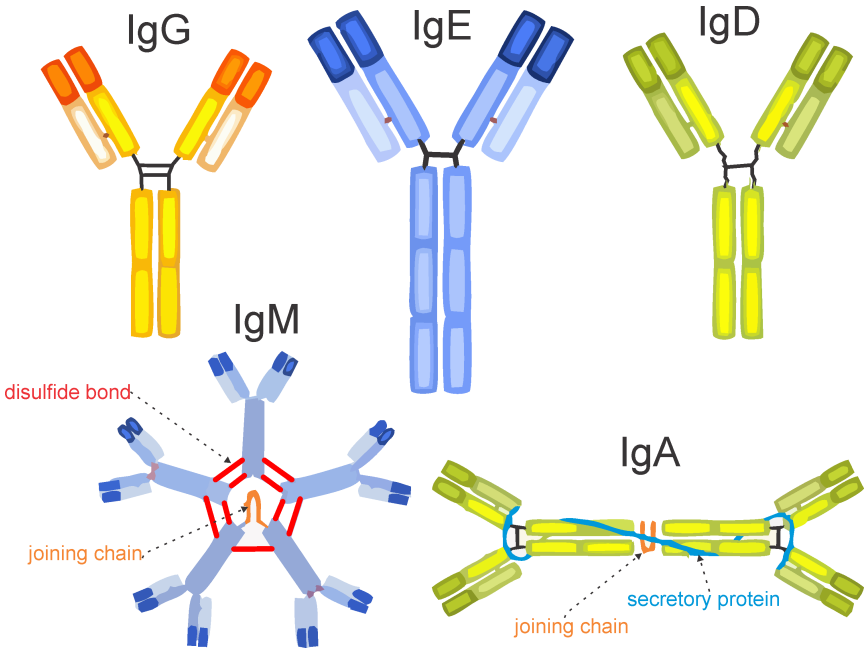

Figure 2.6: Schematic representation for different types of antibody binding receptor.

There are several types of antibodies structures that are currently being focused on in biosensing (See Fig. 2.6). Immunoglobulin consists of two light and two heavy chains, linked by disulfide bonds to form the characteristic Y-shape. The light chain is divided into constant (C) and variable (V) regions. On the second heavy chain constant region (CH_2), IgGs have carbohydrate moieties (See Fig. 2.6) [26]. The variable domain bears three hypervariable regions, known as complementarity-determining regions (CDRs), which are responsible for the specific antibody-antigen interaction. The diversity in this area allows the endless supply of antibodies with different specificity and binding strength (affinity).

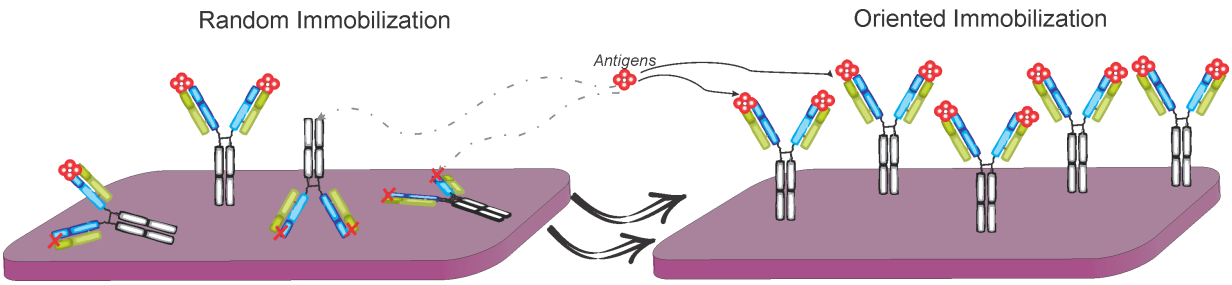

Figure 2.7: Random (left) vs. oriented (right) immobilization of immunoglobulins IgGs.

Providing information about antibody orientation on the surface is of fundamen-

tal interest. Immobilized IgG can adopt four exemplary molecular orientations: side-on (one F_c and one F_{ab} attached to the surface), tail-on (F_c attached to the surface), head-on (both F_{abs} attached to the surface) or flat-on (all three fragments attached to the surface) as shown in Figure 2.7. For the highest analyte binding, Abs should display free antigen-binding regions after immobilization. Controlling the orientation will, therefore, lead to better analyte binding. This will result in improved biosensor sensitivity.

2.2 DNA modified Aptamers

Biomolecules are unique materials, which consist of specific structures and compounds mostly produced by cells and living organisms. The variety of available molecules under study is divided into major types of groups such as carbohydrates, lipids, nucleic acid, and proteins. Biomolecules have different sizes, structures, functions and play an important role in the functionality of the human organism. Moreover, biomolecules that take part in the organism processes often become indicators of a disorder or inflammations. This allows to create of helpful drug and vaccines, usable and painless treatments, as well as inflammation indicators in a sensitive and selective biosensor. The important and unique biomolecules among all biomolecules are Deoxyribonucleic acid (DNA) and Ribonucleic acid (RNA). They are carry the regularized sequence of nucleotides which define the amino acids sequences of proteins called genetic code. The specific order in which these amino acids have occurred, determine fundamental protein structure and function. There are 20 different amino acids that can be combined in sequences within the proteins. Proteins are major structural elements presented in all living organism and produced by the cells. They are involved in various processes and chemical reactions inside and outside the living cells, as it is shown in the Figure 2.8. Research interest in this study mostly concentrated on biomolecules such as DNA, and on a group of proteins closely related to cardiac activity.

Aptamers are short single-stranded oligonucleotides that are capable of binding various molecules with high affinity and specificity. When the technology of aptamer selection was developed almost a quarter of a century ago, a suggestion was immediately put forward that it might be a revolutionary start into solving many problems associated with diagnostics and the therapy of diseases. Aptamers are

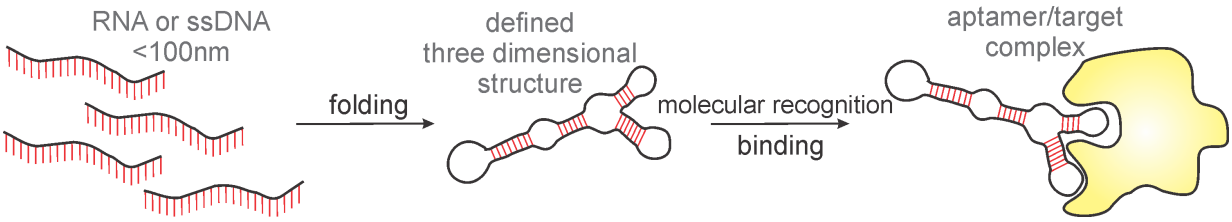

Figure 2.8: Schematics of the molecular recognition between target molecules and synthetically fabricated aptamers.

small (usually from 20 to 60 nucleotides) single-stranded RNA or DNA oligonucleotides able to bind target molecules with high affinity and specificity. Currently, a large number of generated aptamers can bind various targets, ranging from simple inorganic molecules to large protein complexes, and entire cells. In fact, aptamers are nucleotide analogs of antibodies, but aptamer-generation is significantly easier and cheaper than the production of antibodies. Moreover, aptamers are neither immunogenic nor toxic. All these features make aptamers ideal candidates for diagnostic and therapeutic applications, purification of target molecules from complex mixtures, biosensor design, etc. Aptamers represent the newly developed field of research, which is promising for a wide range of biosensor applications. Aptamers may be used as recognizing elements in biosensors. They are 10-100 times smaller than antibodies and can be arranged with a higher density on the biosensor surface. Aptamer-based biosensors require a smaller volume of the tested sample and can be reused without loss of sensitivity. This type of recognition receptors is promising therapeutic agents because they are cheap, non-immunogenic, and easy to be modified. Inhibition of target enzymes is the main field of aptamer application as drugs. Aptamers may inhibit target enzymes by binding to the catalytic center or inducing conformation changes in a protein structure.

Chapter 3

Surface Modification Technologies

IIn this chapter, I describe the step by step surface modification technologies and the series of surface reactions optimized during this research for various types of biosensors. The optimization was done for each functionalization step leading to the covalent binding of target biomolecules and corresponding recognition receptors. Based on a surface modification antibody/antigen binding and DNA synthesized aptamer, the specificity was monitored by thin-field dielectric layers devices as a function of potential and impedance changes at the surface.

Basic conditions for creating compatible functional layers for the attachment of target biomolecules (e.g. proteins, enzymes, DNA, membranes, cells) on solid biosensor surfaces are developed on the basis of a cleaning and surface activation of the test structures. A lot of different procedures of wet and dry cleaning in immobilization protocols for the further attachments of biomolecules were described and proposed in a related publication. Properly cleaned and activated sensor surface is the most critical and important part in the attachment of biomolecule. In this section, the step by step surface modification technologies as a series of surface reactions optimized for various type of biosensors are described. Surface modification technique provides selectivity and sensitivity to the desired biomolecule of interest. During this work, several immobilization protocols were developed. Those protocols were tested on a silicon dioxide thin-film dielectric layers as a control substrate. As well as with control substrates, the immobilization protocols were developed to be compatible with the fully encapsulated FETs-based devices for the further electrical sensing studies, which are presented in the sections 5, 6.1 and 6.2 of the work.

Standard and common cleaning methods for silicon surfaces include wet chemical cleaning [27], UV-treatment [28], temperature annealing or plasma cleaning pro-

cedures [27]. From the following procedures the wet cleaning method was chosen. Chemicals effectively clean the surface from contaminations and provide a highly hydrophilic surface. It is should be taken into account, that in any case of fabrication or functionalization, a proper cleaning step is necessary. After the cleaning procedure, the particles and dust should be completely removed. This may result in a change of surface roughness. Fig. 3.1 shows AFM images taken after wet chemical cleaning with different acids or bases. For all presented images an area of 5×5 μm^2 was scanned.

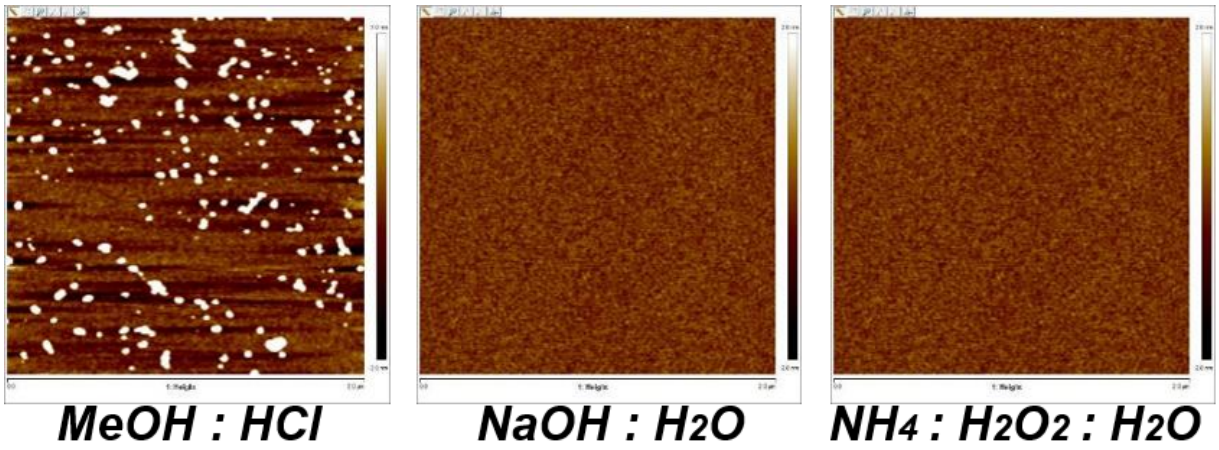

Figure 3.1: Scanned 5x5 μm^2 AFM images of the surfaces treated with the different activation solutions.

In principle, the chemical activation solutions should provide a value of water contact angle on the surface indicating a current state of the surface. The lowest value corresponds to a hydrophilic surface with a high number of open hydroxyl groups(-OH). The water contact angle is simple and informative tool for reflecting information about the reactivity of the surface. It allows to provide a comparative analysis of surface quality. From the same set of samples, the topology changes were monitored, as well as a water contact angle and layer thickness.

In Table 3.1, the different cleaning methods with acids and bases are compared with the corresponding results of measured contact angles. It was an important step to determine the surface roughness, because it was planned to use silicon oxide thin-films for further biology studying. In order to successfully attach biomolecules on fabricated sensors, it is important to know how the surface of sensors looks like. Atomic force microscopy (AFM) was used to monitor surfaces morphology and topology. It is a very high-resolution type of scanning probe microscopy, with resolution of the order of nanometer scale. The major properties of AFM are force

Table 3.1: Comparison of water contact angle and thickness losses for different chemical activation techniques

Chemical solution for activation	Water contact angle	Thickness losses
$MeOH : HCl$	24.6	0.4 nm
$MeOH : HCl : H_2SO_4$	16.9	0.8 nm
$Piranha$	24.2	0.6 nm
$Conc.H_2SO_4$	16.9	0.8 nm
$NaOH : H_2O$	17.6	0.5 nm
$NH_4 : H_2O_2 : H_2O$	28.3	0.6 nm
$NHO_3 : H_2O$	23.5	0.7 nm

measurements, manipulation and surface imaging. These studies were focused on surface imaging. For imaging, the reaction of the probe to the forces that the sample imposes on it can be used to form an image of the three-dimensional shape (topography) of a sample surface at a high resolution. This is achieved by raster scanning the position of the sample with respect to the tip and recording the height of the probe that corresponds to constant probe-sample interaction. The surface topography is commonly displayed as a pseudo-color plot.

The thickness was measured by ellipsometry. The contact angles were taken within 20-30 s after the formation of the sessile drop. After each cleaning procedure, values listed above were collected and compared. From the Table 3.1, based on obtained results, several wet cleaning procedures were selected and used during this work.

From section 2.1 it is clear that it is possible to attach the target molecule through binding with recognition receptors (antibodies or aptamers). The scheme of receptor interaction with the molecule is similar to a simplified version of the key-lock system. The basic principle is the following: for each molecule, the corresponding receptor is produced, and this receptor will not bind any other type of molecule. Even when a receptor is attached to a molecule, it is still not so easy to get a signal response from the bound complex. In this work, we specially designed the sensors with an active sensitive surface. The sensor requires a closely brought charge near it active area, in order to get a signal response. The receptor with an attached molecule will not come spontaneously close enough to the active area of the surface. Moreover, the receptor-molecule complex will be in continuous movement near the sensor surface. This circumstance implies that it is necessary not only to bind the receptor to the target molecule but also to attach them to the sensitive surface of the sensor. The

surface of the fabricated sensors is dielectrics. It will not be enough to simply add a solution with the molecules. It is necessary to cover the surface of the sensors with additional layers that can react with the receptors and form strong bonds. For this, it is important to have a look at receptor structure.

Immobilization strategies may result in the random covering of receptors, specifically antibodies (Abs). The covering and antibody orientation is dependent on the self-organizing capacity of the antibodies, which may be steered by specific reactive groups on the surface, on the antibody, or on the both. Usually antibodies have several possible ways for reaction to occur, due to the presence of different reactive groups. It is highly important to attach antibodies on the sensor surface without crucial changes in their binding activity and specificity. Therefore functionalization strategies should be mild and compatible with the sensor surfaces of various materials. Sensor surfaces can be used directly as is or functionalized with single to several layers. Functionalization strategies can be divided by non-covalent or covalent coupling chemistry.

Hydroxyl groups can be induced on the surface by treatment with KOH, NaOH, or piranha solution. Wet chemical cleaning instead of two steps could be done in one step: it can clean the sensor surface from dust and dirt and it simultaneously can open hydroxyl groups. Silanes readily react with different types of surfaces through surface hydroxyl groups to form a strongly bound coating that includes both covalent bonds and multiple van der Waals interactions. Silanes are hydrolyzing in solution to form silanols, which readily attach to the surface by their reactions to the surface to form Si-O-Si (siloxane) linkages. Effectiveness of silane on silica, quartz, glass, and aluminum is excellent. Silanes with different functional groups such as amino, carboxyl, anhydride, and azide are commercially available and useful for the covalent attachment of antibodies on substrates with -OH groups.

The induction of amino groups on the surface has been one of the most widely used surface functionalization chemistry. The most extensively used surface functionalization chemistry for the induction of amino groups on a wide range of substrate is the treatment with 3-aminopropyl-triethoxy-silane (APTES) via wet chemical procedures or chemical vapor deposition in specific argon atmosphere (CVD) [29]. APTES can be deposited on solid materials, electrode materials, nanomaterials, and nanocomposites under variable conditions of concentration, solvent, temperature, and time. In addition, curing conditions such as air/heat drying might be

necessary depending on the intended application [29].

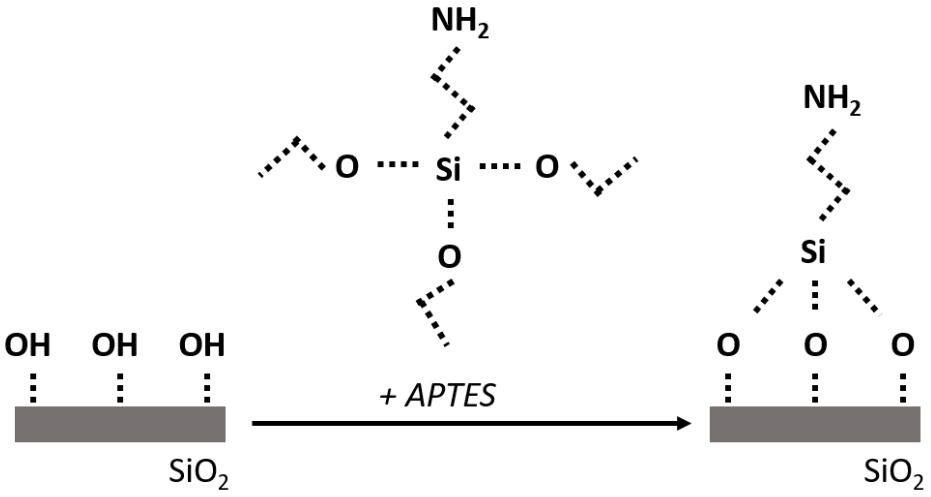

Figure 3.2: APTES reaction with activated hydroxyl -OH groups on oxidized surface.

Normally, silanization is occurring on any type of substrate with chemically active hydroxyl groups for silane grafting [30]. Sometimes substrates already have hydroxyl groups, while others require a pretreatment step with wet chemical cleaning and activation or plasma treatment to introduce hydroxyl groups as mentioned previously. APTES reacts with the free hydroxyls of an oxidized substrate by exchange with the loss of ethanol (Fig. 3.2).

The substrate with hydroxyl groups by reaction with APTES forms a hydrogen bond with the metal surface [31]. A mixture of amine and hydrogen-bonded amines can coexist on the same solid metal surface. Amino molecules orient away from the surface for further biomolecule attachment, whenever the hydrogen-bonded amines are stays bound to the surface. If the surface does not have any oxide groups, the amino molecules react with carbon dioxide from the atmosphere.

The silanization procedure can be done by either wet chemistry or vapor deposition in an argon atmosphere. Wet silanization implies that the process is performed in a liquid solution. Based on the chosen solvent, the wet-silanization process can be classified as organic-/aqueous- or evaporated-based. Ethoxy terminated groups of APTES to initiate the reaction of hydrolysis. On the other hand, vapor deposition is generally a silane deposition on a substrate through evaporation pressure. Vapor deposition advantage is that the with silanization presence of the water-soluble solution is minimized. An activated substrate is simply placed in a closed desiccator, in an environment of an argon atmosphere, and through vapor pressure

silane is depositing on the substrate. Silanes have a low value for vapor pressure for the reaction proceeding, thereby depositing monolayers. Measured by ellipsometry APTES layer thickness on silica is $5A^o$ and $6A^o$, which is in good agreement with the length of an APTES molecule, and illustrating the formation of a monolayer on the substrate [32].

At amine-functionalized substrate by reaction with succinic anhydride can be deposited carboxyl groups as well. A carboxylic reaction can occur with similar glutaric anhydride or citraconic anhydride. And thus, similarly, the thiolated substrates can be induced by carboxyl groups.

Epoxy groups can be induced on the substrate by treatment with (3-glycidoxypropyl)-trimethoxysilane (GOPS/GPTES). They are very stable at neutral pH and, under aqueous reaction conditions. Epoxy groups are reactive toward nucleophiles such as amines, thiols, or acids. The aminated substrate can also be induced with epoxy groups by treatment with oligo(poly)ethylene glycol diglycidyl ether.

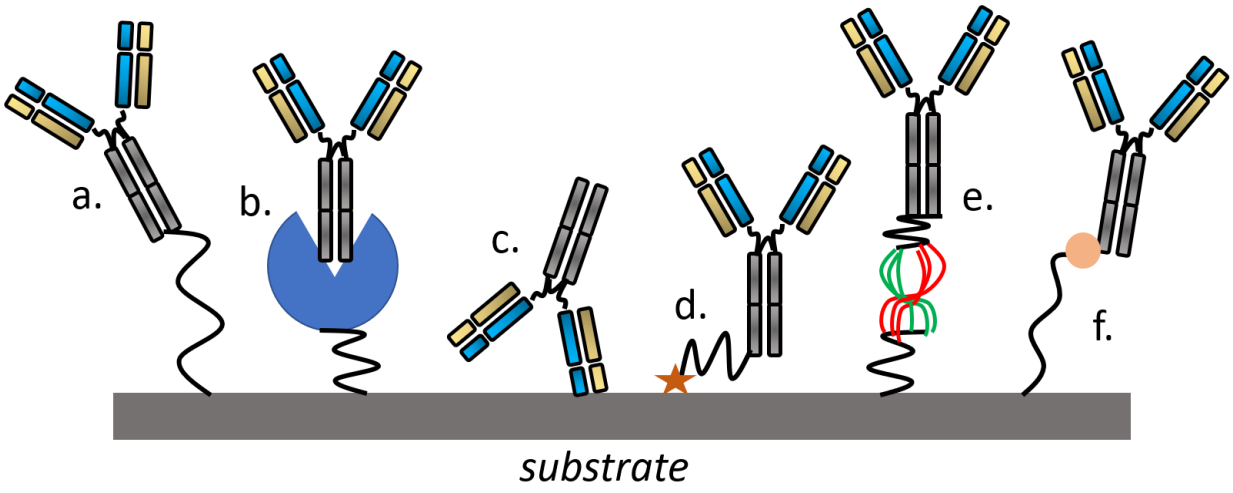

Figure 3.3: Schematic of different methods of antibody immobilization: (a) - covalent, (b) - oriented, (c) - non-covalent/random, (d) - site-specific, (e) - DNA-directed, (f) - recombinant.

A wide range of antibody immobilization chemistry protocols has been developed. All different methods are schematically shown in Fig. 3.3 and the detailed protocols are given in appendix D. In the ideal representation of the experiment, the benefits of oriented immobilization win, since with such a procedure, the antibodies will be rotated with the main recognition part upwards. If antibody stands up with it Y-shape then it will certainly improve catching ability for the target molecules, and

increase the sensitivity of the sensor. The work on the development and fabrication of functional layers was focused on providing oriented immobilization of molecules. Based on immobilization techniques described in the literature, different chemical protocols were created. The functional layers are added step by step allowing the molecule to be attached.

Table 3.2: Selection of techniques and reactions between various groups of antibodies and specific surfaces or layers.

Group	**Reaction with:**	Ref.
Amine group	carboxy-methylated dextran layers	[33] [34]
Amine group	gluteraldehyde exposing surfaces	[35] [33]
Amine group	epoxide-functionalized polymer brushes	[36]
Amine group	NHS-activated biotin	[37]
Intermediate protein	protein A and G (non-covalent)	[38]
Intermediate protein	protein A and G (covalent)	[39]
Thiol group	gold	[40]
Thiol group	meleimide-functionalized biotin	[37]
Thiol group	meleimide-functionalized surfaces	[41]
	Reduced with:	
Difulphide bond	2-mercaptoethanol	[40]
Difulphide bond	UV-light adsorption by nearby aromatic amino acids	[42]

Here in Table 3.2 I present a selection of the techniques recently applied to characterize antibody orientation in a more direct manner by measuring the layer thickness or by scanning of the surface. For this research I has selected the best protocols considered for the development of optimized technology. In order to get the full picture, several techniques ideally should be combined. Many techniques have been used to elucidate the presence and binding function of immobilized antibodies. Fourier transform infrared reflection (FTIR) spectroscopy is used to characterize the presence of specific chemical groups, and various fluorescence microscopies help to visualize the efficient binding of the analyte to antibody-functionalized surfaces [26], [43]. In fact, spectroscopic techniques are predominately used to roughly confirm an effective antibody orientation, with only a relatively small set of studies that investigates the orientation of Abs by comparing antibodies immobilized in different directions. For example, SPR can be used to calculate the antibody coverage, and the relationship between the adsorbed amount and molecular orientation

on the surface. It has been used earlier to distinguish between tail/head-on and side/flat-on orientation [44]. However, the only minimal direct information about antibody orientation can be deduced with such approaches.

All developed protocols have been tested on the thin-film dielectric layers of silicon oxide. At the begging, the developed immobilization protocol started from the cleaning procedure of sensors. Thin-film dielectric layers of silicon oxide were hydroxyl activated in plasma oven (O_2, 0.8 mbar, 80 W, 3 min). After oxygen plasma treatment, contact angle measured were performed. It quantifies the wettability of a solid surface by a liquid via the Young equation:

$$\Upsilon^{sv} = \Upsilon^{st} + \Upsilon^{lv} \cos\theta \tag{3.1}$$

where θ is contact angle; Υ^{sv}, Υ^{sl}, and Υ^{lv} are the free energy of solid surface, solid/liquid interface and liquid surface interface, respectively. A given system of solid, liquid, and vapor at a given temperature and pressure has a unique equilibrium contact angle. If the liquid molecules are strongly attracted to the solid molecules then the liquid drop will completely spread out on the solid surface, corresponding to a contact angle of 0^o. Generally, if the water contact angle is smaller than 90^o, the solid surface is considered hydrophilic [45] and if the water contact angle is larger than 90^o, the solid surface is considered hydrophobic, as shown in Table 3.3.

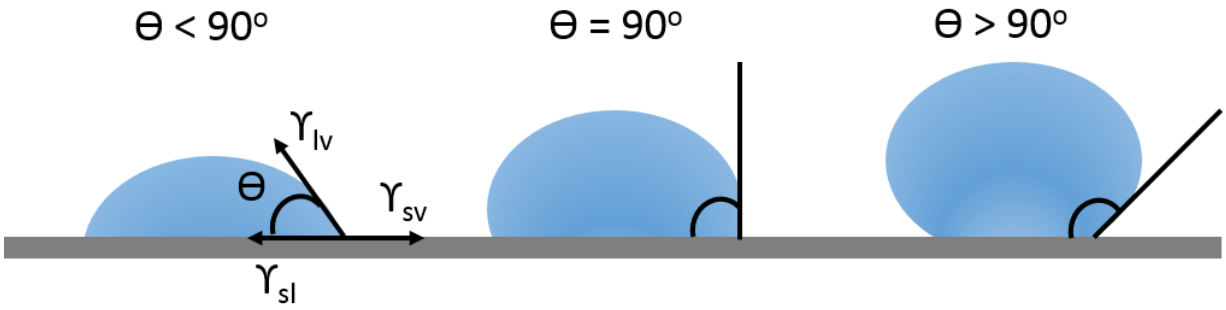

Figure 3.4: Schematic of a liquid drop showing the quantities in the Young equation.

As can be seen from Fig. 3.5, both wet chemical and plasma activation methods are suitable for providing a hydrophilic surface. Results for different approaches in wet chemical activation can be seen in Table 3.1. Table 3.1 shows that some of the chemical solutions are etching a higher amount of thickness than was expected.

Then at argon atmosphere, the thin-film dielectric layers were silanized with APTES molecules in a desiccator at 5 mbar for 1 hour. The APTES silane was

Table 3.3: Water contact angle values corresponding to the strength of solid/liquid interactions.

Contact angle	Degree of wetting	Strength of solid/liquid interactions	Strength of liquid/liquid interactions
$\theta = 0°$	Perfect wetting	strong	weak
$0°<\theta<90°$	High wettability	strong weak	strong weak
$90°\leq \theta <180°$	low wettability	weak	strong
$\theta = 180°$	non-wetting	weak	strong

Figure 3.5: Measured water contact angle before and after wet chemical and plasma induced surface activation.

compared with 3-glycidyloxypropyl-tri-ethoxy (GPTES) silane during silanization process under different atmospheres - wet and dry. On silicon surfaces attachment is typically mediated by first silanizing the surface followed by immobilization of biomolecules of interest. Silanes such as APTES and GPTES are attractive for such applications due to significant advances in the understanding of this class of surface modification agents. Notably, amino silanes have the advantage of catalytic activity by the amine group that facilitates the formation of siloxane bonds with surface silanols, mitigating and potentially obviating the need for post-depositional curing. The amino group has also been reported to crosslink with GPTES through an acid-catalyzed addition of the amino group to the epoxy functionality [46].

After performed silanization process of the activated surfaces, a post-treatment with acid was used. Dilute anhydrous acetic acid was found to be essential at providing the finest thinnest silane layers. The effect of the post-treatment was confirmed by XPS [47]. Silanization procedure was claimed reproducible for development of

thin silane layers of less than 2 nm independent of the process time.

Protein-protein interactions comprise the underlying molecular mechanism of a multitude of complex biological processes. Chemical cross-linking offers a direct method of identifying both transient and stable interactions. This technique involves the formation of covalent bonds between two proteins by using bi-functional reagents containing reactive end groups that react with functional groups such as primary amines and sulfhydryls- of amino acid residues. Cross-linkers (CL) are either homo- or hetero-bi-functional reagents with identical or non-identical reactive groups, respectively, permitting the establishment of inter- as well as intra-molecular cross-linkages. A variety of cross-linkers are commercially available from major suppliers such as Pierce, Molecular Probes, and Sigma-Aldrich. Homo-bi-functional reagents, specifically reacting with primary amine groups have been used extensively as they are soluble in aqueous solvents and can form stable inter- and intra-subunit covalent bonds.

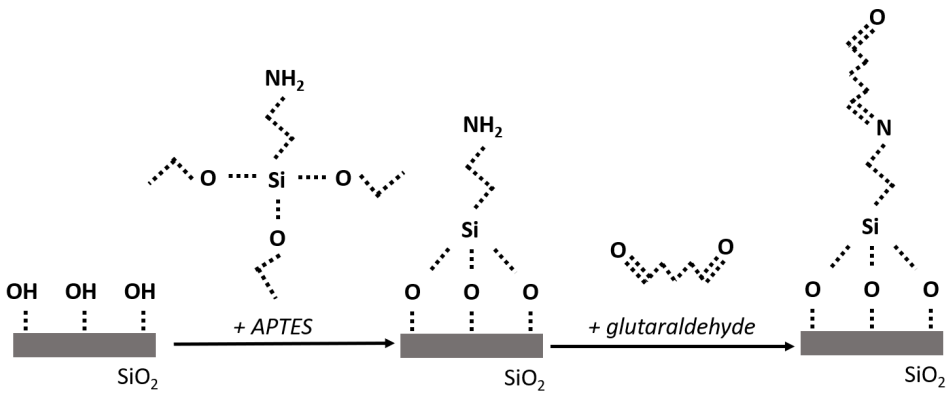

Figure 3.6: Schematic of covalently linked glutaraldehyde with APTES silane on oxidized surface.

Glutaraldehyde is a bi-functional compound mainly used in chemical modifications of proteins and polymers. This bi-functional compound links covalently to the amine groups, as shown in Fig. 3.6, creating a stable structure then that attained by the physical aggregation of protein molecules. These solid aggregates are held together by non-covalent bonding and readily collapse and redissolve when dispersed in an aqueous medium. Treatment with cross-linkers should be performed in buffers free from amines. Phosphate buffers at pH 7.5 to 8.0 are most stable and suitable for molecular interactions. When used in large molar excess, glutaraldehyde can be used to activate one protein for conjugation to the second protein (e.g., the

antibody).

Finally, after activation and silanization with followed linker attachment, the thin-films were covered with recognition receptors dissolved in PBS. However, immobilized molecules on the sensor surface may also interact in a non-specific manner with proteins without receptor bindings. Proteins can be adsorbed on the surface and with the surface itself. To avoid these sorts of unspecific interactions, an "inert" background is needed. It is important not just to block background, but also to affect the activity of biomolecules as little as possible.

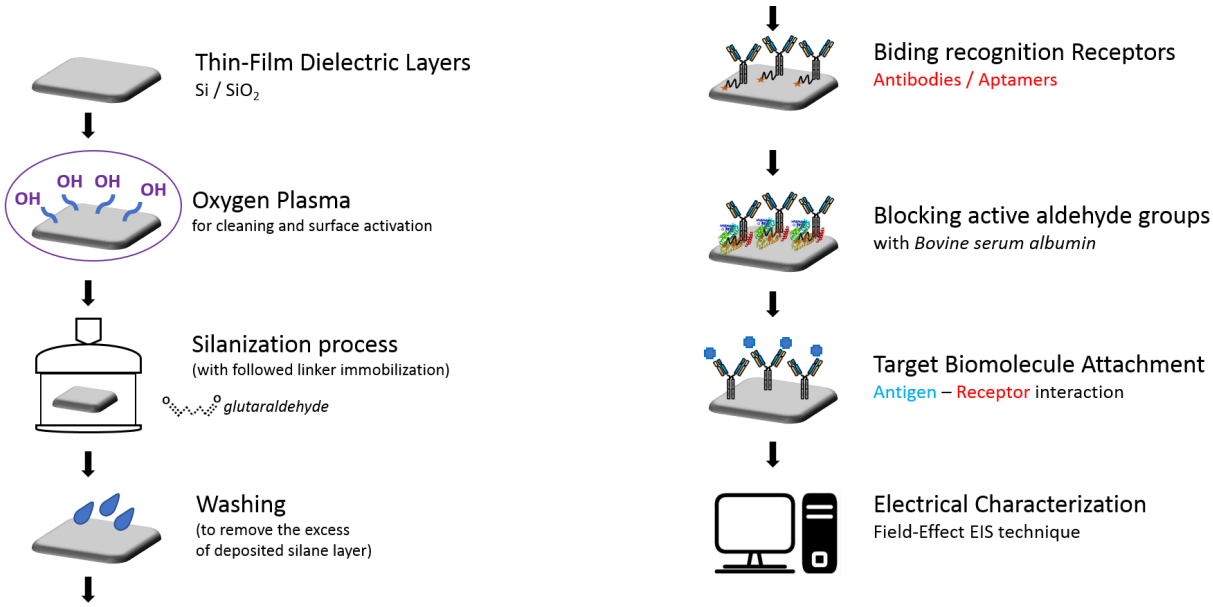

Figure 3.7: First developed immobilization Protocol with functional layers for attachment of biomolecules.

Traditionally, adsorption of albumin from bovine serum (BSA) has been used for this purpose [48]. To reduce non-specific binding, the surface was blocked with bovine serum albumin dissolved in PBS for 30 min. After performed investigation, the immobilization protocol with functional layers is developed and the protocol is schematically shown in Fig. 3.7. However, several intrinsic features of the blocking molecules have to be taken into account. Being a protein, BSA is much more sensitive to temperature and pH variations, which may lead to the denaturation of the protein. BSA may hinder the attachment of target proteins because of its size (3.5 nm x 7 nm x 7 nm), causing antibody binding sites to become obstructed by BSA molecules. Moreover, when there is a coating of the sensor surface with a large number of functional layers, and with the applied large amount of chemical reagents, it will affect the properties of the used sensor surface. The thickness

of the surface is also changed, which is critically while performing the electrical measurements with the target biomolecule. Additional surface modifications can change the contact wetting angle, i.e., make the surface more hydrophilic or more hydrophobic. Moreover, the contact wetting angle of the surface also indicates changes in the structure of the surface, it's roughness or smoothness. As it was mentioned earlier, the AFM scanning method allows to scan the surface of the material in detail and demonstrate the state of surface roughness.

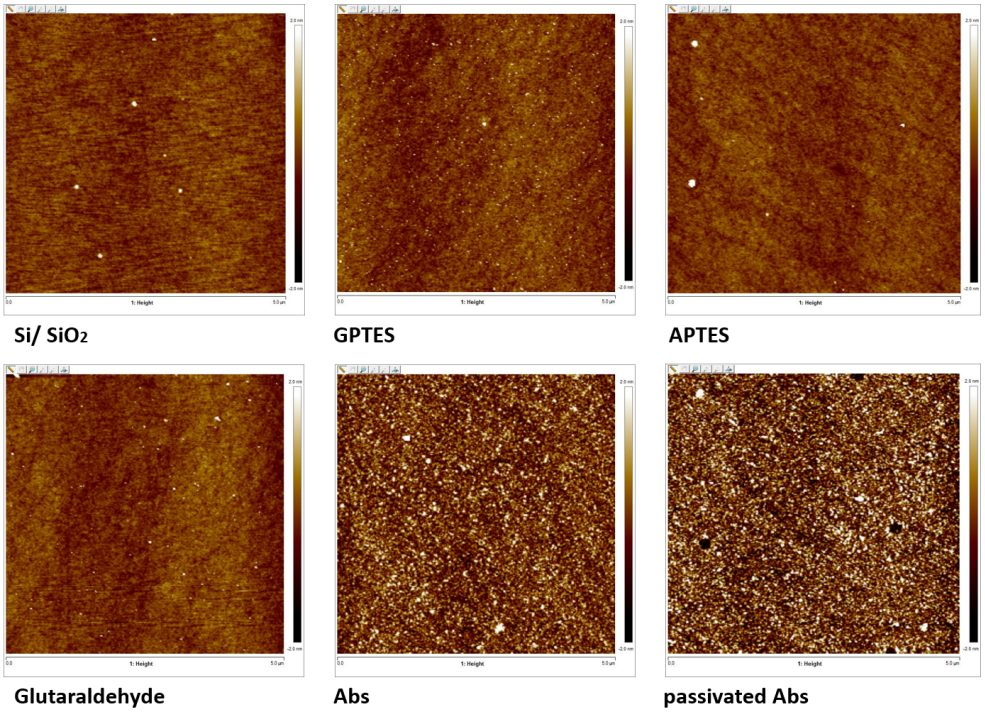

Figure 3.8: Scanned AFM images of chemically introduced functional layers of silanes and cross-linkers on thin-film silicon oxide sensors.

In order to control the changes in the surface roughness during the immobilization process with functional layers the next experiment was performed. On a few specifically selected thin-film dielectric silicon oxide layers with the same thickness, different immobilization protocols were performed. Using the AFM technique, surfaces were screened after various treatments with functional layers, as shown in Fig.(3.8).

Table 3.4 shows obtained roughness values for the modified thin-film dielectric silicon oxide surfaces. From the Fig.(3.8) and Table 3.4 one can see that the introduced silanes do not make strong changes regarding the state of surface roughness. Cross-linker glutaraldehyde results in increasing the roughness. The antibodies were

Table 3.4: AFM scanned results with roughness values of 5x5 um surface resolution for introduced functional layers

Sample 01 SiO_2/Si	Sample 02 APTES	Sample 03 GPTES	Sample 04 GA	Sample 05 mabs	Sample 06 mAbs+BSA
0.248 nm	0.258 nm	0.286 nm	0.301 nm	0.711 nm	0.900 nm
0.238 nm	0.254 nm	0.288 nm	0.299 nm	0.712 nm	0.944 nm

added step by step onto the silane layers, as described in the immobilization protocol. The scanned part with immobilized antibodies shows a high amount of attached receptors on the surface. This result indicates the effectiveness of the developed immobilization protocol. However, introduced BSA blocking agent for blocking active aldehyde groups creates an agglomeration on the surface and hinder further attachment of target proteins. Therefore, for further experimental use of the immobilization protocol with functional layers, the investigations of another blocking agent were performed. As an alternative, the ethanolamine blocking agent was found to prevent a non-specific binding [49]. In contrast, the antibody-immobilized surface capped with ethanolamine agent has maintained it's binding capacity for the target protein [50].

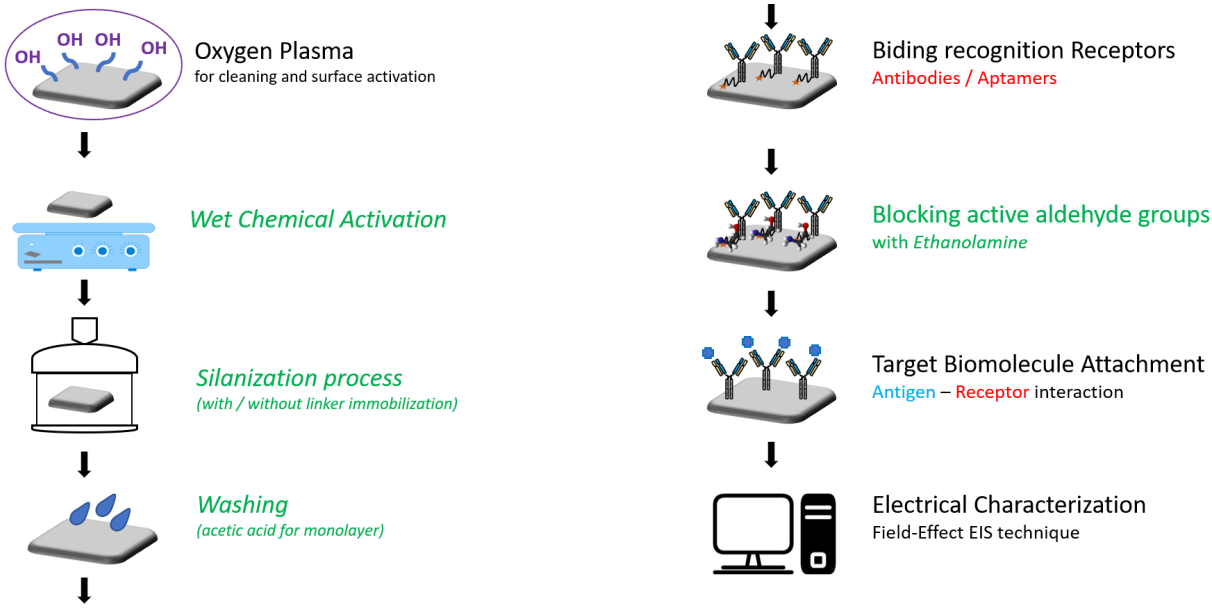

Figure 3.9: Improved immobilization Protocol with functional layers for attachment of biomolecules.

In connection with the description above, the immobilization protocol with functional layers has been improved, as is shown in Fig. 3.9. For surface cleaning and

activation, the oxygen-induced plasma and wet chemical activation were combined. This combination provides perfectly clean and hydroxyl activated groups all over the sensor surface. Acetic acid provided smooth mono-layer of silane and led to amine-functionalized surfaces with greater reactivity. Ethanolamine was used for maintenance binding capacity of the target molecule. This improved protocol was used for all subsequent and further functionalization procedures as well as for electrical measurements both on thin-film dielectric oxide layers and silicon nanowire-based sensors. In the next chapter, I will introduce developed novel approach for contactless characterization of important biological liquids using resonator technique.

Chapter 4

Contactless WGM Biosensors for Antioxidant Biomarker Detection

The resonant phenomenon is originated from the acoustic field, firstly produced and observed in a musical instrument, when strings were vibrating to produce sound without direct player participation. Resonance phenomena occur not just in musical instruments, but in all other types of vibrations waves. There is a mechanical resonance, that can cause violent swaying motions by absorbing more energy when the frequency of its oscillations matches the system's natural frequency of vibration than it does at other frequencies. Acoustic resonance describes the diapason of human hearing. Although, acoustic resonance can occur at frequencies outside the range of human hearing, where acoustic systems amplify sound waves whose frequency matches one of its own natural frequencies of vibration. Well, known the string resonance, which is fundamental and occurs on string instruments. Strings or parts of strings in musical instruments may resonate at their own frequencies when other strings are sounded. Electrical resonance occurs in a circuit with capacitors and inductors under influence of the magnetic field, which generates an electric current. An optical resonance can occur in a build system of mirrors in the form of a standing wave. Light reflecting multiple times in mirrors producing standing waves for certain resonant frequencies. Produced standing waves are called "modes". There are also other types of resonances and resonant systems (orbital, atomic, particle, molecular, and e.g.). In such systems, resonance phenomena occur when the frequency of periodically applied force is equal to one of the natural system frequencies. This causes the system oscillation with a larger amplitude than the case of the applied force at other frequencies [51]. Resonance frequencies correspond to

a relative maximum of resonance response amplitude [51]. In electrical or optical systems, the resonant phenomenon occurs as described but it critically depends on the interactions between different parts of the resonant system. as well as on the precise geometrical properties. Material selection and sensing resonance modes are the crucial factors in any sensor design. And as a consequence, a high motivation to search for novel materials in order to improve the sensor performance. Recent developments in this context for sensing purposes include the use of titanium dioxide (TiO_2), silicon nitride (Si_2N_3), silicon carbide (SiC), hydrogenated amorphous silicon, poly(methyl methacrylate) (PMMA), polydimethylsiloxane (PDMS), sapphire. Such resonances are termed morphology-dependent resonances (MDRs).

Light in a resonator cavity will reflect multiple times due to the interference effects. However, only certain frequencies of confined light will be sustained by the resonator, while others being suppressed. Patterns reproduced on every light round-trip of a resonator cavity, are the most stable among the other. Examples of the main modes are shown in Fig.4.1. Those modes of a resonator are known as eigenmodes.

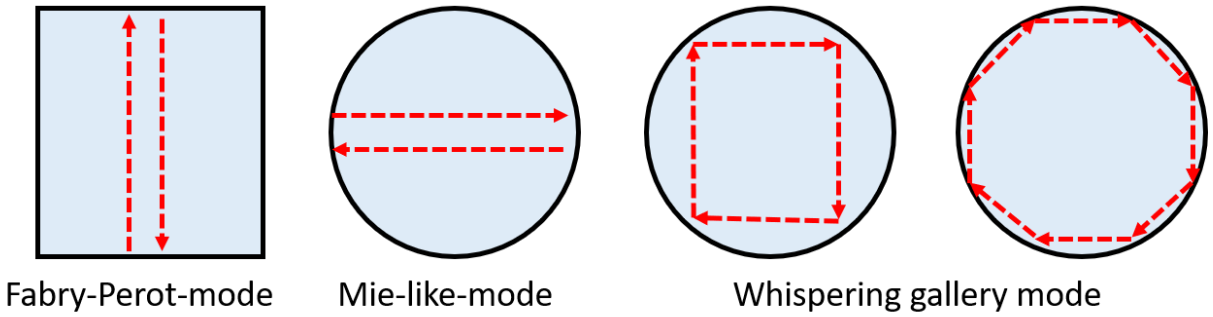

Figure 4.1: Classification of eigenmodes of a dielectric resonator.

Resonator modes can be divided into two groups of modes: longitudinal modes, which differ from each other in frequencies, and transverse modes, which differ in both frequencies and the intensity pattern. The fundamental transverse mode of a resonator is a Gaussian beam [52]. One of the most famous examples of morphology-dependent resonances is a whisperer gallery mode resonance (WGMs) [51]. Firstly, this resonance mode was discovered in the building of St. Paul Cathedral in London. John William Strutt, better known as Lord Rayleigh, explained that sound waves create modes traveled around in a closed concave surface, as shown in Fig.4.2.

Such modes are guided by reflections with repetition rate, and, if do not consider

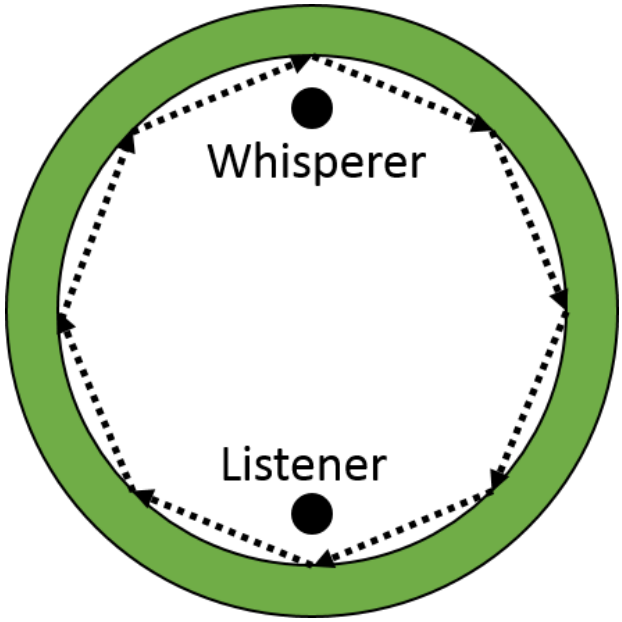

Figure 4.2: Schematic distribution of whispering gallery wave in galleria of St. Paul's cathedral in London.

the adsorption, dispersion of material and scattering, continue to travel infinitely in a geometric perspective. However, there are the losses through the surface of the material are present due to the tunneling effect into the surface layer of the material. In the absence of external excitation, the WGM mode experiences a decay in amplitude. In general, the WGM is representing a class of resonances characterized by their high-quality factors, which also indicates the losses in the material. Moreover, WGMs can also occur in close optical systems and cavities. Ring, disk, cylinder, and spherical cavities are the simplest WGM variants of possible resonator geometries.

4.1 Material selection with Resonator Modes

The WGM resonators can have an extremely high-quality factor (Q) that makes them promising devices for applications in optoelectronic and experimental physics. These resonators are attracting considerable research activities toward further applications, improved fabrication, and theoretical considerations. Several theoretical predictions and experimental studies have been performed regarding resonator geometries. An important goal in developing biomedical detectors and biosensors in science is the ability to detect single molecules and their interactions. One of the

possibilities to achieve the single molecule level is the optical micro-cavities that use WGM modes. To understand better the nature of whispering gallery modes in resonators, it is necessary to understand the main parameters which are describing the resonator itself. A fundamental understanding of WGMs is a prerequisite of the development design strategy for biosensor. The power stored in a WGM, P(ω), exhibits in a Lorentzian line-shape and defined by:

$$P\omega = P_0(\frac{(\gamma_0/2)^2}{(\omega - \omega_0)^2 + (\gamma_0/2)^2} \tag{4.1}$$

The principal parameters describing the WGM resonance are resonance frequency ω_0, full-width at half maximum γ_0, and amplitude P_0 [53]. Commonly, the quality factor $Q_0 = \omega_0/\gamma_0$ is also used to characterize a resonance. Since the energy is trapped within the cavity observation of stored power in a WGM is not feasible [54]. Then excitation of WGMs has to be inferred experimentally and performed for measurements resonator parameters. One common strategy is the monitoring of the excitation response. For example, evanescent coupling to WGMs can be achieved by bringing an adiabatically tapered optical fiber close to the resonator surface [55]. By monitoring the transmitted power of the excitation light launched into the fiber as function of the frequency of incident light, a characteristic Lorentzian resonance shown in Fig.(4.3) can be observed.

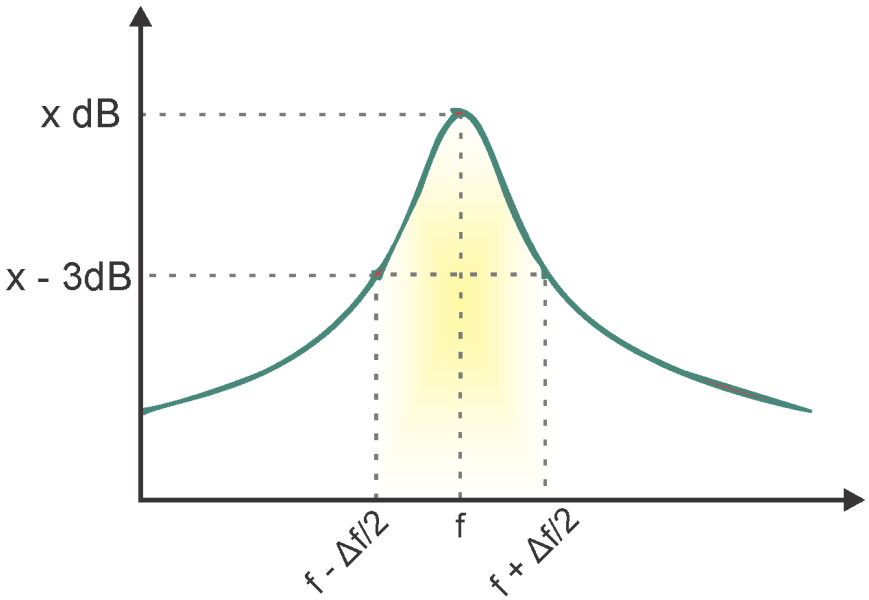

Figure 4.3: Quality factor determined as disturbed evanescence field from electromagnetic field in the resonator.

Prism-coupling strategies, in which WGMs are excited either through an incident propagating beam or evanescent field through the total internal reflection of light from a prism, can be used. In these approaches can be monitored the transmitted and reflected powers. A discussion of the relative advantages of these, and other, coupling schemes can be found in [51]. Total resonance line-width is influenced by losses, radiation, surface scattering, and material absorption. Accordingly the full-width at half maximum of the WGM resonance and inverse of a quality factor depends not only on the material properties but also on the resonator size. In general, the operational principle of WGM sensors is to monitor changes in the WGMs spectral properties prompted by a physical change in the system. From an application point of view, such changes could arise from temperature variations, pressure waves, to the introduction of gas or biomolecules. Electromagnetic sensing follows via induced changes in resonator systems, and as a result, in the resonance frequency or line-width. Shifts in resonance frequency occur when the refractive index is varied. However, induced shifts depend on resonator sizes. Dielectric cylinder and disk (cylinders with small height) resonators are also support whispering gallery modes, as it was modeled and it is shown in Fig.(4.4):

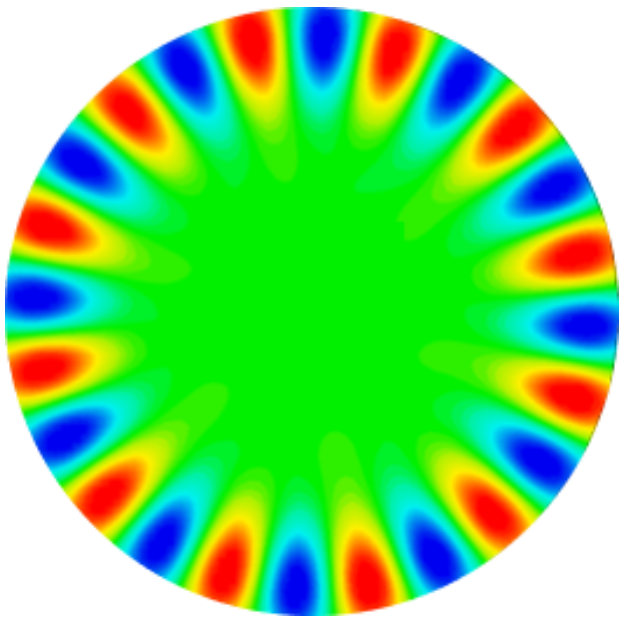

Figure 4.4: Typical electro-magnetic field distributions corresponding to a WGMs mode. An example is obtained by modeling.

To reduce scattering losses from material defects, different proposed fabrication methods were studied. To overcome high losses and limitations, it‘s possible to allow

the WGM mode to be pushed away from the scattering surfaces when shallow wedge angles are used. The natural existence of WGMs in closed optical cavities relies on a total internal reflection at the cavity interface. Low refractive index contrast facilitates the extension of the mode profile beyond the confining of the resonator medium into the sensing domain, thus potentially allowing the utilization material of the resonator as a sensor. Larger refractive index contrasts between the cavity and the host, therefore, help to minimize losses via stronger confinement of the WGMs and thus improve the value of Q factor. Absorption and surface scattering, however, also play a key role in determining mode line-width. The imaginary part of the eigenvalue of the wave number associated with a resonance determines the decay caused by following. Unlike a flat surface, the total internal reflection forms a curved surface which leads to a radiation of the wave from the dielectric round resonator. Corresponding to this phenomenon we define a quality factor:

$$Q = \frac{f}{\Delta f} \tag{4.2}$$

$$\omega = \omega^{'} + j\omega'' \tag{4.3}$$

$$\omega^{'} = 2\pi f \tag{4.4}$$

$$Q = \frac{\omega^{'}}{2\omega''} \tag{4.5}$$

A resonator system where the low value of quality factor ($< 1/2$) is overdamped: the system does not oscillate and the system is displaced from its equilibrium output asymptotically returning to its exponential decay. With the high value of the quality factor, the slower decay becomes stronger and dominates in the system response. The system‘s output responds by rising toward an asymptote. A resonator system with a value of quality factor ($> 1/2$) is underdamped: oscillation combines specific frequency with a decay of the amplitude signal. Underdamped systems with a value of quality factor little above 1/2 may oscillate once or twice before dying out. With increasing of the quality factor, the relative amount of damping decrease. In general, the output of the second low-pass filter with a quite high value of the quality factor, responds by quick rising and oscillating around. Intermediate value of quality factor

(= 1/2) is critical. Like in the case of overdamped system, the output in those systems approaches in a steady-state. However, like for an underdamped system, the output of the system responds quite quickly. The critical situation becomes with the approach to the final value. Real resonance systems usually allow overshoot of an initial response. It requires a slower initial response in order to provide a safety margin. The phase margin of the system sets the value of the quality factor. With the decreased system response, the quality factor becomes high and more oscillatory. With the weak coupling, the regime is the perturbation theory is valid. It can be shown that with the material or solution introduction in the evanescent field, electric permittivity changed.

4.2 Perturbation Theory

Evanescent coupling occurs when we bring a structure possessing a quasi-optical evanescent field in the vicinity of the resonator so that the evanescent fields of the resonator and the coupler overlap significantly like it is shown in the Fig.4.5. This then enables the tunneling of the wave field from the coupler (prism, tapered fiber) to the resonator and back (in complete analogy with quantum tunneling in quantum mechanics) and can be much more efficient than free wave coupling.

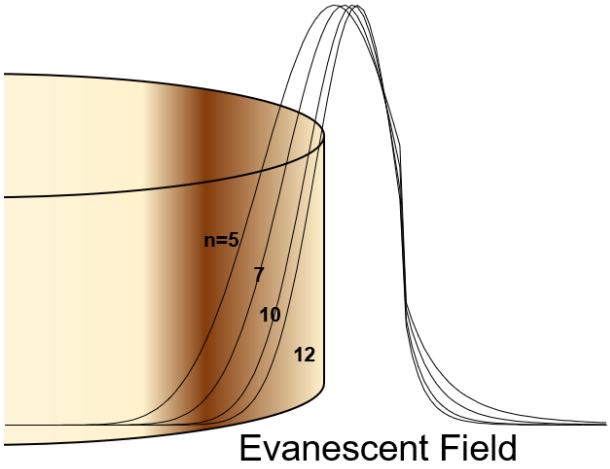

Figure 4.5: Distribution of evanescence field from a disk shaped dielectric whispering galley mode resonator.

Since the evanescent field of whispering gallery modes extends beyond or above a surface outside the resonator, modes are affected by the environment in which the resonator is placed. The environment affects both the resonant frequencies as well

as the quality factors of whispering gallery modes. Because whispering gallery mode resonators can have extremely large Q-factors, and small line width, the line shape shown in Fig. 4.3, is an important informative parameter which is easily measured. This means that the resonators act as very sensitive sensors.

For the concept of material studies, including bioliquids, when a resonant cavity is perturbed, e.g. by introducing a foreign object with distinct material properties into the cavity or when the shape of the cavity is changed slightly, electromagnetic fields inside the cavity change accordingly. The underlying assumption of cavity perturbation theory is that electromagnetic fields inside the cavity after the change differ by a very small amount from the fields before the change. Then Maxwell's equations for original and perturbed cavities can be used to derive expressions for the resulting resonant frequency shift [56]. Perturbation theory generally considers stored energy and lies on classic formulas. The maximum change occurs in resonance frequency when the small perturbations are placed at the maximum of intensity. Such behavior explains only for high-valued quality factors, and only when predicting the spectral shift of the resonance frequency.

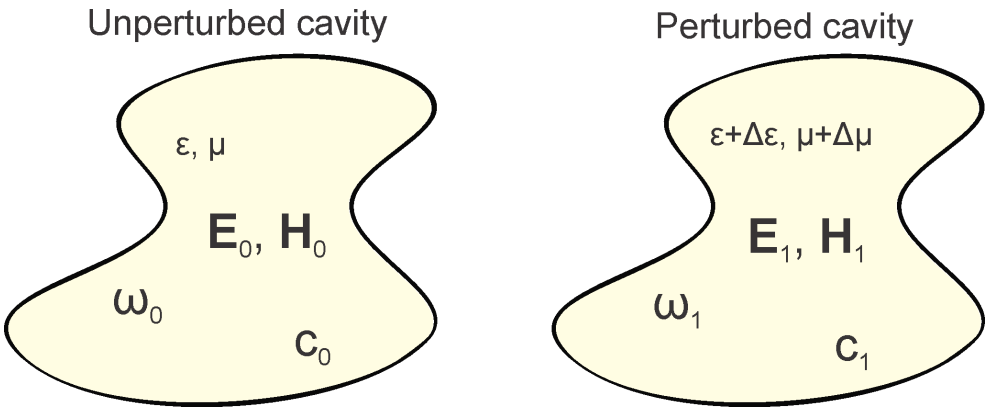

Figure 4.6: Frequency shift by the means of disturbed evanescence field from electromagnetic field in the resonator.

It is furthermore well known that WGM resonators possess a degeneracy between counter propagating WGMs, which can in specific circumstances act to give rise to an effective broadening. If a small molecule or nano-particle enters the evanescent field, the coupling between the modes is introduced. Accordingly, the system eigenstates now correspond to two orthogonal standing wave type modes in the resonator. As can be seen from Fig. 4.6, a material used for fabrication of resonance systems that material also influences on the electro-magnetic field. When the material is changed,

which means that permittivity and permeability are corresponding changes, the resonant frequency can be approximated as:

$$\frac{\omega - \omega_0}{\omega_0} \approx \frac{\iiint_{\Delta V}(\mu|H_o|^2 - \epsilon|E_o|^2)dv}{\iiint_V(\mu|H_o|^2 + \epsilon|E_o|^2)dv} \tag{4.6}$$

Where the isotropic permeability is

$$\begin{aligned} \boldsymbol{B} &= \mu_0(\boldsymbol{H} + \boldsymbol{M}) \\ &= \mu_0(\boldsymbol{H} + \chi_m \boldsymbol{M}) \\ &= \mu_0(1 + \chi_m)\boldsymbol{M}) \\ &= \mu_0\mu_r \boldsymbol{M} \end{aligned} \tag{4.7}$$

and isotropic permittivity is

$$\begin{aligned} \boldsymbol{D} &= \epsilon_0 \boldsymbol{E} + \boldsymbol{P} \\ &= \epsilon_0 \boldsymbol{E} + \epsilon_0 \chi_e \boldsymbol{E} \\ &= \epsilon_0(1 + \chi_e)\boldsymbol{E} \\ &= \epsilon_0 \epsilon_r \boldsymbol{E} \end{aligned} \tag{4.8}$$

Perturbation in the resonator system can also produce changes in the linewidth of the resonance. If a small molecule enters the evanescence field, then coupling between the modes is influenced. For a single perturbing molecule, the WGM‘s mode overlaps with the molecule, shifting the frequency of the WGM and introduce additional losses, as shown in Fig.(4.7). The total effective broadening is dependent on the coupling strength. We focus our attention on the calculations of all important parameters for creating a sensitive biosensor with WGM modes below.

4.3 Microfluidic fabricator for WGM Biosensor

The relative dominance of each contribution depends not only on the intrinsic material properties and fabrication quality but also on the resonator size. Specifically, for small resonators, radiative losses dominate, while as the resonator size increases absorption losses in the host medium play a more prevalent role. As the size increases even further the WGM becomes more confined within the cavity such that the material properties of the cavity govern the final, ultimate, material limited

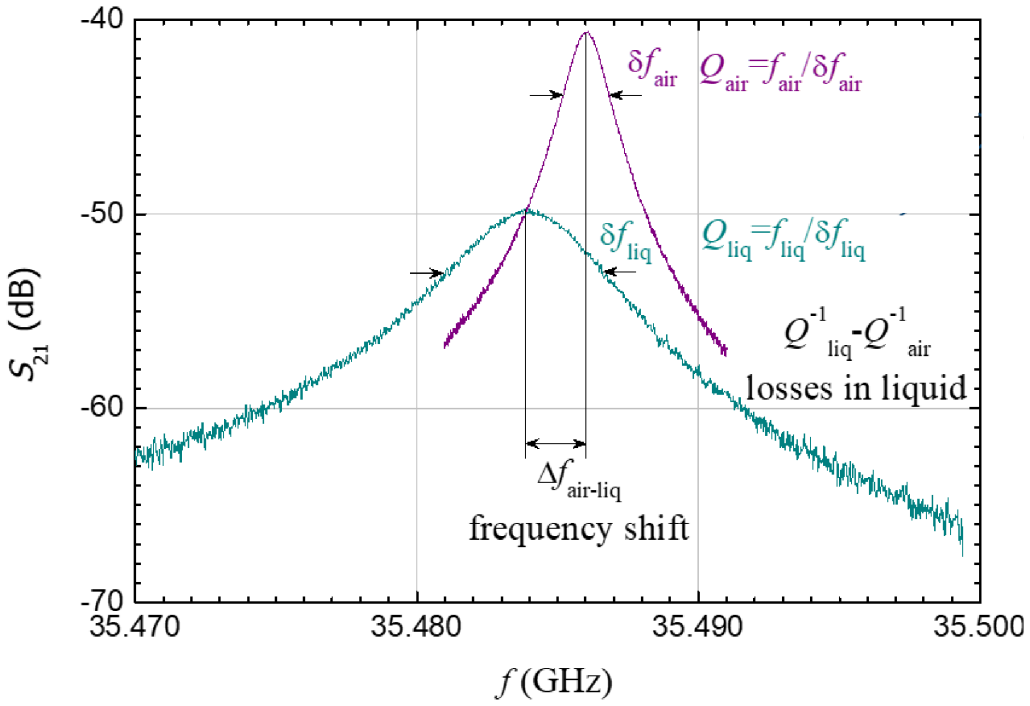

Figure 4.7: Example of changes in resonance shape due to introduced losses by a liquid in the microfluidic channel.

quality factor, where the refractive index of the resonator associated with absorption coefficient. Any given WGM resonator, however, can support multiple WGMs of different order as shown in Fig.4.4. We focused our interest on disk resonators, particularly on the disk resonators with a circular hole in the middle. Since whispering gallery modes are already highly localized at the cavity-air interface, disk resonators have almost the same whispering gallery modal structure as cylindrical resonators 4.4, while higher order radial modes are much better suppressed. An additional advantage of disk resonators is that they allow for many times smaller mode volumes, at only a fraction of the volume of the dielectric material.

As it was mentioned in the section before, the dimensions of the dielectric resonator are the main crucial criterion for the design, as well as losses and sensitivity. To study the effect and influence of these parameters on the resonator geometry, simulations in COMSOL Multiphysics were performed. The calculation model is based on a consideration of the sapphire disk resonator. The proposed model was realized in the Radio-frequency (RF) mode using the eigenfrequency mode stimulation. All simulated model parts were divided into the tetrahedral mesh elements. The HE 12 1 1 mode used for measurements has twice degenerated on the azimuthal index in

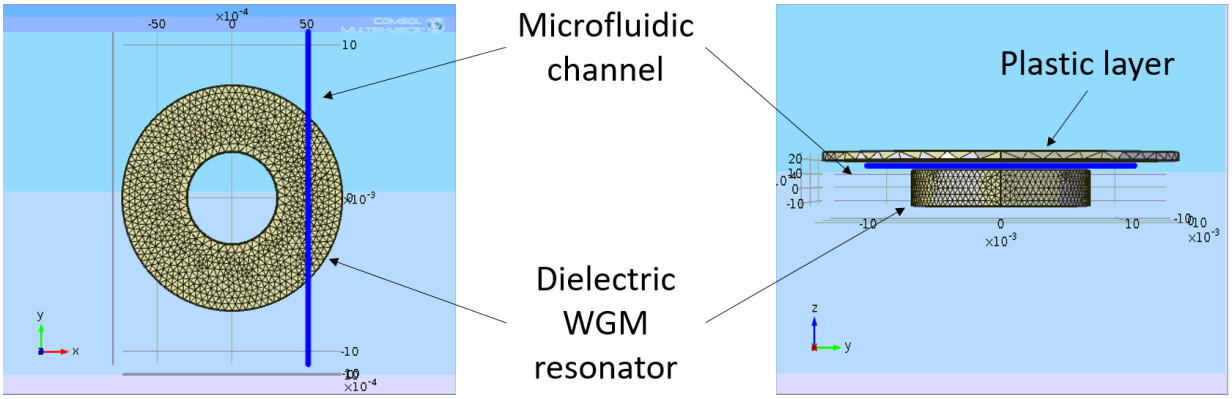

Figure 4.8: Modeling Whispering-Gallery-Mode resonator with microfluidic channel.

the resonator without a microfluidic. However, since the resonator was planned to be used as a biosensor for the detection of liquids and solutions, one of the important tasks was introducing the cavity for the liquid under the test. This task was also simulated in COMSOL in order to find a suitable cavity for the liquid under the test. It was critically important that the liquid in the vicinity of the cavity of the resonator electromagnetic field should introduce minimal losses. As shown in Fig. (4.8), it was decided that the best way to introduce the liquid to the sensitive field of the resonator is in the microfluidic channel. It should be taken into account, that the position tuning of microfluidic channel should consider the radiation losses in the resonator have to be less than total losses by introduced liquid.

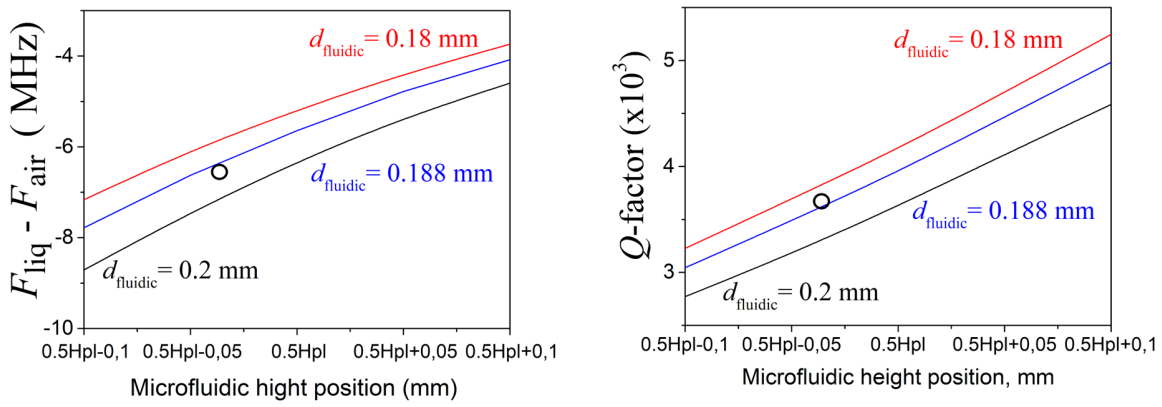

Figure 4.9: Frequency and Q-factor determination of calibrated microfluidic position.

Results of the calculated and corrected geometrical values of the microfluidic diameter are 0.19mm. Microfluidic was placed from the middle of the resonator height and located in the direction of the resonator by 0.03mm. In a WGM resonator

with a simulated filled microfluidic channel, degeneration is removed and the HE 12 1 1 mode splits. The first HE 12 1 1 split mode has a resonant frequency of 35.39268 GHz with a quality factor of $Q = 3500$. The second one has a resonant frequency of 35.39294 GHz with the quality factor of $Q = 3930$. The results of calculations for the two modes were averaged to obtain a single peak. Simulation and calculations are allowed us to understand the optimal geometrical position of the microfluidic channel for the tested liquids, as shown in Fig. (4.10). However, if we talk about real conditions and position, we must take into account that the microfluidic channel must be made from some material. And not just from any material, but a specifically selected material that would satisfy all requirements like good quality, low losses, availability, liquid resistance, long-term usage. The calibration procedure was introduced to obtain accurate geometric parameters of the real microfluidic channel filled with the liquid and its position in the plastic layer. The plastic Zeonex 480 Cyclo Olefin polymer (COP) was considered as a suitable material for microfluidic fabrication. Zeonex 480 COP is an engineered plastic material that provides excellent optical properties such as high transparency, low absorption, high precision molding, low dielectric constant and dielectric tangent.

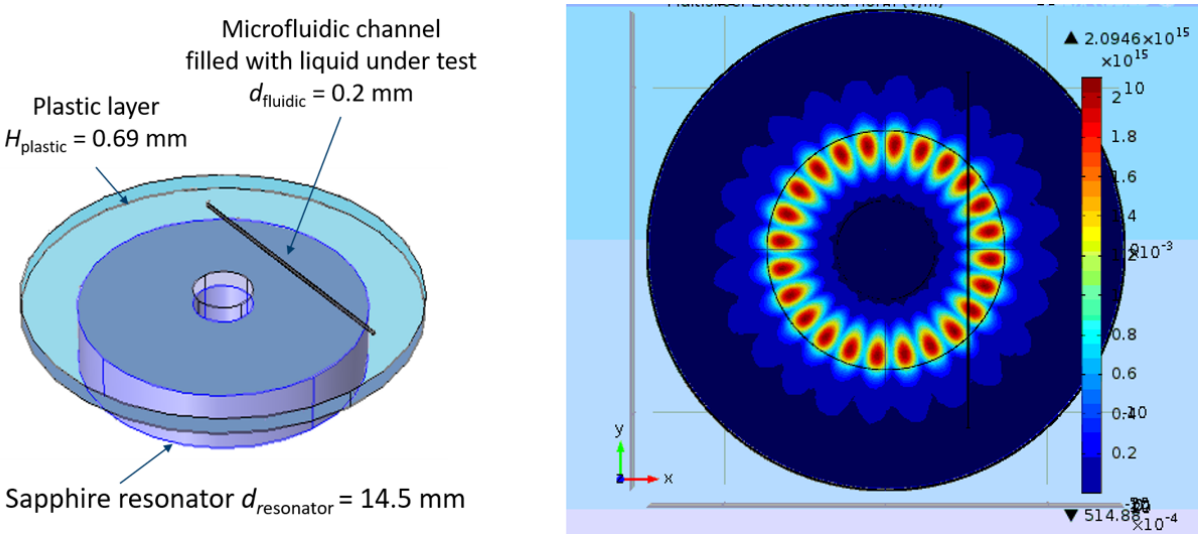

Figure 4.10: Simulated model of dielectric disk resonator with microfluidic channel in plastic layer.

As well, in Fig. (4.10), can be seen that the microfluidic is located directly above the maximums of the induced electromagnetic field and penetrates with the evanescent field. It is worth paying attention to radiation losses. However the resonator was developed for measuring complex permittivity of dielectric bioliquids, the losses

determined by liquids is much higher than other kinds of losses. Resonator radiation losses were calculated by means of the numerical simulation as well as using the program COMSOL. In the program, the matched absorbing layer was placed at some distance from the resonator. At the same time, the analytically calculated quality factor showed that the calculation accuracy of the program COMSOL increased using a number of dielectric layers with different values of complex permittivity [[57]]. In general, when calculating the resonator quality factor, the COMSOL simulation takes into account losses in the dielectric

$$Q_0^{-1} = k \tan\theta + A_S^C R_S^C + A_S^S R_S^S + Q^{-1} \tag{4.9}$$

where $tan\theta$ is the dielectric loss tangent, R_S^C and R_S^S are a surface resistance of the sample under test accordingly, k, A_S^C and A_S^S are coefficients taking into account losses in the dielectric, Q_{rad} is a quality factor.

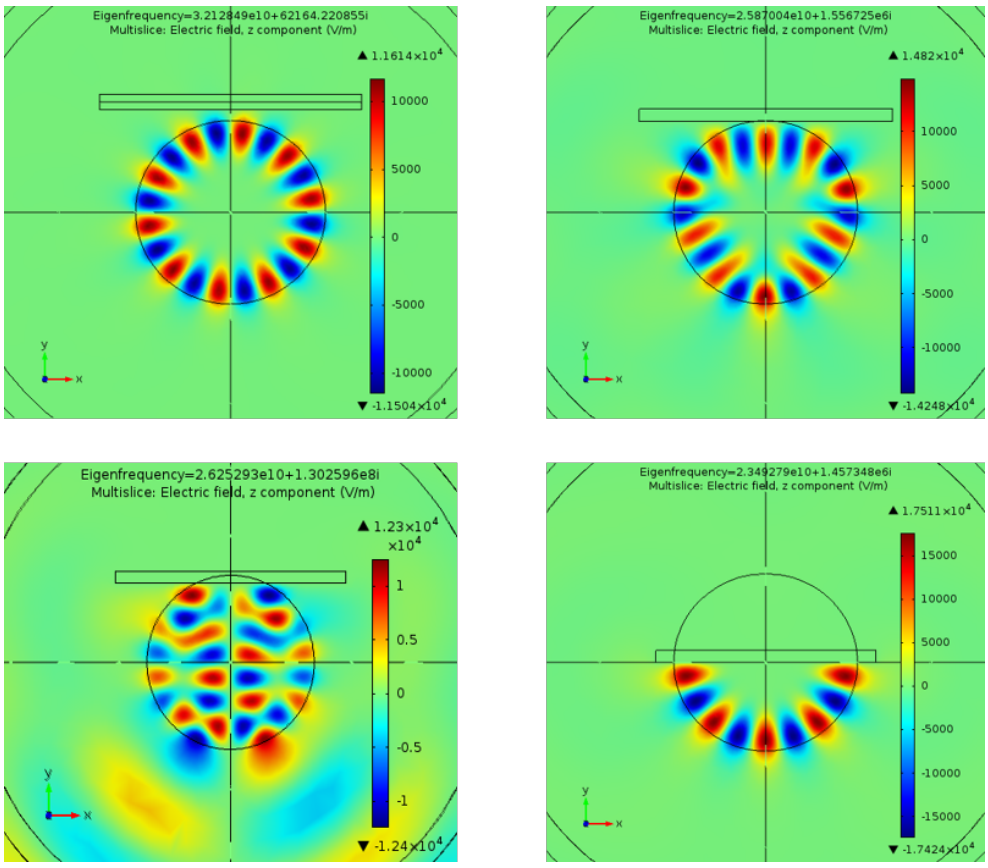

Figure 4.11: COMSOL simulation of finding a more accurate value of acceptable distance between the resonator and waveguides (reproduced from [57]).

The losses in the resonators used for sensor studies have to be less than the

total losses in the dielectric and conductors about one order of magnitude to be neglected. In principle, higher Q-factor may be necessary. The WGM disk of radius 7.25 mm was made of sapphire. The height of the disk and the sample is 2.5 mm. When the sample touches the disk, the value of this distance is equated to zero, and when the sample "enters" into the dielectric disk body (cut disk resonator) the value below 0 (4.11). Numerical studies of radiation losses in sapphire WGM resonators with two and one CEPs were analyzed using the program COMSOL 4.11. Experimental studies were performed for the resonators with one CEP, where the shape of the surface of the dielectric disk can differ from cylindrical shape. All simulations and experiments in this work were focused on Ka-band. It was found, that the introduction of conducting sample under test in the resonator with two CEPs perpendicular to the radius leads to both deformation of WGM field and significant increase of radiation loss. For measurement purpose, the sample has to be located at the distance, which is not less than 1 mm from the cylindrical surface of the dielectric disk. So, in this case, the resonator is a cut disk with two CEPs and with the flat sample pressed to a surface of cutting. The conductor sample has a significant effect on the frequency. Its influence on the radiation Q-factor becomes considerable at distance < 5 mm for the length of 40 mm and < 9 mm for length 4 mm. Obviously, the strong deformation of WGM field at approaching the sample to the dielectric disk and a sharp increase in radiation loss make using of this kind resonator problematic for studies of superconductors or other samples with high conductivity (e.g. graphene [58]). Increasing the distance between the sample and resonator surface to achieve acceptable values leads to decreasing the measurement sensitivity. It is obvious that the superconductor sample has to be placed at a distance, which is not smaller than 1 mm from the resonator. For finding a more accurate value of acceptable distance it is necessary to perform additional studies of the coefficient. Changing of the electromagnetic field distribution is accompanied by a change in spectral and energy characteristics of the resonator. Fig. 4.7 shows the change in frequency and radiation Q-factor of QDR with changing the position of the sample for different values of the azimuthal number n and the sample length. These lines are in a good agreement with the results, obtained analytically [59].

Based on the data obtained during various studies and COMSOL simulations, I fabricated a special set-up, based WGM resonator, yet tuned for biomolecular sensing. The measuring cell is enclosed with protective box in order to reduce noise

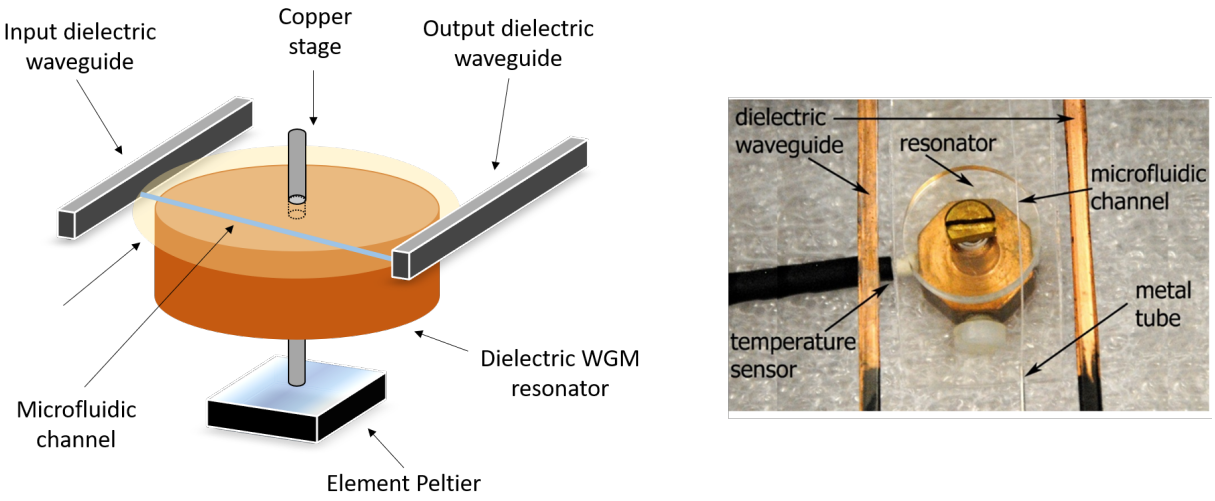

Figure 4.12: WGM-resonator characterization setup (reproduced from [60]).

and external influence of physical parts. Fig. 4.12 shows a schematic representation and "real-life" image of the developed resonator-based sensor. The WGM resonator is made from sapphire material. In the center, the sapphire resonator has a circle, where the copper stage is placed. On top of the resonator, there is a Zeonex plastic layer with a finely defined microfluidic channel. Underneath the resonator is the Peltier element is placed. Some bioliquids are stable under certain conditions. Temperature is one of the main conditions that is specifically monitored during the measurements. Temperature sensors (PT1000) placed directly near the resonator and provide the possibility to precisely control the temperature inside of the closed measurement box. Dielectric waveguides are used to induce the electromagnetic field in the sapphire resonator, while the copper stage is holding sensing systems in the order. The measurement cell was specifically designed for testing various biological liquid: simple and complex. It is well known that to get accurate results, it is highly important to properly prepare and configure the system before measurements. The best simplest way to calibrate the device is to perform a measurement on solutions with well-known parameters and permittivity values.

Such known liquids as water, acetone, methanol, ethanol, and propanol were used for measurements. Measured values of frequency and quality factor with air were used as a reference for measurements with liquids. From Fig. 4.13 one can see the calculated shift of frequency values and Q-factor values. These linear-defined dependences shown changes in measured frequency values and Q-factor values by air-reference. Plotted data points helped to obtain the real and imaginary parts

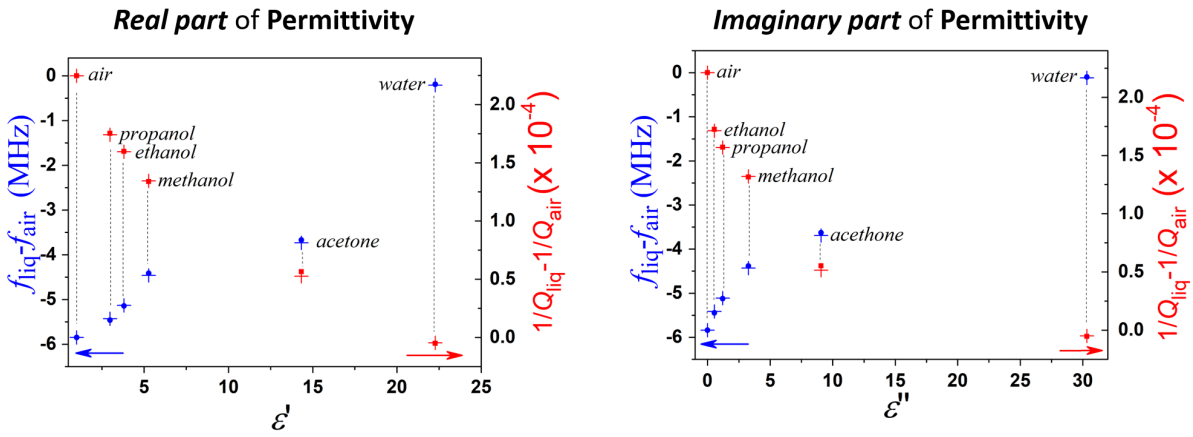

Figure 4.13: The measurements of the relaxation time the different biological liquids (reproduced from [61]).

of liquid permittivity, which is in a good agreement with real data. Particularly attractive for biosensing applications is the capability of a WGM sensor to detect biomolecules in a label-free manner, that is, without requiring any chemical modifications of the analyte molecule. Furthermore, the probing light usually does not alter the biophysical properties of the biomolecule, such as its binding kinetics. Specific detection with WGM sensors then relies on the recognition of the target analyte by molecular receptors, thereby producing WGM frequency shifts specific to the analyte molecule, which thus necessitates the functionalization of the sensor surface. Biomolecular detection can then be achieved by monitoring the binding of analyte molecules to the receptors, in turn transducing interaction and binding events into detectable optical and electrical signals. It is also important to mention that biosensors operate in an aqueous environment since the mechanisms of molecular recognition require water as the solvent. Biosensing covers a broad spectrum of possible uses, ranging from those requiring lower sensitivity, such as detecting the presence of analyte molecules, to quantitative analysis of single particles requiring much higher sensitivities.

4.4 Antioxidant Specific Biomarkers Detection

Reactive oxygen species (ROS) play an important role in the regulatory functions of all biological systems (plants, animals, and humans). These chemically reactive molecules containing oxygen are the product of the normal oxygen metabolism re-

sponsible for a number of reduction-oxidation reactions and cell signaling and homeostasis, controlling stable internal conditions. Under oxidative stress conditions, an imbalance in the ROS level excites the system to detoxify the ROS intermediates and to repair the damaged locations in the cells. For example, ionizing radiation interacts with the H_2O in the human body resulting in highly reactive products such as hydroxyl radicals, hydrogen peroxide, superoxide radicals, and oxygen. The interaction processes of these products with molecules include removing electrons from molecules resulting in their conversion into free radicals, deactivation of specific enzymes, changing macromolecules such as DNA in cells. At the same time, inside the cell, a lot of reactions are found to be responsible for ROS production via electron transport chains.

It is known that an imbalance in oxidation – reduction reactions plays a major role in aging processes and many diseases, such as cancer, diabetes, hepatitis, cardiovascular and neurodegenerative diseases, including Alzheimer and Parkinson. An imbalance of the cell ROS may damage the sub-cellular compartments, including mitochondria and nuclear. This starts the process of programmed cell death by activating free-floating proteins cleaving the proteins of the mitochondria membrane further and starting a chain reaction. The effect of ROS on cell metabolism includes not only programmed cell death but also positive induction of host defense genes and mobilization of ion transport systems, including the implication of mediators in cardiovascular diseases (ischemic injury, stroke and heart attack). Thus ROS are recognized as playing a dual role as deleterious and beneficial species [62, 63]. Any dysfunction of the cell may be recorded as an increase in ROS level causing oxidative stress. In this case, antioxidants – substances that reduce the oxidation of cellular signaling – may return the system to a balanced state.

The regulatory pathways of cells returning to a balanced state display increased the generation of ROS as a common reaction of cells to stress. For example, a high level of ROS can suppress tumor growth through activation of cell cycle inhibitor and induction of cancer cell death. The exact mechanisms in which ROS have a defensive function are not fully understood. However, a direct relation to mitochondria has already been established. Understanding ROS sources and ROS-balance reactions are crucial for the analysis of cell signaling pathways at intracellular and extracellular exchange process levels. At the same time, the mechanism of chain reactions has still not been studied in detail. Once these mechanisms are understood it will be

possible to answer a lot of questions related to diseases in order to apply effective pharmacological treatment in good time.

It is very important to create new methods for detection and characterization of molecules, responsible for reduction-oxidation reactions in ROS-balance reactions. The main aim of this study is the measurement and analysis of characteristic parameters of antioxidant – specific biomarkers in solutions with different concentrations (See Figures 4.14 and 4.15). In this work, we focus on the crucial low-molecular-weight antioxidant-specific markers such as ascorbate and glutathione (see Figure 4.14).

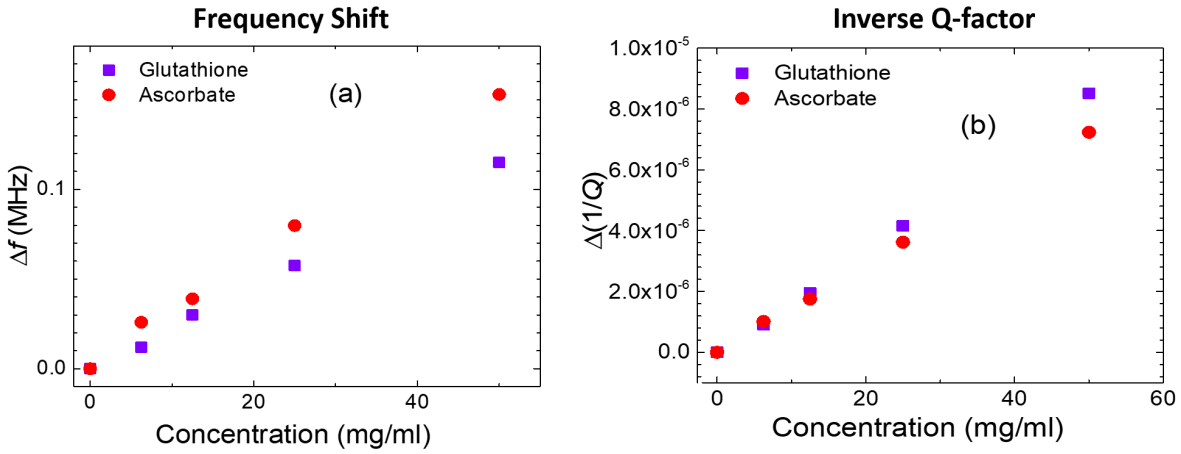

Figure 4.14: The resonant frequency shift and changes in the inverse quality factor as a function of the concentration of sodium ascorbate (red circles) and glutathione (violet rectangles) solutions. (Described in [64])

In the experiment, were used a specially developed calibration procedure and the nomogram chart to extract the absolute values of complex permittivity for liquids under test [61]. The nomogram chart represents a calculated net for the resonant frequency shift and changes in inverse quality factor for a resonator cell with microfluidic channel filled with varied permittivity substances. In such a manner we obtained the real and imaginary parts of liquid permittivity as a function of ascorbate (see Figure 4.15). The dependencies show linear behavior with high sensitivity to the content of biochemical liquids. The real part of the glutathione permittivity decreases at a slower rate with increasing concentration in water solutions than for sodium ascorbate, while the imaginary part demonstrates a stronger dependence. As visible from Figure 4.14, the relaxation time of the glutathione solution is higher than that of the sodium ascorbate solution with an equal concentration. This can

be explained by taking into account the glutathione molecule shape, which is more elliptical than the sodium ascorbate one [65]. The second peculiarity is connected with the ion conductivity of the sodium ascorbate salt solution. The ion conductivity plays an important role in the lower frequencies, but it is still present at 35.5 GHz. This is the reason behind the ion conductivity part adding to the imaginary part of the conductivity and changing the strength of the concentration dependence. In overall, these results indicate a high selectivity for low-molecular-weight antioxidant biomarkers using the real-time microwave resonator technique.

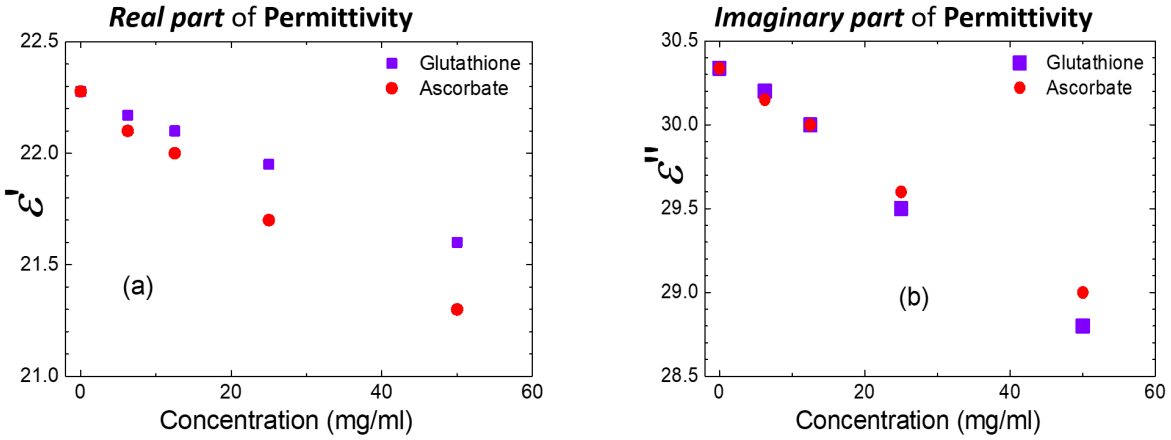

Figure 4.15: Changes in real and imaginary part of permittivity of the liquids with different concentration of ascorbate and glutathione. (Described in [64]

As a summary to this chapter, the WGM resonator technique provides advanced properties not only due to high quality factor of such a structure but also an open resonator system, real-time fast response, reliability, accessibility for the rigorous analysis of electromagnetic field distribution in the resonator, and a controllability of mode coupling with feeder lines. Microwave method does not require labels and provides real-time measurements. Using microfluidic channels in the microwave band allows the contactless measurement of different biochemical liquids that is important for various biochemical applications. For instance, a non-destructive approach for characterization of microwave dielectric response of whole blood was demonstrated for hemoglobin measurements on microlitre samples. In order to characterize ROS scavenging biomarkers, we used ultra-high sensitive microwave WGM resonator technique together with the microfluidic channel. The whispering gallery mode (WGM) optical resonator have only been used for biosensing applications for less than a decade [66], [67], [68] and the performance and limitations of the tech-

nology are still being characterized and debated. It is clear already, however, that these devices exhibit extraordinary sensitivity and show great promise as a future analytical or diagnostic instrument.

Chapter 5

Characterization of Functional dielectric Layers for Cardiac Biomarkers

The operation of a field-effect capacitive sensors based on the electrolyte-insulator (EIS) structures can be described by comparing them with their solid-state analog, metal - insulator - semiconductor (MIS) or metal - oxide - semiconductor structures. Figure 5.1 shows an MIS structure, which consists of a semiconductor substrate (in this case p-type doped silicon) and a metal (or polycrystalline silicon) layer, referred to as gate, separated by a thin insulating material. Typically, the gate insulator is made of silicon dioxide (SiO_2) or a combination of several insulating materials (for instance, SiO_2-Si_3N_4). The insulator is assumed to be ideal, i.e. there is no electrical current passes through. The MIS structure can be considered as a parallel plate capacitor. However, the operating characteristics of the MIS capacitor are quite different. The remarkable property of MIS devices is that the ability to modulate the space-charge distribution in the semiconductor at the interface with the gate dielectric by applying the potential to the gate electrode, thus changing the capacity of the structure.

The simplest EIS-based (bio-)chemical sensor relies on the capacitance change as a result of a biomolecular interaction with the surface of the device. The structure and measuring set-up of the capacitive EIS sensor is shown in Fig. 5.2. It is obtained from MIS structure by replacing the metal gate with an electrolyte. The working point of the EIS sensor is defined by applied through the reference electrode a direct current (DC) polarization voltage, while a small alternative current (AC) voltage

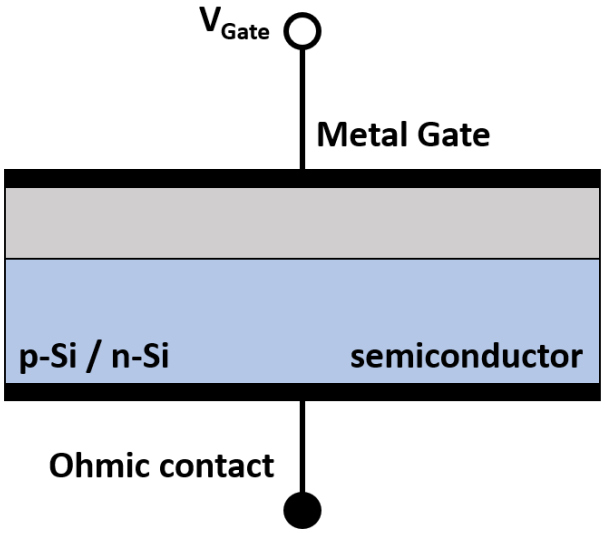

Figure 5.1: MIS structure, which consists of a semiconductor substrate, insulator, and a metal layer.

(∼10–50 mV) is applied to the system in order to measure the capacity of the biosensing device.

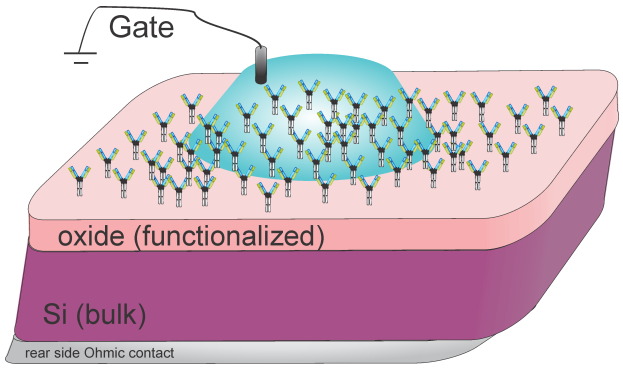

Figure 5.2: The biosensor structure, that is fine tuned for biomeasurement, using MIS the oxide layer is specifically modified with biorecognition sites and an electrolyte is used instead of top gate metal.

The complete AC equivalent circuit of an EIS system is complex and includes, such components as:

- bulk resistance;
- space-charge capacitance of the semiconductor;
- interface impedance at the insulator –electrolyte interface;
- double layer capacitance;

- resistance of the bulk electrolyte solution.

resistance and the impedance of the reference electrode, related to the semiconductor, gate insulator, different interfaces, electrolyte and reference electrode, respectively. However, for typical values of insulator thickness (∼30–100 nm), sufficiently adjusted ionic strength of the electrolyte solution (10^{-4} –10^{-5} M) and relatively high frequencies used, the equivalent circuit of the EIS structure can be simplified. In this case the capacity of the system is mainly determined by the series connection of the insulator capacitance, $C_i = \varepsilon_i/d$ (ε_i, and d are permittivity and thickness of the insulator, respectively), and the space-charge capacitance of the semiconductor, shown in Figure 5.3.

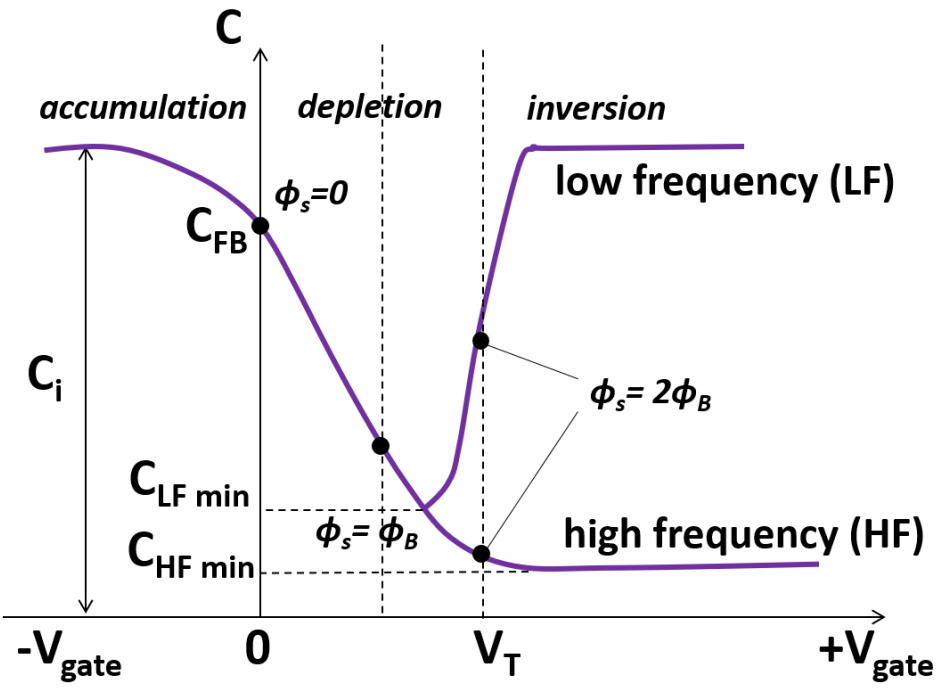

Figure 5.3: The capacitance of a typical MOS (or MIS) device. Regions of accumulation, depletion and inversion defined by measured capacitance-voltage dependencies.

Thus, the expression for the capacitance of the EIS structure, C(ϕ), is similar to the equation for an MIS capacitance, but with a modulation possibility of the flat band voltage and consequently, the space–charge capacitance, $C_{sc}(\phi)$, by means of the electrolyte solution/insulator interface potential and Debye screening length in

electrolyte solutions:

$$\lambda_D = \ Debye\ Length\ = \sqrt{\frac{\epsilon\epsilon_0 kT}{2N_a e^2 l}} \tag{5.1}$$

where ϵ_0 is the permittivity of free space, ϵ is the dielectric constant, k is the Boltzman constant, T is the absolute temperature, e is the elementary charge, and N_a is the Avogadro number.

The insulator capacity with the given thickness is a constant value and represents the maximum capacity of the system, while the capacitances C, C_i and C_{sc}h are usually defined per cm^2 of the surface area. In equation $C_i = \varepsilon_i/d$, for a given insulator thickness d, C_i is constant and corresponds to the maximum capacitance of the system, while C_{sc} is determined by the thickness of the space-charge region in the silicon, which is a function of applied voltage at given doping level of the substrate. Thus, the total capacitance of the EIS structure can be calculated using the following expression as a function of applied voltage:

$$C = C_{ox}\sqrt{1 + \frac{2K_{ox}^2\epsilon_0(V - V_{FB})}{qK_s t_{ox}^2(N_A - N_D)}} \tag{5.2}$$

Assuming that $V_{FB} < V < V_T$ where ϵ_0 is the free space permittivity, q is the electron charge, N_A and N_D are the acceptor and donor concentration of the substrate, V_{FB} and V_T are the flat bang and threshold voltages respectively. C_{ox}, K_{ox} and t_{ox} are the oxide layer's capacitance, relative permittivity and thickness, respectively.

$$t_{ox}^{'} = t_0 + t_{ox}\frac{K_S}{K_o x} \tag{5.3}$$

where K_N and t_N are the relative permittivity and thickness of oxide layer. The flat-band voltage of EIS structure can be defined using the following equation:

$$V_{FB} = E_{ref} - \psi_{ox} + \chi^{sol} - \frac{\Phi_{Si}}{q} - \frac{Q_T}{C_o x} \tag{5.4}$$

where E_{ref} is the potential of reference electrode, ψ_{Si} is a sensitive surface of the oxide, χsol if the surface dipole potential of the solution is presented, Φ_{Si} is the silicon electron work function, and Q_T is the total equivalent charge trapped in the dielectric layers and at the oxide-silicon interface. The threshold is defined then as:

$$V_T = V_{FB} + 2\phi_F + \frac{1}{C_o x}\sqrt{4qN_A K_S \epsilon_o \phi_F} ch \tag{5.5}$$

where ϕ_F is the Fermi energy potential.

The depletion interval is given by the following equation:

$$\Delta V_d = V_T - V_{FB} = 2\phi_F + \frac{t'_{ox}}{K_{ox}\epsilon_0}\sqrt{4qN_A K_S \epsilon_o \phi_F} \tag{5.6}$$

$$\frac{\delta C}{\delta V} \mid_{V=V_{FB}} = -\frac{K_{ox}^3 \epsilon_0^2}{qK_S t_{ox}'^3 (N_A - N_D)} \tag{5.7}$$

Generally, for the characterization of EIS sensors, the mode is used [69]:

- The capacitance-voltage (C/V);

There are three regions curve which can be distinguished in the C/V curve, namely accumulation, depletion, and inversion as it is shown in Fig. 5.3. In the accumulation region, $C_i \ll C_{sc}$, then the capacitance of the entire EIS structure is determined by the geometrical capacitance of the insulator, C=C_i. For a capacitive field-effect sensor application, the depletion region of the C/V curve represents the most useful operation mode. Biochemical detection in this operation mode is implemented as the modulation of the flat-band voltage resulting in the capacitance change (5.4) induced by the particular biochemical reaction at the electrolyte/gate interface. The thin-film dielectric layers have been widely used for the detection of solution's pH value, ion concentration, enzymatic reactions, charged macromolecules as well as action potentials of living cells [70]. The simplest biosensor employing the field-effect is the capacitive EIS sensors with thin dielectric layer, representing a bio-sensitive capacitor. As it can be seen from the curves in Fig. 5.3 (top, left), the C/V curves of the EIS structure are concentration dependent due to the contribution of the potential ϕ at the insulator/electrolyte interface. Described thin-film dielectric EIS sensor is capable of charge sensing, in particular the charges brought to the surface by the charged molecules.

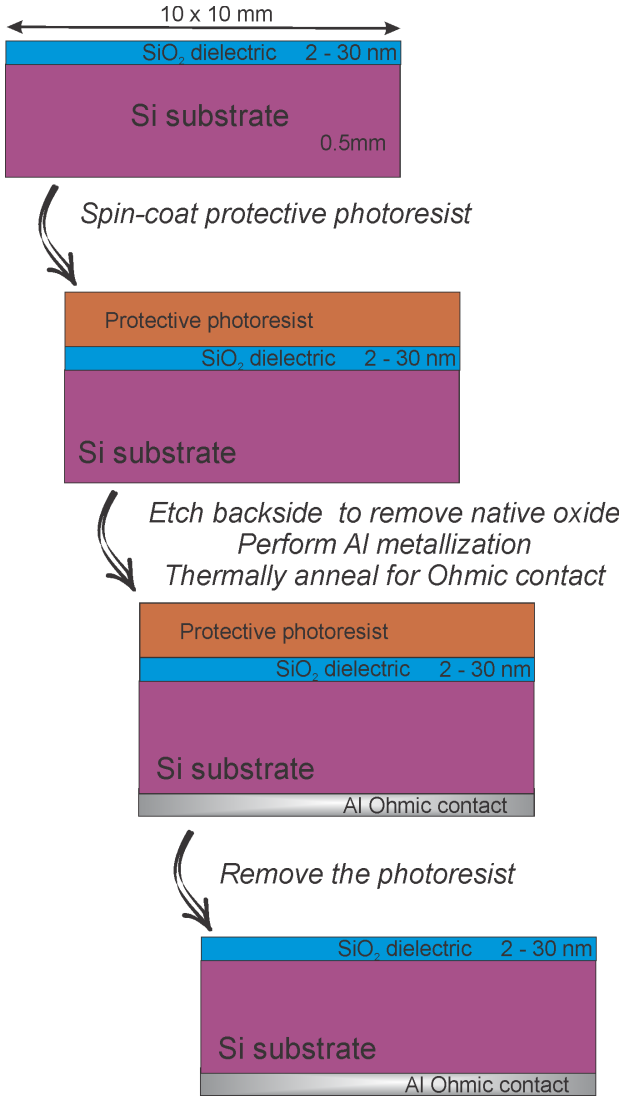

Figure 5.4: Fabrication steps for developed thin-film oxide dielectric layers performed in Helmholtz Nanoelectronic Facility.

5.1 Fabrication and characterization of thin film dielectrics

All fabrication processes were performed at the Helmholtz Nanoelectronic Facility (HNF) of Forschungszentrum Juelich. High-quality n-type and p-type silicon wafers with <100> surface orientation were used as a substrate for EIS structures. Several chemical modification steps were undertaken. Firstly, the silicon wafer was cleaned from organic, inorganic and metal contaminations as well as oxide removal in terms of a standard RCA procedure including SC1, SC2, and dipping in diluted HF solution. A layer of silicon oxide was then thermally grown in a dry oxygen

atmosphere (See Figure 5.4). The thicknesses of thermally grown silicon oxide layer was controlled via Ellipsometry (SE800) technique. The front side of the wafer was protected by applying the AZ5214E photo-resist. Afterwards, the back side of the wafer was chemically etched in buffered-oxide etch (BOE, $7 \div 1$) to remove the oxide layer before the metalization procedure. Later aluminum (Al) was deposited onto the back side of the wafer in order to establish an Ohmic contact with the bulk silicon.

To determine the quality of the fabricated thin-film dielectric layers such methods as ellipsometry, X-ray photo-electron spectroscopy (XPS), atomic force microscopy (AFM), as they provide different types of information about the surface and allow to fully describe the properties of fabricated sensors.

Ellipsometry is an optical technique to measure the transmission and reflection properties of focused light incident on the material. This method uses the elliptical polarization of the light, after transmission and passing through the material. Ellipsometry allows not only to determine the thickness of layers, but also to study the refraction as well as absorbtion properties of the material. The main advantages of the ellipsometry as a tool for material characterization as listed below:

1. Spectroscopic ellipsometry has high precision in wavelength;
2. The measurements are indestructive;
3. Time efficiency;
4. Various parameters can be measured (layer thickness, refractive index, reflection angle, dielectric function tensor);
5. Ellipsometry measures at least two parameters at each wavelength of the spectrum;
6. Measurements are less affected by intensity instabilities of the light source or atmospheric absorption;
7. Ambient unpolarized stray light does not significantly influence the measurement, so no dark box or cover is required;
8. Real and imaginary part of the dielectric function (or complex refractive index) can be extracted.

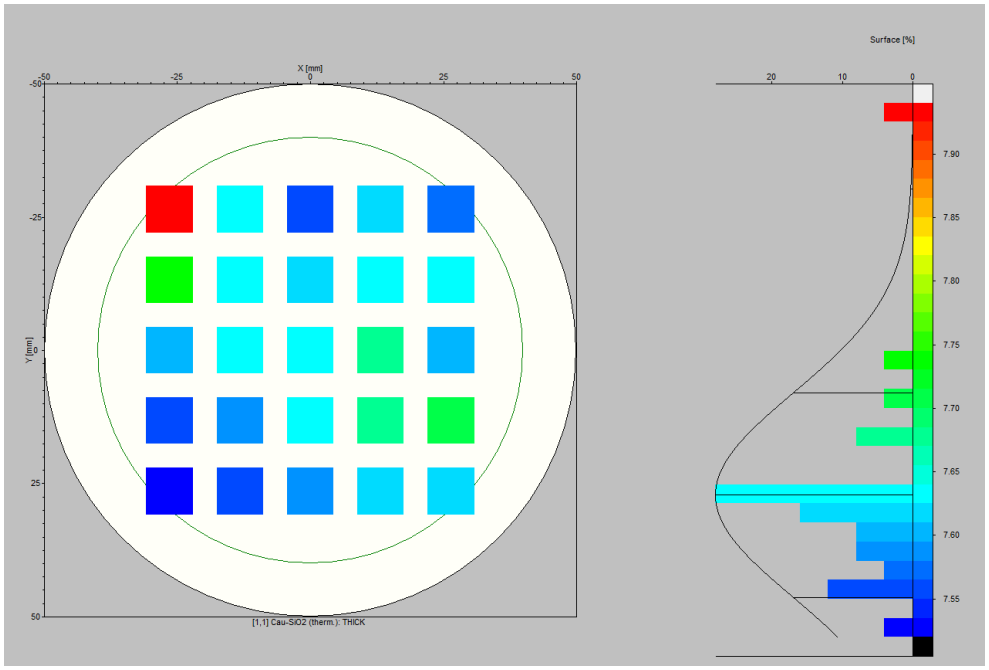

Figure 5.5: Ellipsometric characterization of fabrication wafer for developed thin-film oxide dielectric layers.

Typically, the ellipsometry technique is used in the reflection setup configuration. The change of polarization is determined by the properties of the sample under study: complex refractive index and layer thickness. Compared to most optical techniques, ellipsometry is not diffraction-limited, and allows to achieve the sub-nanometer resolution within the polarization state. The technique is applicable to the materials and films the thickness ranging from less than a nanometer to several hundred micrometers.

Fabricated thin-film oxide dielectric layers were characterized using the ellipsometry technique. As it is shown in Fig.5.5, the measured thickness of thermally grown oxide layer is in a good approximation with the planned thickness and it was determined to be approximately 8nm. The next step was to analyze the components of the fabricated structure.

Since, the fabrication process involves the strong chemicals and polymeric materials, it is important to characterize the structure of the grown silicon oxide on the chemical scale. In order to do that, the X-ray photo-electron spectroscopy (XPS) [71] was utilized. XPS is the most widely used characterization technique that is able to perform surface analysis of the material and provides the quantitative information about the chemical properties of the material. Usually, the XPS spectrum is

obtained by x-ray irradiation of the surface, making the process locally destructible. In parallel with thr irradiation, the kinetic energy is measured, counting the number of electrons that escaped from the top layer of the material (5-10 nm) being under study.

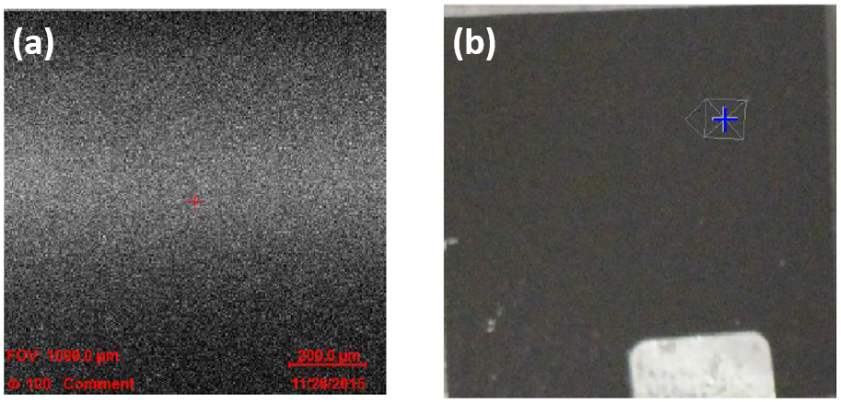

Figure 5.6: Silicon oxide sample prepared for XPS characterization: (a) silicon oxide thin-film dielectric sensor; (b) chosen square for the depth profiling and analyzing;

The Phi5000 VersaProbe 2 instrument (ULVAC-Phi Inc., USA) with the monochromatic source of Al K-alpha (1.486keV) was used for the XPS characterization. Sputter rate for the measurements was calibrated by the depth profile of 100 nm of SiO_2 on Si standard sample. Analysis was performed on a small square (Fig. 5.6), so studied sample should be covered with protective resist, stored in a vacuum and used for addition characterizations only after the resist removing.

Survey spectrum is usually the first starting point of the XPS analysis. This kind of spectrum shows all possible elements presented in the material. It allows to set up the subsequent high-resolution for the spectrum acquisition. The inset in Fig. 5.7 shows a quantification table (right upper corner) indicating all elements found in the sample, their binding energies, and their content expressed in percentage. The average depth resolution for XPS analysis is approximately 5 nm. In principle, this technique detects all available elements with an atomic number (Z) of 3 (lithium) and above. It cannot easily detect several elements such as hydrogen and helium. Typical spectra represent a plot of the detected electron intensity, per unit time (Y-axis, ordinate), versus the binding energy of the detected electrons (X-axis, abscissa). Each element provides a set of characteristic XPS peaks for binding energy values that directly correspond to the element existing in or on the surface of the material being studied. The spectral peaks correspond also to the electron configurations

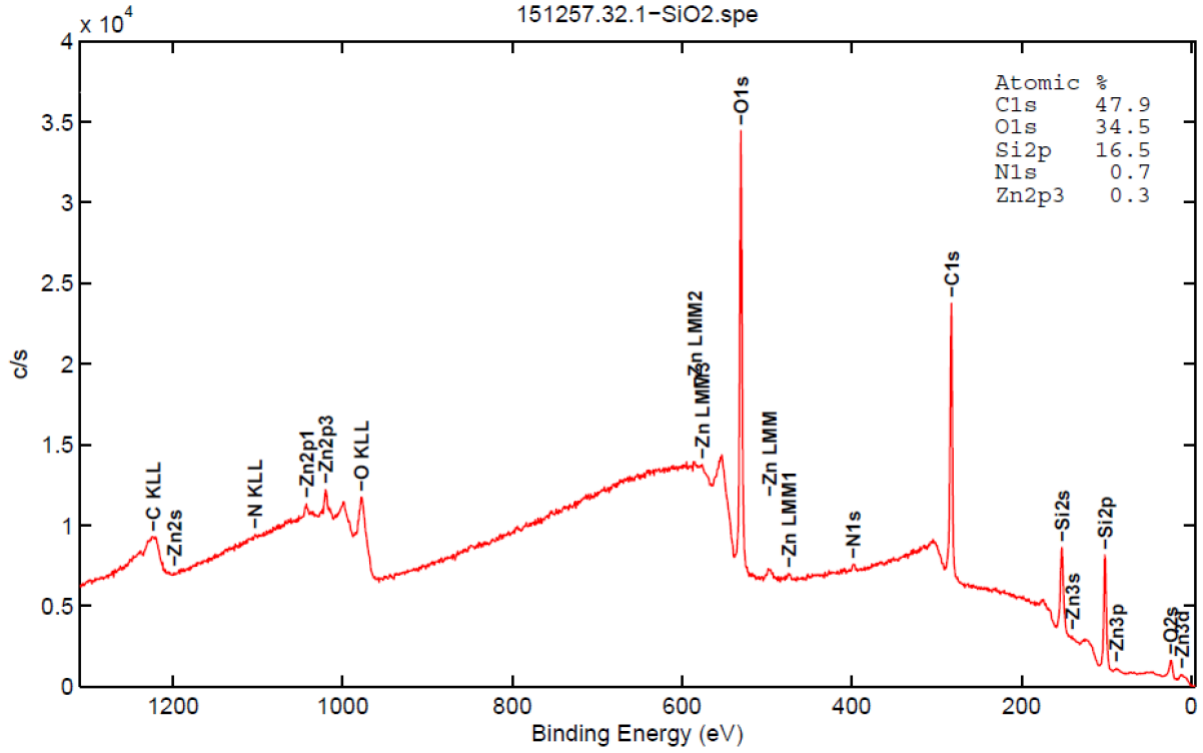

Figure 5.7: Full energy range spectrum of XPS analysis with quantification table for all observed elements with their binding energies, and their atomic percentages.

within atoms (1s, 2s, 2p, 3s, etc.). Each characteristic peak contains the information about the number of detected electrons directly related to the number of elements within the XPS sampling volume (see Figure 5.6).

XPS technique was utilized to identify the present oxidation states of silicon, and detect the amount of elemental silicon present in SiO_2, possibly as nanocrystals, and relate the shifts in core levels to Si concentration (See Fig. 5.8). Another high resolution spectrum of the studied samples shows the energy range of the Si 2p signal [72]. The raw data from the spectrum, marked with the red color, is overall signal for five components of different chemical states. The oxidized form of Si (SiO_x, where x=1-2) appears at higher binding energies around 103.67eV. The so-called metallic form of silicon, which resides below the upper layer of oxidized silicon, exhibits a set of doublet peaks at 100.30 eV (Si $2p_{1/2}$) and 99.69 eV (Si $2p_{3/2}$). The fact that the metallic silicon signal can be seen "through" the top-layer of oxidized Si indicates that the silicon oxide layer is relatively thin (6-8 nm). Attenuation of XPS signals from deeper layers by top-layers is often used in XPS to estimate layer thicknesses and depths [73]. After XPS analysis, it was concluded

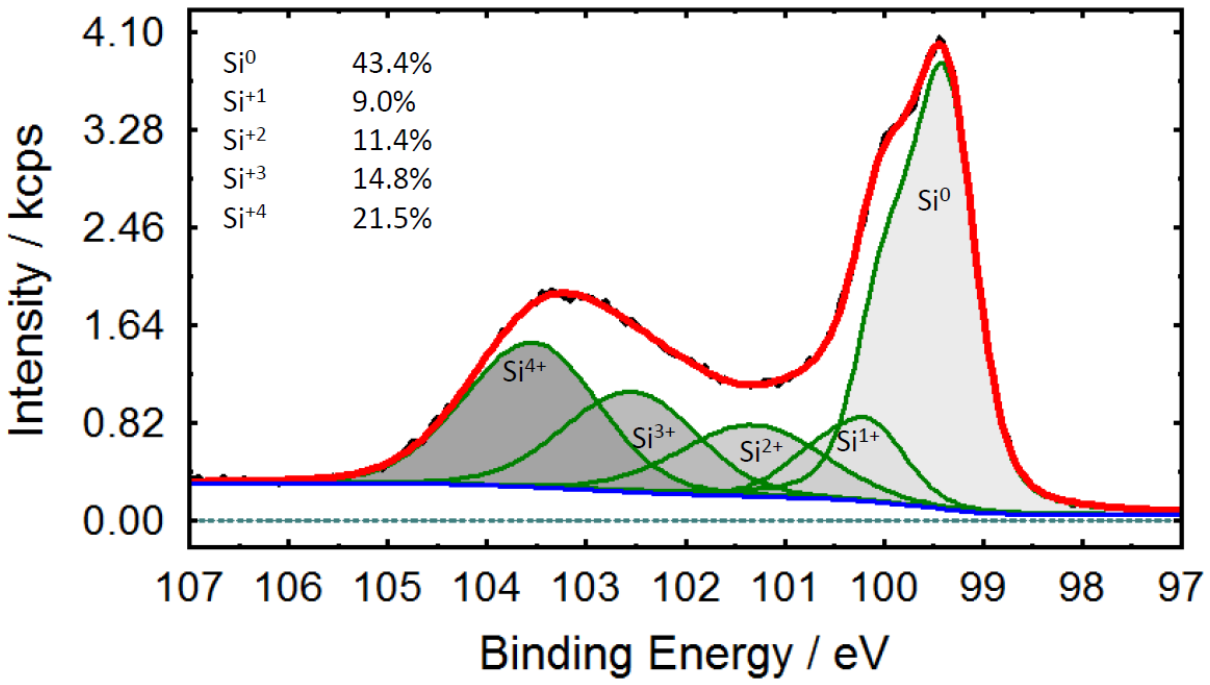

Figure 5.8: High resolution spectrum of the Si 2p peak with atomic percentages for silicon and silicon oxide.

that the fabricated thin-film dielectric oxide layers are stable, chemically correct and without additional contamination by other elements. This method of molecular XPS surface characterization, allowed to assure the high quality of produced thin-film dielectric EIS sensors, and confirmed the applicability of fabricated devices for further research and electrical measurements with target molecules of interest.

5.2 Label-Free Electrical Detection of Cardiac Biomarkers

For the biomolecule detection I used a field-effect capacitive electrolyte insulator semiconductor (EIS) technique capable of yielding a quantitative information about the diffusion potential and doping concentration in semiconducting materials. Such approach is widely used to determine semiconductor parameters and can obtain oxide thickness, oxide charge, mobility and density of interface traps.

Figure 5.9 schematically represents the measurement cell, connected to impedance analyzer. This technique is used to characterize the flat-band voltages and other

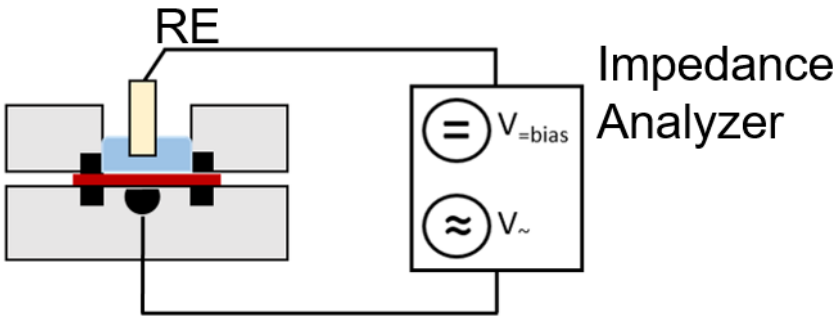

Figure 5.9: Schematically represented measurement cell for thin film dielectric layers.

parameters of fabricated EIS biosensors with thin-film dielectric layers. During the procedure of electrical detection, the DC bias voltage was applied across the EIS structure to set the working point, while making the measurements with an AC signal. Frequencies of the AC used for measurements were in the range from 100Hz to 1MHz. Obtained data are typically represented in the form of the capacity dependence on the applied voltage. Measured capacitance values allow to extract the flat-band voltage, thus providing the information about the properties of molecular layers. To perform the characterization, the EIS-based sensor chip with a thin-film dielectric SiO_2 was placed into the transparent "home-made" measurement cell. The EIS-sensor chip was sealed with the resin O-shaped ring. The voltage was applied to the sensor through the Ag/AgCl reference electrode, and a rear contact pin from the back side (Fig. 5.9). C-V measurements have been performed at a frequency of 1 kHz. All measurements have been performed in a dark closed Faraday cage at the room temperature.

5.2.1 C-reactive protein Electrical Detection

For attachment of C-reactive protein antigen, several steps from immobilization protocol were provided. At the beginning of immobilization, the thin-film dielectric layers were rinsed with solutions of acetone and ethanol followed with drying under a nitrogen stream. Then thin-dielectric oxide films were treated with the chemical solution of NH_4:H_2O_2:H_2O (1:1:10) in order to activate the surface. Then at argon atmosphere, the films were silanized with (3-glycidoxy-propyl)-trimethoxysilane (GPTES) molecules in a heated desiccator at 5 mbar for 1 hour. Finally, the films were covered with CRP-antibodies dissolved in 10mM phosphate buffered saline. Since the distribution of the antibodies can be irregular, some unattached aldehyde

groups can be still be active. Therefore, to prevent any non-specific binding, the aldehyde groups were blocked with Ethanolamine solution for 30 minutes. CRP antigens were then successfully bonded to the immobilized antibodies.

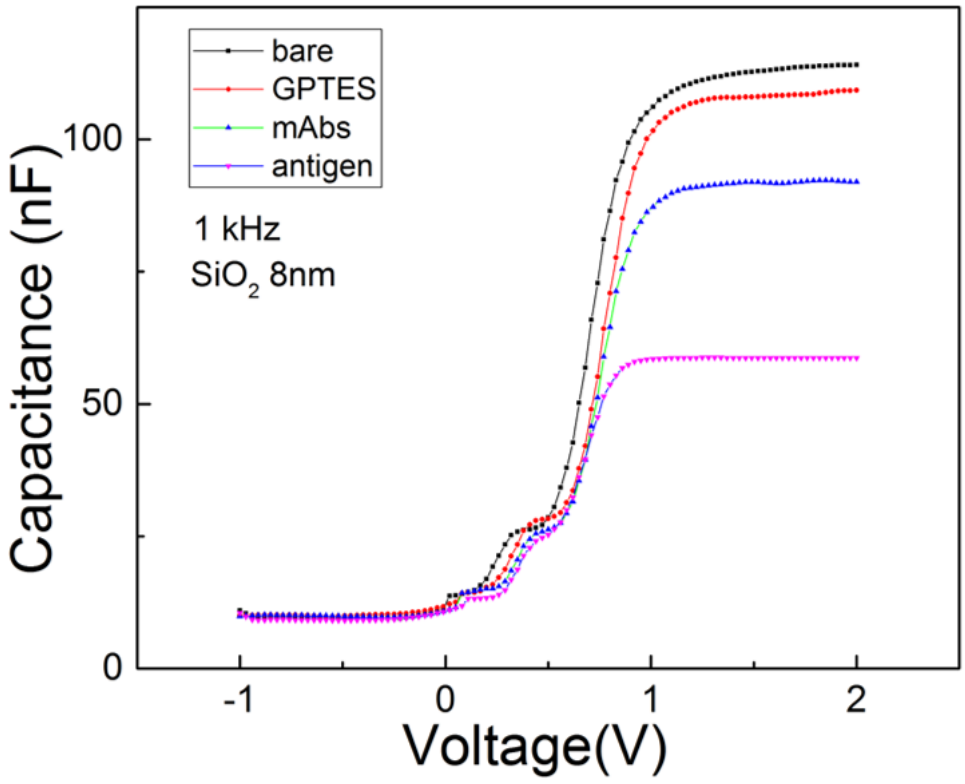

Figure 5.10: Dynamic of the C-V curve shift upon modification of a bare thin film (black) consequently with GPTES silane (red), antibodies-mAbS (green), and finally with antigen (blue).

Electrical sensing measurements were performed by mentioned field-effect capacitive electrolyte-insulator semiconductor measurements. Capacitance-Voltage curves were obtained alongside for each added functional layer during the immobilization procedure. As can be seen from Fig. 5.10, the capacitance value is shifting along with the increased thickness of the measured active sensor layer. After introduced GPTES monolayer the capacitance value has less shift then the attached antibody receptors. CRP-antibodies is the large shaped Y-protein with a molecular height of 12 nm. While the monolayer of silane is only around 1 nm thick, from Fig. 5.10 one can noticed significant difference in the value of the capacitance between CRP-antibodies and CRP-antigens. Such extreme difference in the values may be due to the fact that the maximum permissible concentration of CRP-antigen (4.5 mg/mL) was measured. With such a high concentration, the sensor surface was occupied by

a large amount of antigen. Moreover, used it can be said that the sensor surface was not just occupied, but "filled" with antigens, and blocking BSA solution so much that it was hard to get a signal from the antibody-antigen complex. Therefore the layer of antigens behaved like an extra layer of the thin-film dielectric layer. As a result of this behavior, a significant difference in the capacitance values can be observed, with the small shift of the C-V curves. That concludes that presented field-effect capacitive electrolyte-insulator semiconductor technique is extremely sensitive to even small changes of the active sensor area. The shifts with the depletion region of C-V curves along the voltage axis induced by different surface functional layers and bimolecular sensing also studied.

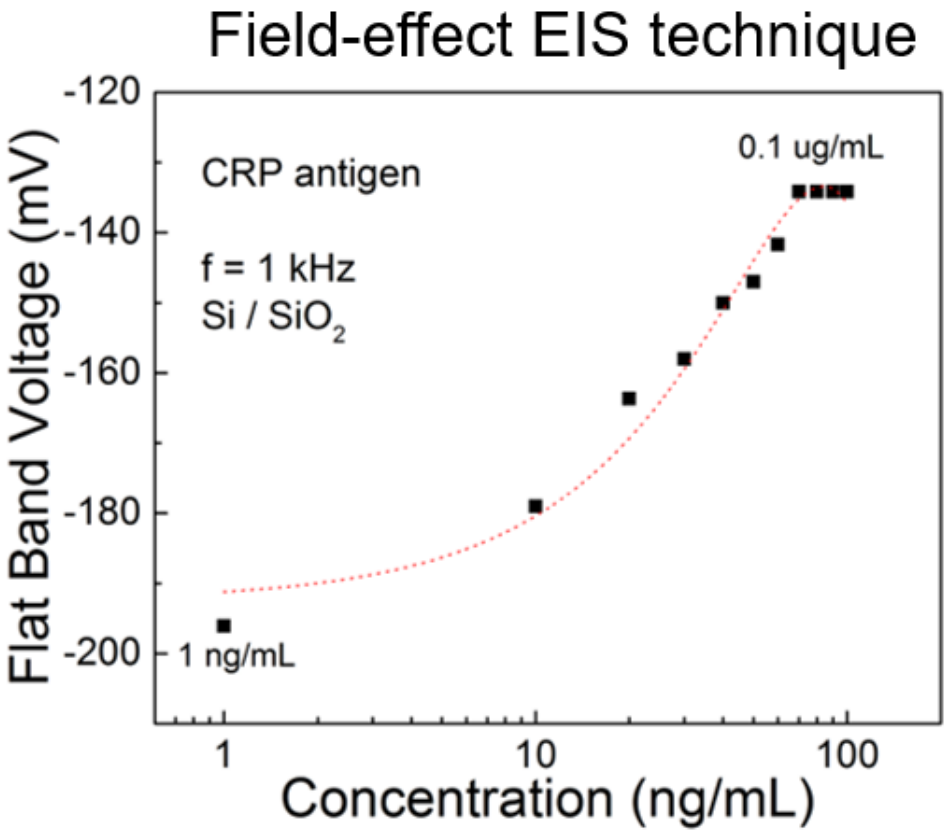

Figure 5.11: Field-effect EIS detection of C-reactive protein in different concentrations.

Concentration range for CRP antigen was varied from 100 ng/mL down to 1 ng/mL in order to test device sensitivity. For each followed concentration of antigen, the C-V graphs were plotted and the flat band voltage was calculated. Resulting flat band voltage values were plotted then as a function of CRP antigen concentrations. The result can be seen in Fig. 5.11. The curve can be divided into two parts:

linear regime and saturation regime. The linear part of flat band voltage values is occurring due to the presence of additional charges near the sensing area of the biosensor. C-reactive protein has a basal isoelectric point around 5.45, and therefore negatively charged at the pH 7.4. consequently, by applying more negative charges to the sensing area we got a response in flat band voltage. As can be seen in Fig. 5.11, at higher CRP-antigen concentrations the linear dependence transforms into saturation mode. At this point of view, can be said that all receptors presented by CRP-antibodies are successfully bonded all introduced antigens, and there are no free receptors to bind more. Since the received signal on the graph depends on the concentration, it is clear that the received signal is identical to the general signal of the antibody-antigen complex. The lowest concentration of antigens which was achieved with functionally immobilized CRP-antibodies is equal to 1 ng/mL. The presented experiment showed that the developed method with functional layers allows to easily and accurately measure biologically active molecules with charges.

5.2.2 Cardiac Troponin I Electrical Detection

Aptamers are unique molecules that enable the enhancement of signal detection from target biomolecules due to their characteristic size which is about twice as short as a length of antibodies [74]. The receptors used in this work were synthesized from DNA and modified with amino-C^6 linker (-NH_2) at the 5' end to attach aptamer specifically on silicon dioxide surface [75].

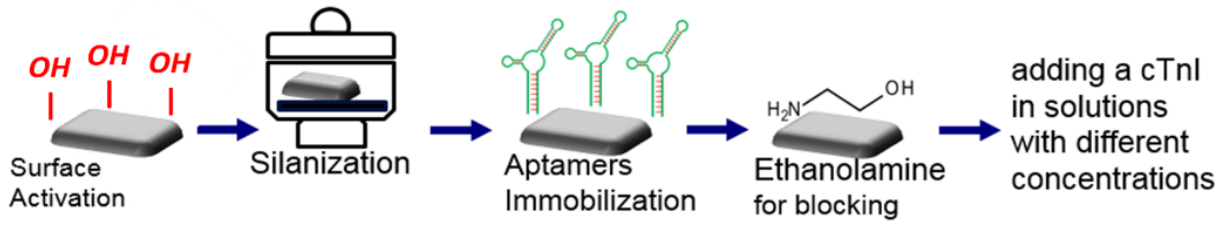

Figure 5.12: Immobilization protocol for aptamer binding from [76].

Firstly, films were hydroxyl activated in a plasma oven (0.8 mbar, 80W, 3 min). The thin-film dielectric layers were then silanized for 1 hour at argon atmosphere with 3-aminopropyl-triethoxysilane (APTES) molecules in a desiccator at 5 mbar. In order to produce a thin silane layer, the dielectric films were then rinsed with 1M Acetic acid. Finally, the films were covered with aptamers dissolved in phosphate-

buffered saline (PBS). To perform the final stage of immobilization, the aptamers were dissolved in 10mM PBS with pH=7.4 to obtain a 100pM solution. The immobilization was performed at T=37°C for 40 minutes. Following the immobilization, ethanolamine was used to prevent non-specific binding. As a result of the protocol, the human cardiac Troponin I antigen molecules are specifically bound to the aptamers.

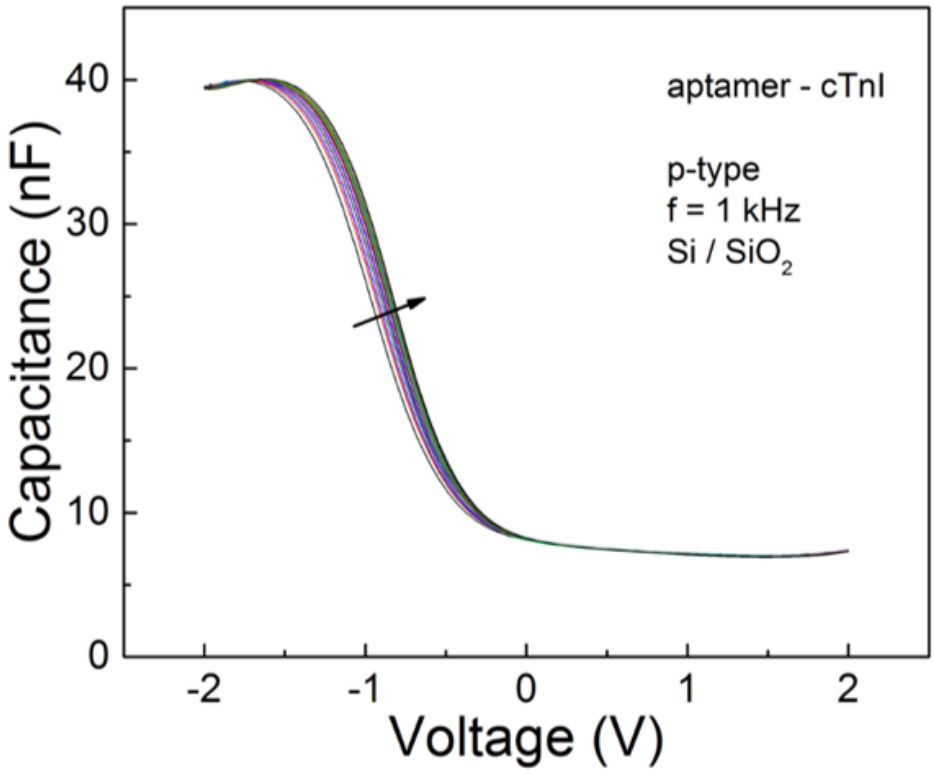

Figure 5.13: Whole voltage range of the Capacitance-voltage dependencies, measured for different antigen concentrations with the step equal to 20 pg/μL from [76].

The successful binding and detection of cardiac Troponin were verified using electrical measurements. For field-effect capacitive electrolyte-insulator-semiconductor (EIS) measurements, was used a solution of antigen dissolved in phosphate-buffered saline (10 mM, pH=7.4) in a concentration range from 10 pg/μL to 1 ng/μL. The optimal frequency for studies in the voltage range of -2V to +2V and electrical characterizations were selected to be of 1 kHz. The isoelectric point value of human cardiac Troponin antigen is equal to 9.6, therefore the molecule can be presented as a dipole moment with a negative charge. A negative dipole moment changes the value of a flat band voltage and results in the shift of capacitance-voltage curves

(Figure 5.13). The value of capacitance depends on the thickness of the functional layers and the composition of the layer structure. As shown in Figure 5.14, a zoomed image of capacitance-voltage curves demonstrates a clear shift due to the reaction to the introduced charge of the target molecule. The key aspect in these types of dependence is the flat band voltage, which is affected by oxide charges [77].

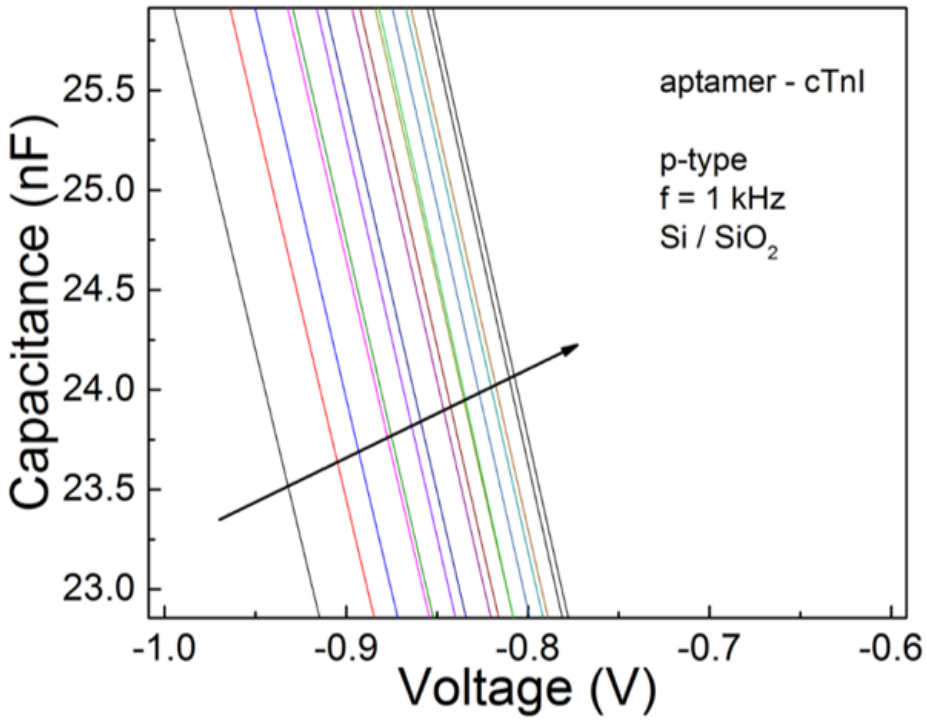

Figure 5.14: Enlarged part of the Capacitance-voltage dependencies, measured for different antigen concentrations with the step equal to 20 pg from [76].

In the cases involving a p-type sensor, all flat band voltage values are generally negative, as can be seen in Fig. 5.14. For each concentration of Troponin antigen, flat band voltage values were calculated and extracted, and their concentration dependence was plotted. The aptamer-antigen binding system can be characterized using the Langmuir isotherm equation. This equation describes a typical saturable binding in a variety of chemical, physical, and biochemical situations [78]. It was considered that under certain conditions, the concentration of the aptamer receptor (R) is far less than that of the Troponin antigen (L). Hence, the formation of the binary complex does not significantly diminish the concentration of the antigen. Therefore the approximation can be made that the free antigen concentration is

about the same as the total antigen concentration added, which thus follows:

$$[RL] = \frac{[R][L]}{K_D + [L]} = \frac{[R]}{1 + \frac{K_D}{[L]}} \tag{5.8}$$

$$[RL]_{min} = 1pM \tag{5.9}$$

Fraction occupancy of the receptor is often represented by the symbol B (for bound receptor) and can be calculated using the following formula:

$$B = \frac{1}{1 + \frac{K_D}{[L]}} \tag{5.10}$$

This equation describes the binding in a variety of chemical, physical, and biochemical situations. It is often used to determine the cooperativeness degree of binding ligand to the macromolecule or enzyme. This Langmuir isotherm equation is useful in normalizing data and can be plotted as a function of antigen concentration (see Figure 5.15).

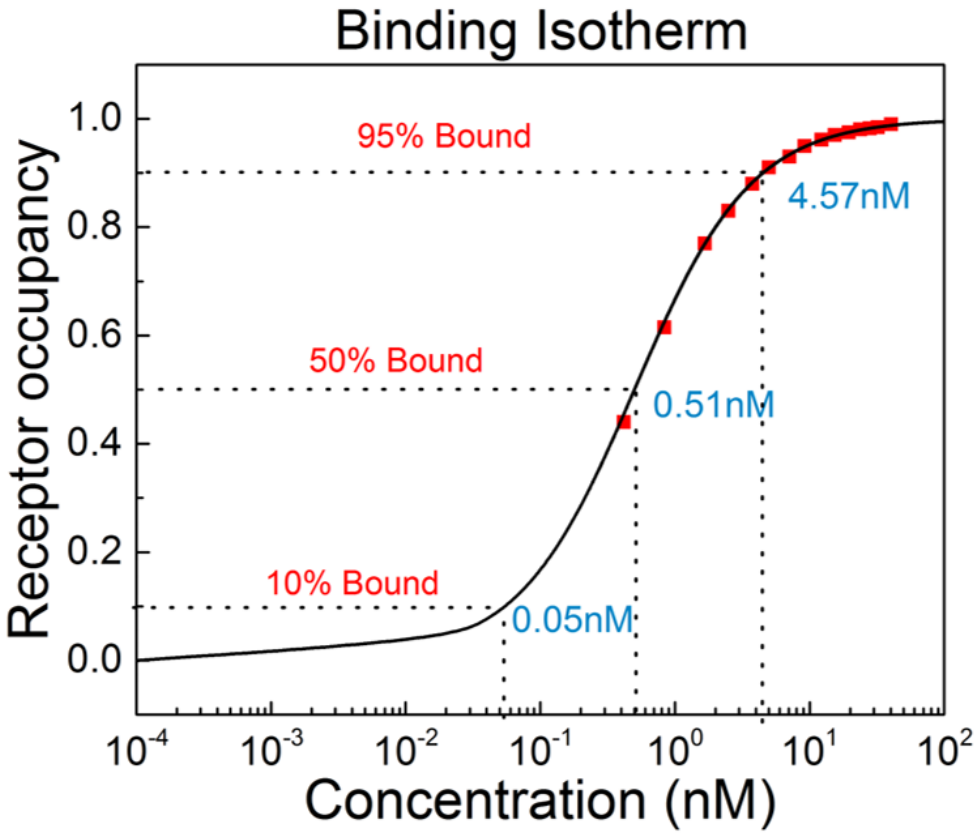

Figure 5.15: Calculated binding isotherm for aptamer-troponin complex from [76].

Based on the calculations of equations 5.8 and 5.9, it can be concluded that the fabricated sensor allows the detection of different concentrations of the aptamer-Troponin complex down to a value of 1 pM. The results demonstrate high sensitivity and are in good agreement with the data presented for human cardiac Troponin I studies on a gold electrode [79]. At the same time, I obtained a high-selectivity detection principle of cTnI using aptamer immobilized on the SiO_2/Si substrate, which opens up possibilities of using the detection protocol for silicon nanowire covered with a SiO_2 layer in field-effect transistor (FET) structures [80]. FET-based biosensors enable active amplification and increased sensitivity to very small changes in Troponin concentration. This may allow for the label-free monitoring of cardiac troponin in real time and enable other cardiac markers to apply medical treatment in time for Acute Myocardial Infarction (AMI) - one of the world‘s leading diseases according to causes of death statistics. The results allow the stable and reproducible detection of cTnI on a SiO_2 layer, introduced on many similar materials for point-of-care portable biosensor applications.

To conclude this part of the work, the thin films of silicon oxide dielectric layers on silicon were fabricated and used to study the detection of a molecule of human Troponin antigen (cTnI), which is a cardiac biomarker for the early diagnosis of AMI. The aptamer immobilization protocol for detection of the cTnI biomolecules on silicon substrate covered with a SiO_2 layer was successfully introduced. Charged troponin molecules were found to influence the shift of the capacitance-voltage curves of the EIS sensor. The results demonstrate that the thin-film dielectric layers enable high sensitivity for the detection of molecules, such as a cardiac Troponin down to a value of 1 pM. The results are important for future investigations into cardiac biomarkers on thin-film dielectric layers of nanowire field-effect transistor biosensors, which will be described in the next section.

Chapter 6

Field Effect Transistor (FET) Cardiac Biosensors

6.1 Silicon Nanowire FETs Biosensors for Cardiac Biomarkers

Biosensors based on Si NW FETs (see Fig. 6.1) have recently received considerable attention as reliable and robust electronic devices for sensing of various biological molecules due to the unique and tunable electrical properties of silicon nanowires [81]. The high surface-to-volume ratio of nanowires makes them very sensitive to charged molecules [82–84].

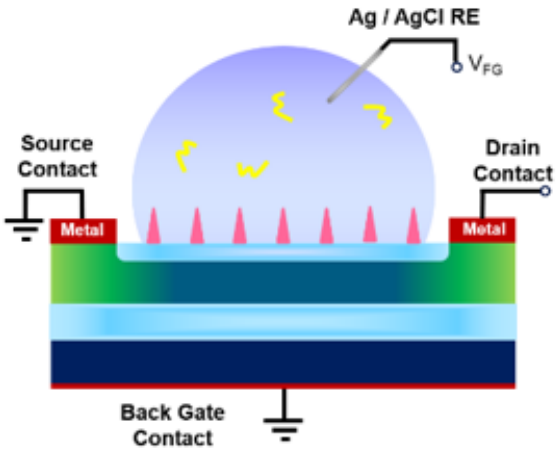

Figure 6.1: Schematic representation of the liquid-gated Si NW FET.

The mechanism of sensing for these types of sensors is commonly based on monitoring of changes in current or conductance of the FETs upon attachment of target

molecules on nanowire surface [85] . Being charged molecules, biomolecules induce a gating field effect, which leads to depletion or accumulation of carriers in the channel resulting in conductance changes that can be measured and correlated with the concentration of target biomolecules in the solution.

6.1.1 Device Fabrication and Characterization

Si NW FETs were fabricated using CMOS-compatible fabrication technology, making the process cost-efficient, and yielding a low device-to-device variation. Moreover these devices can be scaled down to the size of the analyte which enables a detection even of single molecules [86].

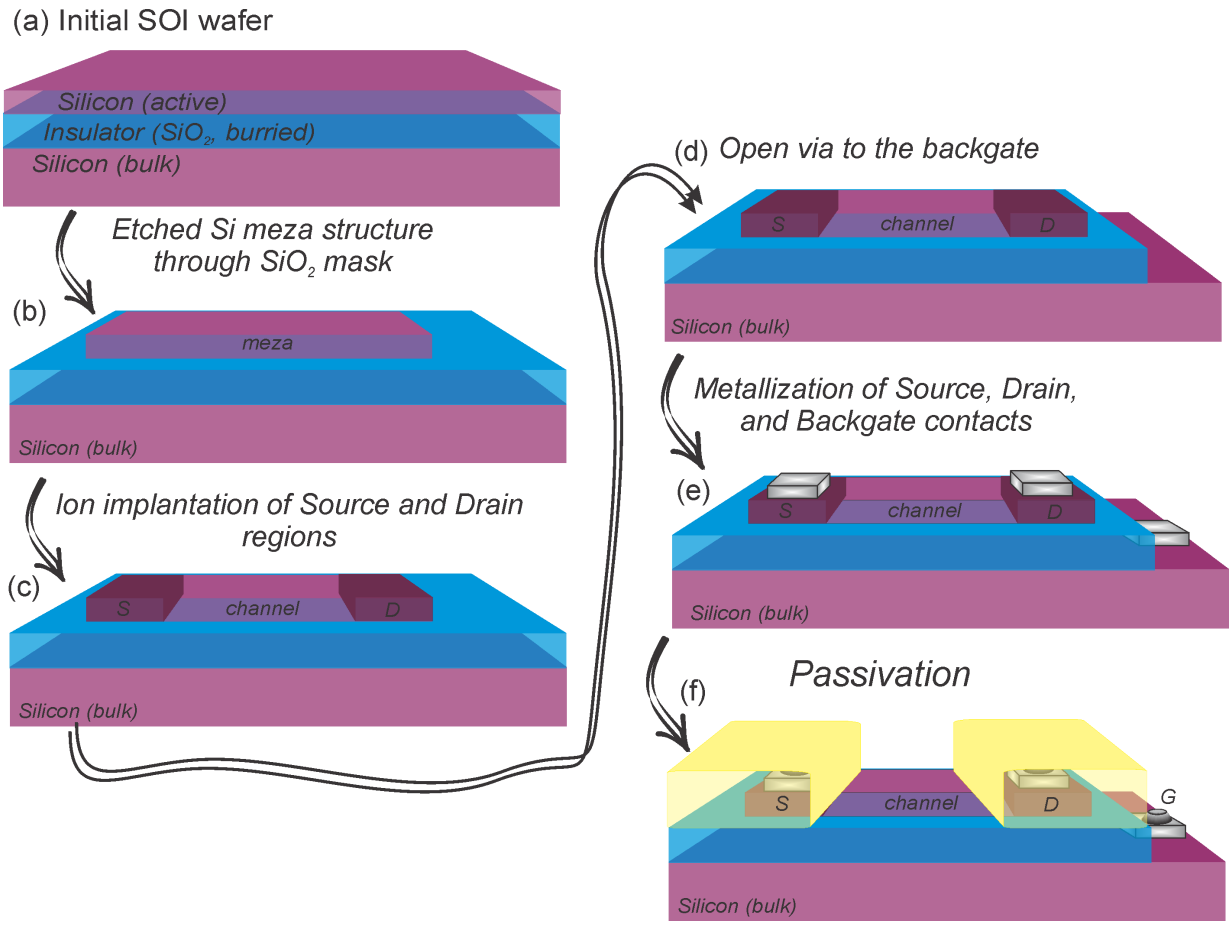

Figure 6.2: Schematic representation of the main steps of fabrication routine of the Si FETs.

The silicon field effect transistors were fabricated on the basis of 4-inch silicon-on-insulator (SOI) wafers (see Fig. 6.2a). At first, a silicon dioxide hard mask was created by dry thermal oxidation (1000°C, 30 min) of the active silicon layer. As a

result, the active silicon layer was thinned down to the required thickness. At the same time the grown silicon dioxide layer will be used for further processes. The hard mask was patterned by anisotropic reactive ion etching (RIE) or wet chemical etching in order to form the meza structures of transistors (see Fig. 6.2(a)). In case of wet chemical etching the 1% HF solution was used. In the case of RIE, the CHF_3/Ar plasma process was used. The main advantages of the latter method are the higher selectivity and highly anisotropic etching profile. The etch rate for the wet chemical process is approximately 6-7 nm/minute, while for RIE it is usually controlled by a laser or calibrated beforehand (approx. 30nm/min). For the etching of active silicon layer around the shaped hard mask, 5% TMAH water solution was used. This kind of silicon etching has high selectivity to the material and yield almost atomically flat surface in comparison to RIE [87]. At a temperature of 90°C, conventional etch rate in 5% TMAH is 1.4 μm/min for <100> plane. Several steps of photo-lithography using AZ5214E photo-resist were performed in combination with electron-beam lithography to pattern the nanowires and nanoribbons. Each lithography was followed by the RIE or wet chemical etching (5% TMAH). As result, the nanochannels/nanoribbons were formed (Figure 6.2(b)). Next, ion implantation of the drain and source regions (Figure 6.2(c)) by boron (6 keV, 10^{15} cm^{-2}) or arsenic (8 keV, 10^{14} cm^{-2}) was carried out in order to get highly doped p- or n-type respectively. Wafers were then annealed in order to activate the dopant: 5 s at 1000°C for boron implantation and 30 s at 950°C for arsenic implantation. Further, a thin layer of silicon dioxide was grown by dry thermal oxidation. Etching of the back gate opening was performed (Figure 6.2(d)), in order to have a possibility to investigate transistor properties employing the back gate with good Ohmic contact.

Metalization of Si FET (Figure 6.2(e)) was followed in two steps. First, metal contact deposition of aluminum with the annealing in the forming gas atmosphere (10 min, 450°C) to get a good Ohmic contact. And second, additional metalization (typically Ti/Au), as a preparation for the wire bonding or flip-chip process. Two last steps, passivation (Figure 6.2(f)) and dicing, were carried out afterwards. For passivation, HD-8820, a photostructurable polyimide-based photoresist was used. The resist, once baked at 350°C results in a perfect, pinhole-free passivation layer of approximately 3μm in thickness. For the dicing, it is very important to apply a protective layer of a photo-resist on the wafer in advance.

The conductance between the source and drain is modulated by the voltage at

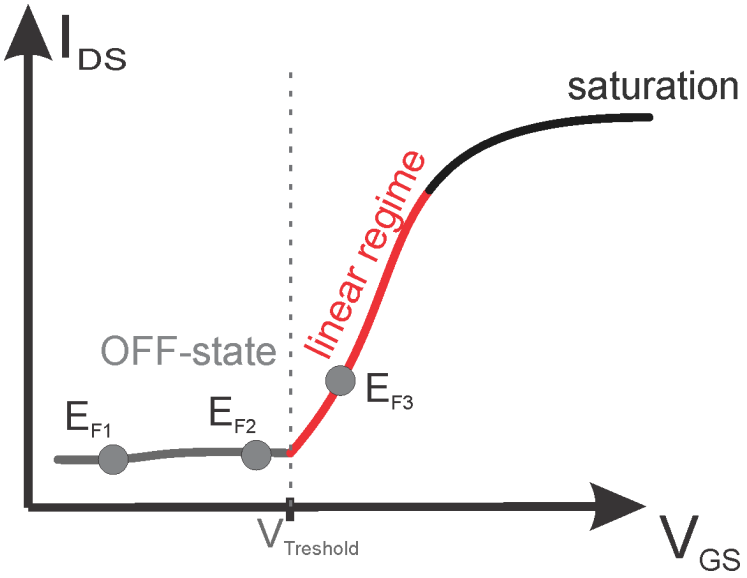

Figure 6.3: A representative I-V curve of a standart silicon based FET.

the gate terminal. In MOSFETs, the metal or polysilicon gate is in direct contact with the dielectric over the channel, but in the case of liquid-gated FET, the gate dielectric is directly exposed to the solution. A gate voltage (V_{GS}) is applied using an Ag/AgCl or Au reference electrode to set the operating point of the device. The conductance of the channel is measured by applying a drain to source voltage (V_{DS}). A typical I-V curve of a silicon NW FT is shown in Figure 6.3. Variations of the surface potential, induced by changes at the dielectric-solution interface on the current through the channel and act as a variation of the gate voltage. However, there are several important challenges, such as the stability and reproducibility of the operation of such sensors in a liquid environment due to changes of the thin gate dielectric properties when exposed to an electrolyte for a long time. Liquid-gated Si NW FETs can be used to detect changes of the pH value of the solution [88]. Using nanowire sensors to measure solutions of known pH can provide a good metric for characterization of the sensor device sensitivity to the surface charge. However, the intrinsic sensitivity of the dielectric surface cannot exceed sensitivity 59.2 mV/pH at 25°C as dictated by the Nernst Limit [89] due to the presence of surface states at the silicon/insulator interface, ionic screening in the solution, mobile oxide charge and the intrinsic buffer capacity of the dielectric.

Furthermore, in order to detect charged analyte biomolecules, the nanowire surface has to be modified and functionalized with specific receptor molecules, which provide selectivity to the analyte. Nowadays, the biomolecular detection methods

can be divided into two general categories [90]:

- label technique;
- label-free detection technique.

The label-based methods can detect biomolecules at relatively low concentrations, however, require expensive and time-consuming pre- and post-processing of the samples under study. All of these requirements make them not suitable for real-time detection. Meanwhile, the label-free detection approach utilize biophysical properties of molecules such as molecular weight, refractive index or molecular charge to monitor molecular presence or activity. Changes of the charge at the sensor surface associated with binding and/or dissociation of analyte molecules allow to use Si NW FET device for label-free and real-time detection [91–94].

6.1.2 Biomolecular Electrical Detection with Si-FETs

Experimentally, the current-voltage curves of fabricated Silicon Nanowire FETs are measured using a Keithley 2602A - two channel source-measure unit. The nanowire structures, surrounded by the gate oxide are exposed to an electrolyte solution, in our case 10mM phosphate-buffered saline (PBS) with pH = 7.4 solution. An Ag/AgCl reference electrode was used to apply the gate potential, V_{GS}, while the drain-source bias,V_{DS}, was applied to the highly doped regions of the implanted field-effect transistors. The drain-source bias was kept constant at - 0.1V for all sensing measurements in order to provide a linear working regime of the transistor structures (see Fig. 6.3). The measurements were performed at the room temperature inside of the electrically shielded cage. Nanowire FET devices, controlled by liquid-gate voltage show reproducible transistor I-V characteristics without leakage current.

The response of the sensor is mainly determined by the sensor/electrolyte interface, since the surface charge on the gate insulator is also screened by the charges of counter ions in the medium. However, when the biomolecule binds to the receptors anchored on the surface of the FET channel, the intrinsic charges of the molecule generate the electrical field disturbing the electrostatic equilibrium (see Figure 6.10 for schematic). Consequently, the field gating effect induced by such charges causes the accumulation or depletion of carriers in the channel depending on the charge carriers in the semi-conductive channel. In this respect, the modulation of the channel conductance, which is proportional to the density of the carriers in the channel,

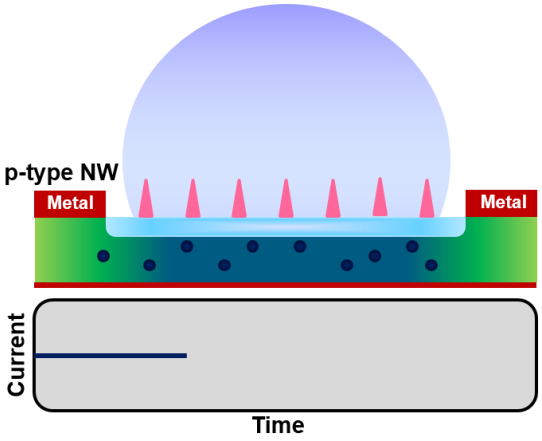

Figure 6.4: A ground control recording. Current-time recording is stable, since there is no specific reaction happening between the oxide surface and target biomolecules in the elctrolyte.

reflects the changes in the current-voltage characteristics caused by binding of the biomolecule. If there are no specifically targeted biomolecules in the electrolyte, there is no current change over time (no reaction, see Figure 6.4).

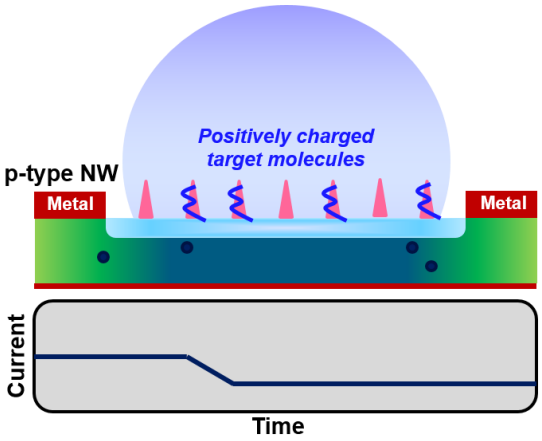

Figure 6.5: Positively charged biomolecules on silicon oxide nanowires.

When charged macromolecule is tethered to the gate surface through the receptor molecule, each of them is surrounded by counter ions with charge distribution defined by the ionic strength of the solution. In this case, the condensation of the biomolecular charge on the charge of the receptor molecule depends on a Debye length of the buffer [95]. If the Debye length is greater than the intermolecular distance between ligand and receptor molecules, the molecules become not entirely electrically screened by counter-ions and consequently the intrinsic charges of biomolecule are free to move within biomolecule-receptor pair due to sharing of

electrons. In this respect, the electrical field that affects the surface potential is generated by intrinsic charges inside the biomolecule-receptor system.

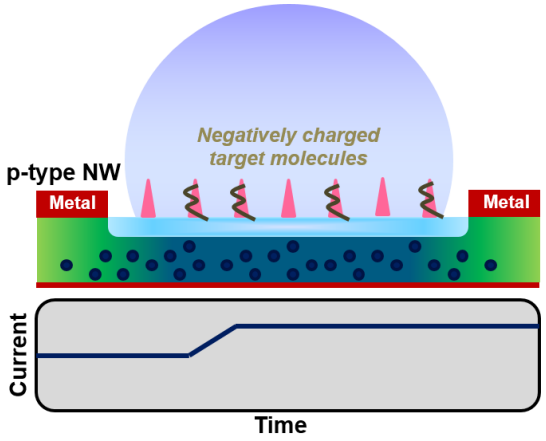

Figure 6.6: Negatively charged biomolecules on silicon oxide nanowires.

The current-time response to the reaction will depend on the charge of the target molecules and affects by the concentration of introduced charges (see Fig. 6.5 and Fig. 6.6 for both cases).

6.1.2.1 C-Reactive Protein detection with Si-FETs

It is known that the C-reactive protein (CRP) molecule is a primary inflammation marker that is recently emerged in medical practices for monitoring the state of inflammations [96, 97]. The concentration of these molecules increases rapidly in response to inflammation and tissue damage.

Thus, monitoring of CRP levels in the blood allows for a prediction of the risk of different diseases and helps to track the development of these diseases in order to apply appropriate treatment [98]. Single Si NW FETs with a width of 250 nm and length of 4 μm were used for the measurements. The response of the sensors to the concentration of target CRP antigen molecules was measured by monitoring the concentration-dependent shift of transfer characteristics (drain current vs. liquid gate voltage). The overview of the protocol of antibody modifications is shown in Figure 6.7, and includes the following steps:

- **Oxygen plasma**;
- **Silanization**;

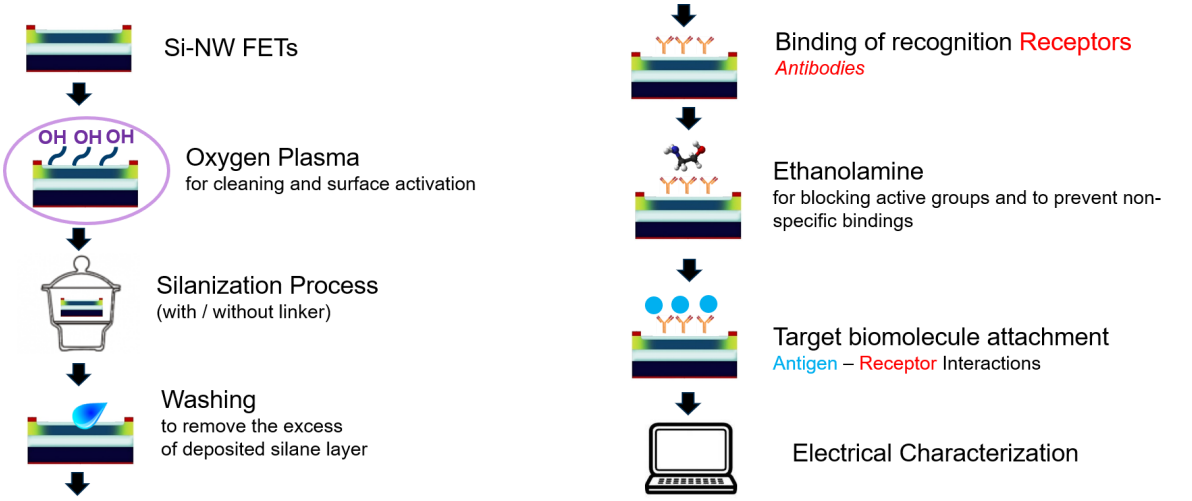

Figure 6.7: Immobilization protocol with functional layers for double gated SiNW-FET for specific biomolecules attachment.

- **Washing** to remove excess of silane;
- Binding of **Antibodies**;
- Blocking the uncovered silane groups with **Ethanolamine** to prevent non-specific binding;
- Measure electrically while or before/after addition of **target antigens**.

The details of each step are given in the appendix D to the thesis. Reference measurements are performed in pure 10 mM PBS at pH = 7.4 solutions and then in different concentrations of CRP antigen molecules in the range from 10 pg/ml to 10 ng/ml. After each concentration, the transfer curve was measured. The results of the measurements are shown in Figure 6.8. With increasing of the antigen concentration, transfer curves shift to the direction of higher currents. This indicates that the CRP concentration increase causes the negative charge increase on the gate oxide surface due to antigen-antibody bindings. The negative introduced charge is in good agreement with literature data concerning the charge state of CRP molecules. The biosensor calibration curve is extracted from the I_D - V_{LG} data and re-plotted in terms of sensitivity $S = |I_D - I_{D0}|/I_{D0}$, which shows a normalized biosensor response to changes in the concentration of target molecules (see Figure6.9) [99]. Here I_{D0} is the reference drain current at zero CRP concentration. Fabricated silicon NW FET biosensors show almost linear response in a semi-logarithmic scale in the

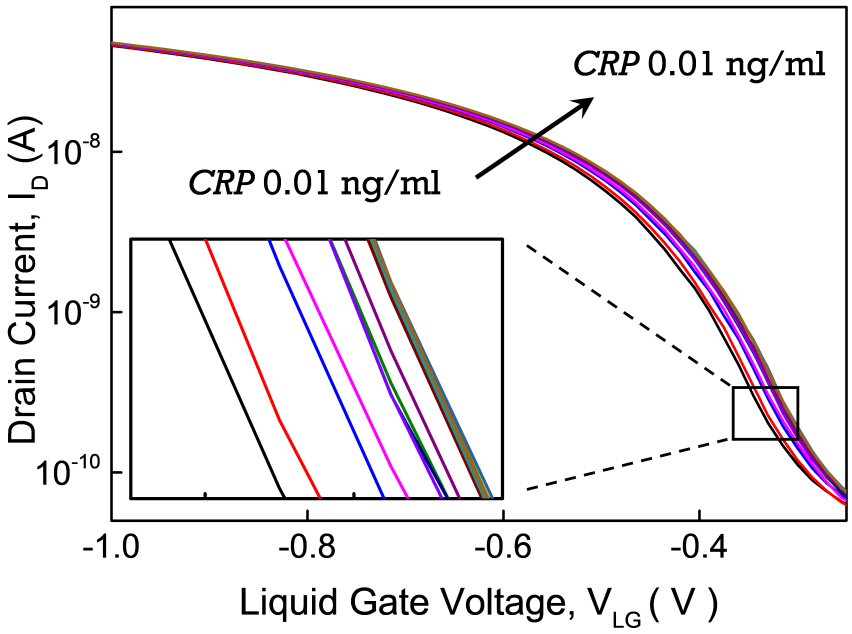

Figure 6.8: Different concentrations of CRP antigen molecules in the range from 10 pg/ml to 10 ng/ml.

concentration range from 50 pg/ml to 5 ng/ml. This concentration range of CRP detection can be described by the following equation:

$$S = 0.23 \times \log_{10}[C] + 0.63 \tag{6.1}$$

Starting from concentrations above 5 ng/ml, no further shift of transfer curves was observed with an increase of the antigen concentration. At this point, all the anti-CRP antibodies on the gate-oxide surface were bound to antigen molecules, resulting in the formation of saturation region. The lowest determined CRP concentration equals to 10 pg/mL, however using nanowire structures with different widths and lengths the value can be tuned.

6.1.2.2 Cardiac Troponin I reusable detection with Si-FETs

As it was already described in the introductory chapter, troponin is a protein complex that consists of three sub-units (I, C and T) that modulate the calcium-mediated interaction between actin and myosin in skeletal and cardiac muscle tissue [100]. Subunit I is an ideal biomarker for necrosis diagnosis due to highly cardio specificity, fast release time and high elevation level [25].

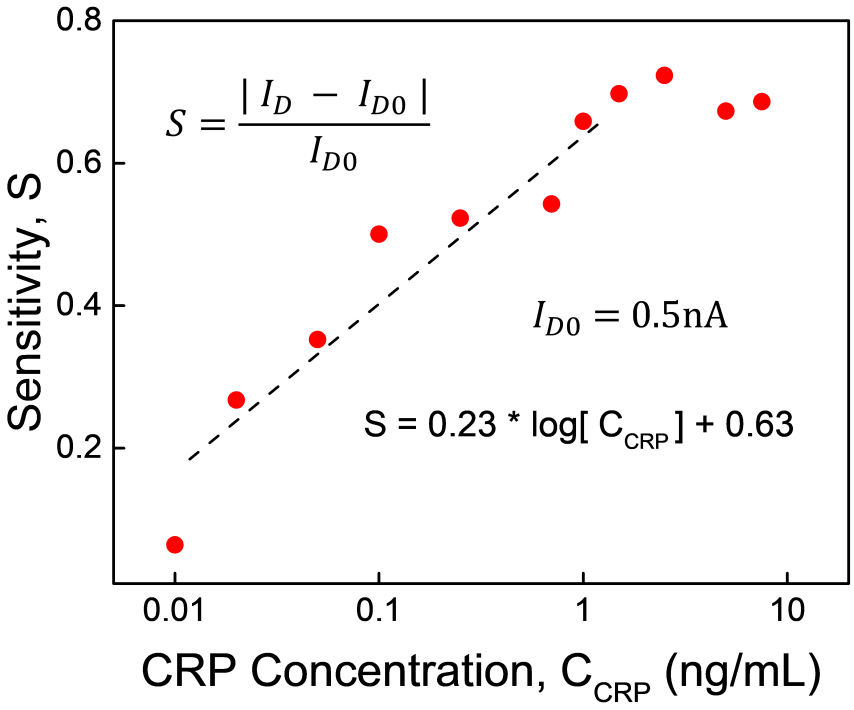

Figure 6.9: Sensitivity of Si NW FET biosensor vs concentration of the target CRP molecules. The concentrations of CRP antigen molecules is varied in the range from 10 pg/ml to 10 ng/ml.

Heart damage progresses are very fast and delayed medical treatment increases the probability of mortality. Therefore, rapid and accurate diagnosis of cardiac cells necrosis and early treatment are critical for increasing the survival rate. That is why fast and accurate determination of cardiac troponin I concentrations is greatly appreciated [101]. Thus, Si NW FETs can be considered as one of the promising candidates for the role of novel diagnostic tool for cardiac troponin I detection [99, 102]. For the detection of such marker, the sensor was rinsed with ethanol to clean the surface and dried under the nitrogen flow. Then the thermal treatment was performed in order to dehydrate and activate the surface of nanowires.

Next, 3-aminopropyltriethoxysilane (APTES) layer was introduced to the nanowires by low-pressure molecular layer deposition during 1 hour at room temperature. After the APTES treatment, the device was immersed in glutaraldehyde solution to introduce aldehyde-terminated surface. Then the highly specific antibodies were covalently linked to the nanowire surface. Finally, to prevent non-specific binding of proteins, the remaining unreacted aldehyde terminal surface groups and unspecific binding sites were blocked using ethanolamine. The Si NW chips were functional-

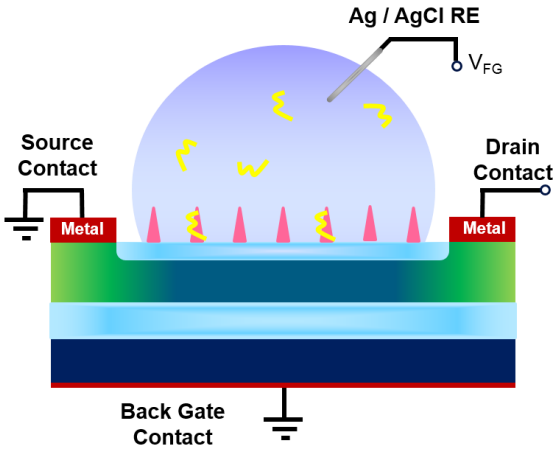

Figure 6.10: Schematic of a double gated SiNW-FET with functionalized top oxide layer and specific biomolecules present in the electrolyte.

ized with cardiac TnI antibodies as described above and used for sensing experiment to detect a various concentration of cardiac TnI antigens in 10 mM buffer solution with pH 7.4. The buffer ionic concentration was adjusted to abate the screening effect of ions and accordingly to maximize sensor response.

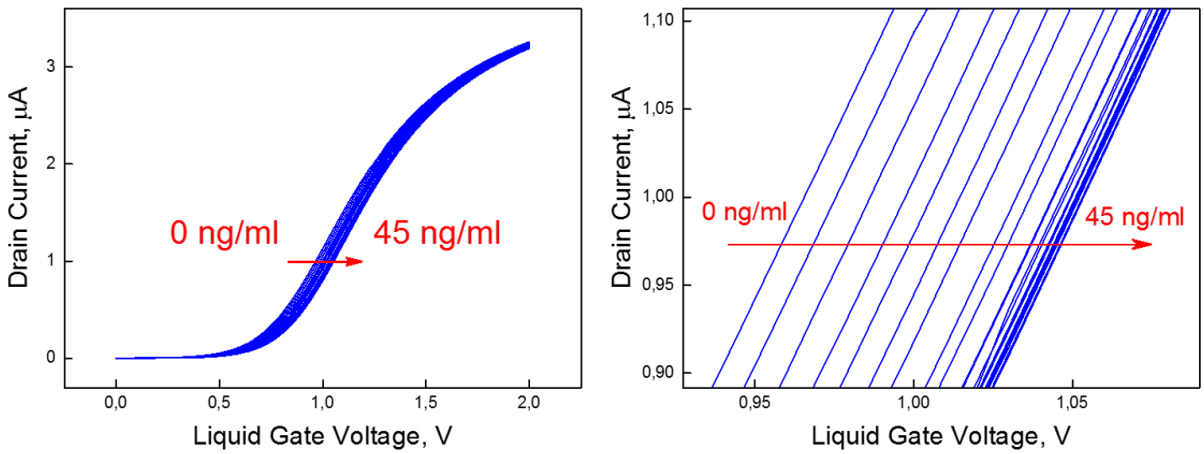

Figure 6.11: Transfer characteristics of the functionalized Si NW FET sensor for various cTnI concentrations in 10 mM PBS solution. Described in [103].

Figure 6.11a represents the sensing results of the Si NW FET device against cTnI antigen concentration in buffer solution. A static drain current versus liquid gate voltage transfer curve measured before injection of cTnI antigen molecules was used as the baseline. After introducing to a buffer of 20 pM cTnI (about 0.5 ng/mL) - a threshold voltage shift in positive voltage direction was observed. The device response, i.e. the transistor transfer curve was measured within a certain time period

to achieve sensor stable output and an equilibrium state after introducing of analyte molecules into a buffer solution. The isoelectric point (pI) of cTnI molecules was around 5.2 meaning that they carry negative charge in physiological solutions with pH 7.4. Therefore, the binding of negatively charged troponin molecules of n-type Si NW FET results in the depletion of carriers due to the gate effect leading to an increase of threshold voltage.

In order to develop the reusable sensor, it is necessary to establish a regeneration solution, which will be non-destructive and not harmful for both sensor surface (gate-dielectric layer, passivation layer) and recognition layer (immobilized antibodies). Moreover, it is necessary that antigen-antibody interaction dissociate completely during the regeneration [104]. Based on these considerations, glycine–HCl buffer was chosen in the present study as the optimal regeneration reagent for renewal of the functionalized surface of the sensors. Here, it is demonstrated that applying of glycine amino acid solution after the detection of cTnI antigen allows the receptor-analyte complex to dissociate, thus restoring the sensor initial state (see Figure 6.12).

The mild regeneration solution contained 10 mM glycine diluted in 1mM PBS solution (see Figure 6.12). The pH was adjusted to pH 4.0 with HCl. In such environment, the glycine molecules (the isoelectric point of 5.97) carry a positive charge. Since the isoelectric point (pI) of cTnI is around 5.2, antigen molecules become also positively charged at pH=4.0. Therefore, the addition of glycine buffer with low pH results in reversing the attractive van der Waals and electrostatic (Coulombic) forces, which hold antigen-antibody complex together, into repulsive forces. In this case unfolding of proteins takes place leading to dissociating effect between antigen and antibody molecules.

Important to note, the glycine-HCl buffer with pH 4.0 does not cause irreversible damage neither to the biosensor surface chemistry nor biosensors itself and assists the decreasing of the bonding strength, maintaining the natural activity of the immobilized antibodies. It should be also mentioned that utilization of glycine-HCl buffer as the regeneration solution has not yet been reported for detection of cardiac troponin I via liquid gated Si NW FETs. After sensing experiment, the analyte solution was replaced by regeneration buffer and incubated for 10 min at room temperature allowing the cTnI antigen-antibody complex to dissociate. Subsequently, after treatment with low pH glycine buffer, the device was rinsed with DI water and

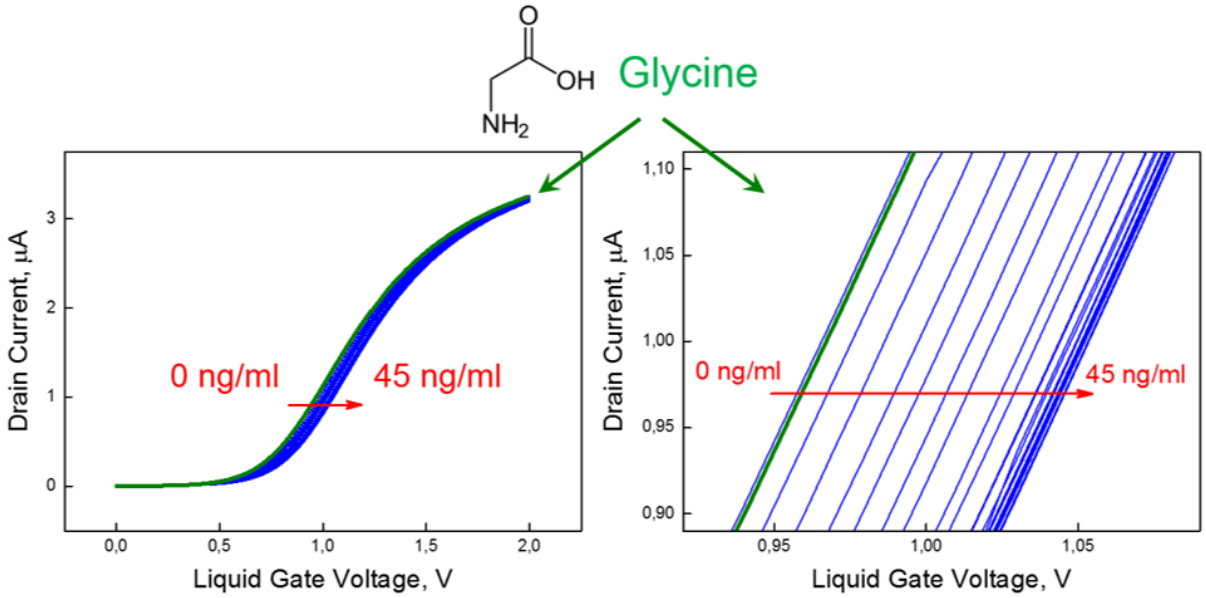

Figure 6.12: Transfer curves before binding of troponin molecules and after applying of glycine regeneration solution. Described in [103].

drain current–liquid gate voltage measurements were taken again under the same conditions in order to make a comparison with the original curves. As it is shown in the Figure 6.12, after applying of regeneration solution, the electrical characteristics of the Si NW FET returned to the initial state, indicating on the successful renewal of the sensor surface and the stability of the device.

6.1.3 Extracellular Recording with Si-FETs

In the previous sections, I described measurements of cardiac biomarkers, which are indicators of cardiac inflammations. In the ideal case, it would be necessary to understand the initial nature of these cardiac biomarkers. In order to understand the relationship between biomarkers and cardiac disorders, it is necessary to look inwards, at the cellular level.

Signal recordings from individual electrically active living cells (e.g. cardiomyocytes or neurons) represent the general approach for understanding biological processes in living systems on different levels, starting from networks of cells down to the single cell level. In particular, the heart is a highly important system to study since it is the engine of the human body which ensures a continuous flow of blood and provides an organism with oxygen and nutrients. Heartbeat fluctuations may be determined by a variety of factors, among which cardiac dysfunction or

cardiac diseases occupy the highest priority for medical treatment and health care applications.

Silicon-based devices, produced using modern complementary metal-oxide-semiconductor (CMOS) – compatible technology possess a variety of advantages due to extensive research over the last decades. The sensitivity enhancement of biosensors based on Si NWs was confirmed for a variety of test biological objects, including proteins, nucleic acids, and viruses. Advanced CMOS technology allows for much denser packaging resulting in higher spatial resolution. It should be emphasized that recent research activity in the interfacing between living cells and nanoscale objects demonstrates better interface properties for such structures with a decreased cleft when compared to large scale planar devices.

The cardiomyocyte HL-1 cell line was stored and received from a frozen state. The cardiomyocytes are thawed under the bench at room temperature and passaged in T25 culture flasks for several days until the moment of full coverage of the surface. The constructed layer of cells shows beating and electrical activity with a frequency of approximately 1-3 Hz. Prior to the seeding of cardiomyocytes, the Si NW chips were cleaned with an absolute ethanol solution to remove any dirt from the surface. Then, the surface of Si NW arrays was covered with a mixture of fibronectin (5 μg/mL) dissolved in gelatin (0.2 μg/mL) for 1 hour at 37 degrees to improve cellular adhesion at silicon dioxide surface. The cardiomyocytes were split after the formation of the confluent layer and placed inside the on-chip reservoir in amounts approximately 150 cells/mm. After cell seeding, the Si NW chips were placed into the incubator at 37°C with the flow of CO_2 gas. Claycomb medium was supplemented with a mixture of 100 U/ml penicillin to 100 μg/ml of streptomycin, fetal bovine serum, 0.1 mM norepinephrine, 2 mM L – glutamine, and was exchanged every day during cell growth and approximately two hours before the electrical measurements.

In order to measure the activity of the confluent cellular layer on top of a chip, a multichannel measurement setup was used. The system allows for I–V characterization to be performed as well as time series recordings in parallel from all 32 transistors on the chip. The setup consists of an amplification cascade which includes a pre-amplifier and a main amplifier. For AC coupled measurements, filters are used to prevent aliasing effects. An amplified signal is then passed to the data acquisition system for the readout and further data processing on the computer.

Operational amplifier together with Si NW array FET on the chip (one FET on a chip we will call a channel) represents the pre – amplifier circuit. The resulting amplification depends on the selection of feedback resistance (FBR) connected to the operational amplifier and the actual transconductance of the FET defined by a selected working point.

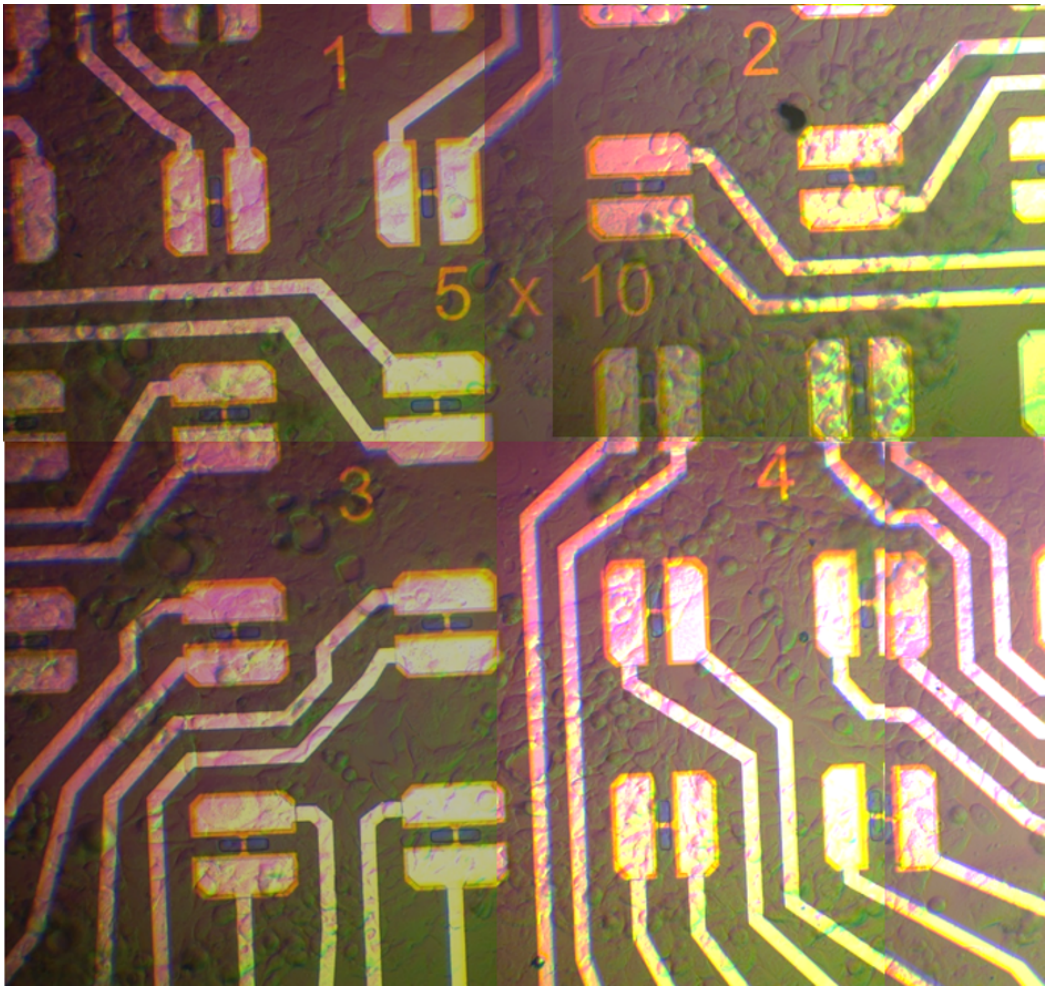

Figure 6.13: Stichep apnorama optical image of *in vitro* cultured cardiomyocyte HL-1 cells on the Si-NW FETs sensors. Spacing between two FETs is 200μm.

The cardiomyocyte cell layer was cultured on top of the chip for 3-4 days (see Figure 6.13 for the differential interference contrast (DIC) microscopy optical image of the HL-1 cell layer grown on top of a Si-NW FET chip). This time is enough for the cells to create a dense confluent layer which already demonstrates beating activity. It is supported by the spontaneous generation of action potentials by the pacemaker cells. Usually, these cells are the strongest and they set the beating rate for the whole monolayer. Since the HL-1 cells form a syncytium, the electrical signals

propagate geometrically along with the tissue. Pacemakers play an important role in providing the stable beating rhythm of the cell community and the synchronization of the cells. Therefore it is important to record not only the electrical activity of cells but also the propagation of the signal across the layer. Our NW sensors satisfy these requirements by performing cell measurements on the chip consisting of Si NW FETs using multichannel measurement setup allowing simultaneous recording of electrical fluctuation from all 32 FETs.

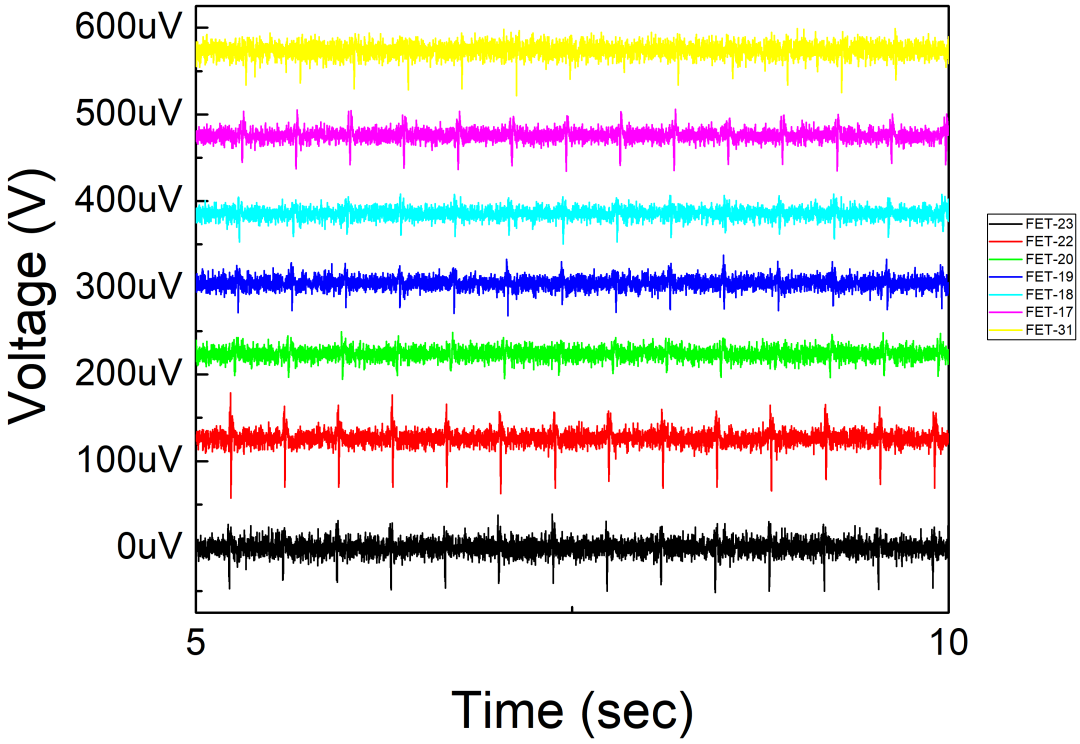

Figure 6.14: Recorded action potential of cardiomyocyte HL-1 cells on the different FETs channels of Si-NW FETs sensors. Each color represents a different transistor. Described in [105].

Prior to time trace series measurements, I – V characterization of transistors on the chip has been performed. The average transconductance curves for both linear and saturation regimes with an average deviation of approximately 12 percents for different FETs are recorded. Next, the recording of time traces at a sampling rate of 1 kHz with the working point set in linear regime with drain-source = -0.1V and liquid gate voltage = -1.58 V (see Figure 6.14) were performed. The maximum transconductance obtained was about 1.88 μS V^{-1} for our Si-FETs. Then time series

measurements in another working point near the saturation regime were performed. The Si-FETs demonstrate higher transconductance values with the maximum equal to 10.57 μS V^{-1} at drain-source voltage = -1.1V and liquid gate voltage = -1.9V. In this working regime clear, APs were recorded with improved SNR compared to the low voltage regime.

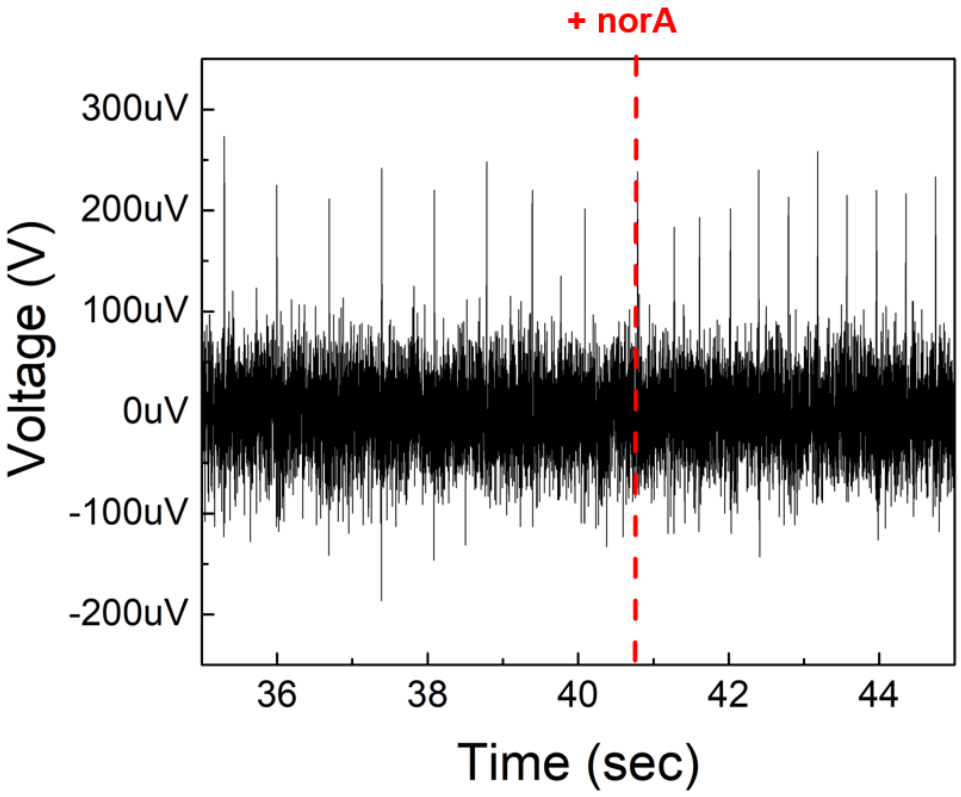

Figure 6.15: Influence of NorA on action potential of cardiomyocyte HL-1 cells on the Si-NW FETs sensors. Described in [105].

Typical action potential timetrace extracted for measurement channel is shown in Figure 6.14, where each color corresponds to a separate channel and are moreover topologically separated from each other. The shape of the signal is in agreement with processes taking place in the cell membrane and correspond to current flows through ion channels. The beating frequency was about 2 – 3 Hz. The action potential propagation across the tissue was also registered using spatially separated FETs (see the delay in APs between different channel in Figure 6.14). In this experiment, a linear chip layout where transistors are fabricated along one line were employed. For this geometry, the time delay of pulses for FET channels was recalculated . Time delays for the seven transistors fit nicely to a linear dependence, demonstrating signal

propagation without distortion. From this data, the propagation speed of AP in the direction along with transistors was extracted. It was calculated to be approximately 13 mm/sec which is similar to values obtained via MEA-based sensors [106, 107].

Finally, in order to prove the influence of pharmacological solutions on APs and to test the biological response to the pharmacological effect on the cultured cells, the Noradrenalin (NorA) was utilized. NorA is known as a drug for heart stimulation and as substance released as a reaction to stress or danger. The beating of the cell depends on the direct stimulation effect of NorA on the pumping of Na+ and K+ cell channels (see Figure 6.15). As it is shown in Fig. 6.15, the addition of NorA to the medium results in almost doubling the beating frequency which is in good agreement with literature [108].

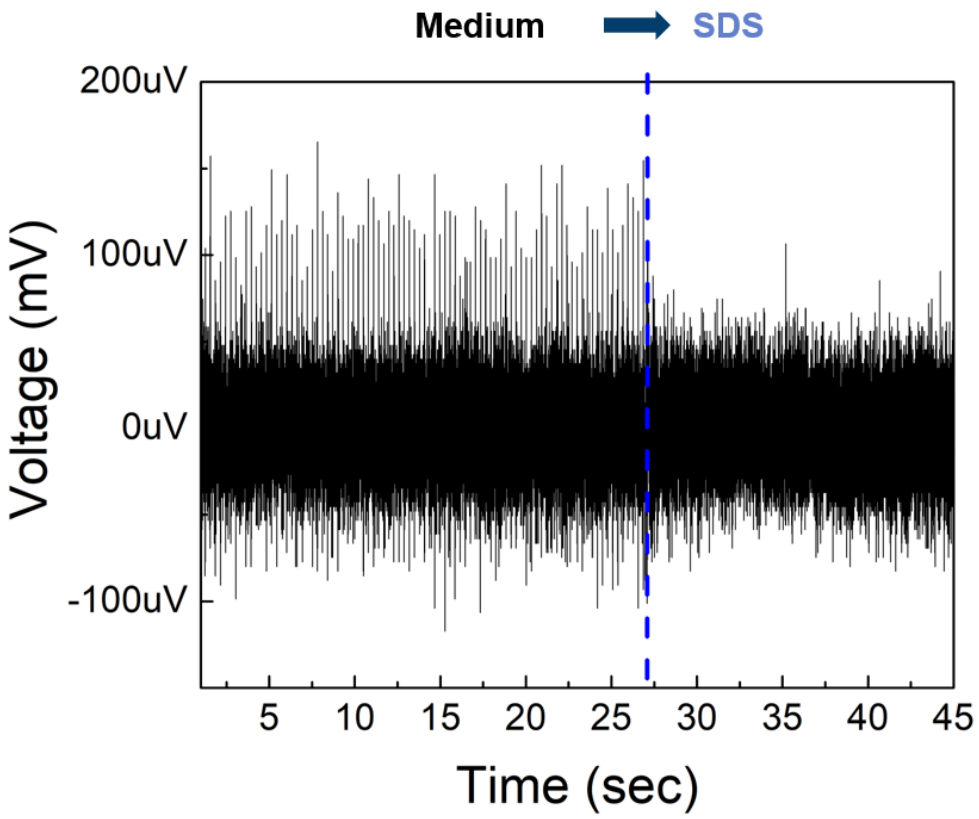

Figure 6.16: Prevented beating activity of cardiomyocyte HL-1 cells by used SDS solution. Described in [105].

Additionally, sodium dodecyl sulfate (SDS) was selected as the surfactant, as it dissolves the cell membrane and may be used to model the critical stage of acute myocardial infarction (AMI). Supplying SDS to the medium perforates the cellular layer, causing the AP activity to vanish, as it is demonstrated in Figure 6.16.

The performed experiments show that Si NW FETs are the perfect candidates for studying cell network behavior at different conditions. Furthermore, they are perfect tools for the studies of cellular responses to a variety of pharmacological influences [109]. Such experimental tools are particularly relevant for the studies of cardiac diseases, including acute myocardial infarction. To summarize, the Si NW FETs were designed and fabricated. The transconductance values reflect the high quality of FET electrical properties. Sensing devices have been used for in vitro electrical activity monitoring of cardiomyocyte cell networks cultured in the reservoir on the chip. High signal to noise ratio value between 3-5 was obtained for fabricated FETs. Reliable recording of AP propagation across the cell layer was shown. Spatially separated FETs allow extracting the position of pacemaker cell, which is important for the studies of HL-1 cellular communication and their responses to external treatments.

6.2 Graphene FET Biosensors for Cardiac Functionality Detection

The research on graphene transistors has emerged with interest an a novel and specialized material. Graphene might be not the best material of choice for a classical logic circuit transistor, since the material is by default conductive and has a bad ratio between "on"- and "off"-current states. However, in the field of bioelectronics, graphene seems to be a promising choice and can be used for flexible applications. Schematic representation of a graphene transistor is shown in Figure 6.17a with associated V_D, V_G, and V_S applied and currents measured through a set of custom made the pre-amplifier system, BioMAS. Figure 6.17b shows a standard ambipolar transfer curve with a Dirac potential and two regions, of hole conduction (left of the Dirac point) and electron conduction (right of the Dirac point). Similarly to the operation of a Si-FET, the usage of GFETs for any biosensor or bioelectronic applications begins with the $I_{DS} - V_{GS}$ characterization, as one shown in Figure 6.17b. The points of maximum slope, also known as points of maximum transconductance are often used as operational points (OPs). Further, when an OP is fixed ($V_{DS} = const,\ V_{GS} = const$), the time series recordings can be performed, i.e. the current flowing through the channel is recorded with a predefined sampling frequency (typically in the range of 1–10kHz). A possible representation of such a

time trace is shown in Figure 6.17b.

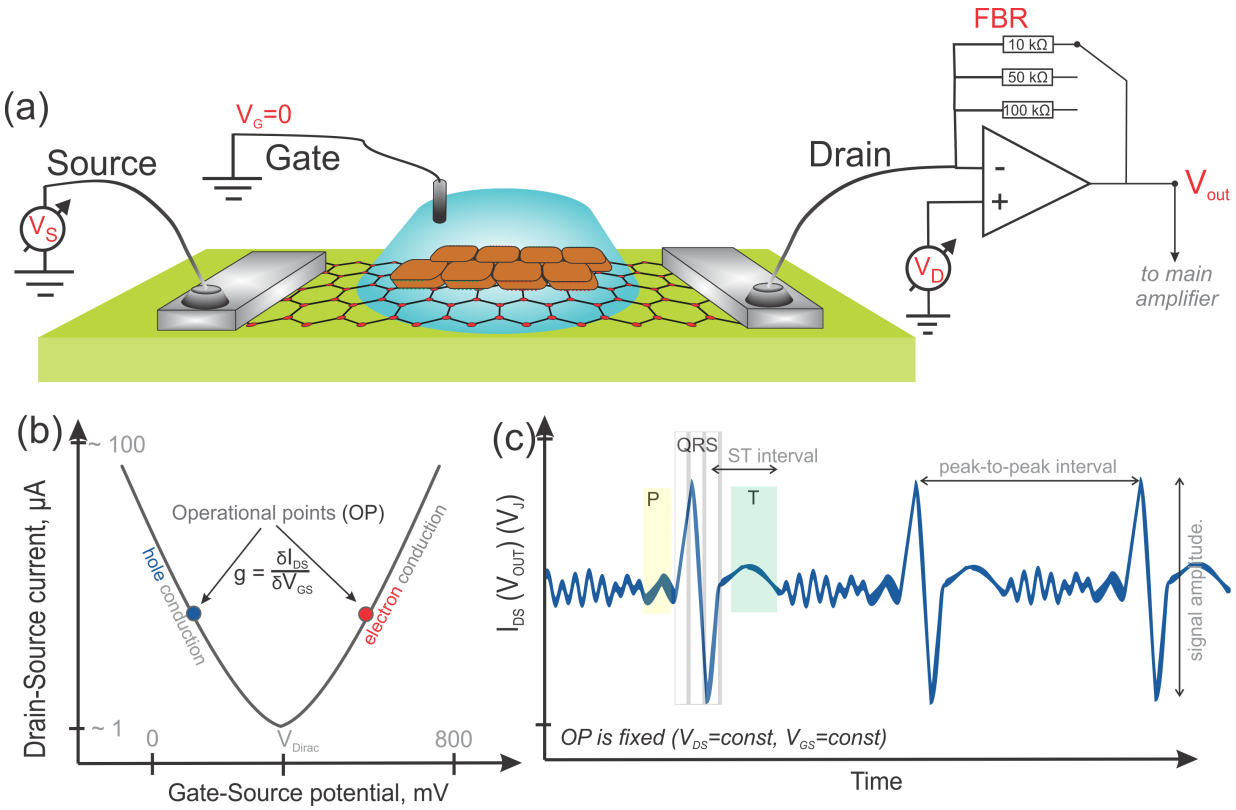

Figure 6.17: Schematics of the signal recording through a GFET. (a) shows a schematics of a GFET with cells grown on top of the graphene. (b) shows a representative for a GFET V-shaped transfer curve. Two points featured on the plot, those are points of maximum transconductance, g_m, one for electron conduction regime and one for hole conduction. In (c) is shown a theoretical timetrace recording when V_{DS} and V_{GS} are fixed ($OP_{electrone}$ or OP_{hole}), and the current flowing through the graphene channel is recorded. The current can be further recalculated into junction membrane potential.

The first graphene field-effect transistor (GFET) application as biosensing element was reported in 2010 by Lieber et al., where they recorded signals from the spontaneously beating embryonic chicken cardiomyocytes [110]. In the next years, research on GFETs has significantly increased [111]. Several advances in biological applications of graphene have been reported recently, for example, Bendali et al. [112] have shown that the CVD grown graphene is a potential substrate for the ganglion cells without any protein supportive coating [112]. A number of groups have shown that graphene-based devices are biocompatible for the recordings of cells cultures, e.g., cardiomyocyte-like cells, human kidney cells, mammalian fibroblast cells [111]. Moreover, the graphene and its surface can be modified with (bio)-active molecules through the chemicals reactions for particular purposes of the application.

Some of them are met to improve the solubility of graphene in the water solutions (relevant for the drug and therapeutic agents research areas), some are used for the modification of the surface for further analysis of different bio-objects, like biomarkers, nucleic acids, antibodies. Nevertheless, the graphene in biology is a relatively young research topic, thus there is still a lot of research to be done. For bioelectronics, either *in vivo* or *in vitro*, compatibility of the electronics with the gating medium needs also to be given. In both cases ionic liquid solutions are surrounding the electrical components, that aims to record/detect specific signals.

6.2.1 Fabrication of GFETs

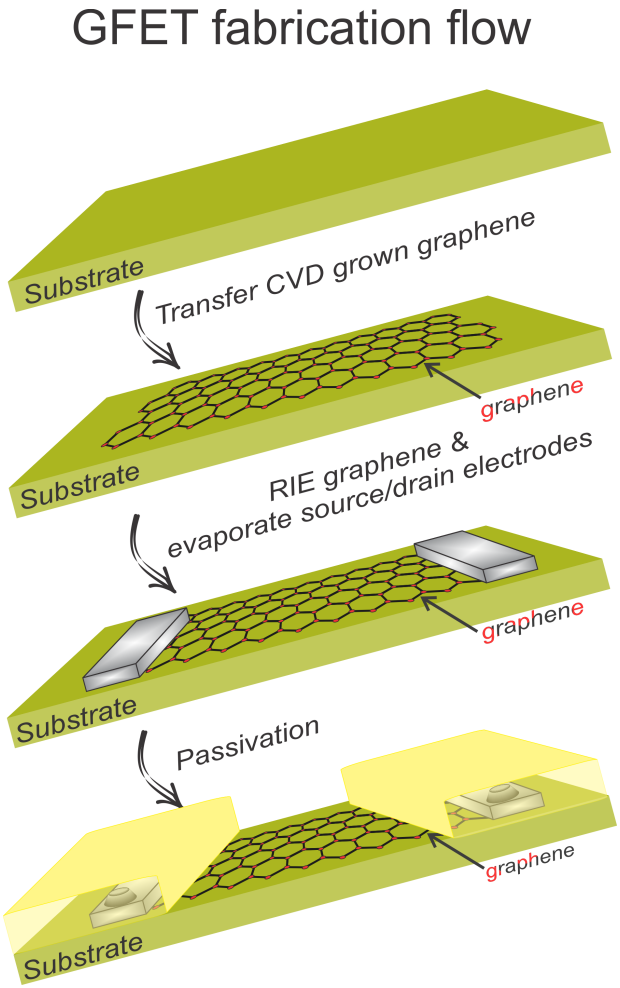

Figure 6.18: Schematic representation of graphene fabrication routine. The fabrication starts with a bare SiO_2/Si substrate, where graphene is transferred, shaped into desired dimensions, then contacted by Ti/Au and passivated with photostructurable photoresist.

When the fabrication step is completed, the next step is to characterize the newly

produced GFETs electrically. This analysis enables further to set the particular parameters of the device for the extracellular signal recordings of the cell cultures. In this work, two main measurement setups were used: Keithley 4200 semiconductor characterization system and BioMAS system. The detailed step-by-step fabrication protocol of the GFETs is shown in the Appendix C, and a short schematic is given in Figure 6.18.

6.2.2 Extracellular recordings with GFETs

Electrophysiology is a study of the behavior of electrically excitable cells and membranes. In order to be able to investigate the interactions between cells and (micro) electronics, it is necessary to understand the fundamentals of the electrophysiological processes, chemical and voltaic changes, occurring in cells and tissues. All cells establish homeostasis due to the surrounding the whole cell membrane that acts as a barrier between the internal and external environment. The cell membrane is formed mostly by a bilayer of phospholipids and transmembrane proteins. The layer of lipids is selectively permeable for molecules and especially non-permeable for the charged ions and polar molecules, which are mostly given by the functional proteins inside the cell. This selective permeability allows maintaining an electrochemical gradient, known as the Donnan equilibrium, between the cytosol, where all cells organelles are located, and external environment. For the proper functioning of a cell, the ions concentration inside and outside of the cell should be stabilized. Thus, the permeability of certain inorganic ions is controlled by so-called ion channels (K^+, Na^+, Cl^- and Ca^{2+}) and ion pumps. Ion pumps to transport ions actively against the electrochemical gradient and consumes energy for this purpose; it is called active transport. On the other hand, ion channels are passive transporters, which transport ions selectively across the membrane and open-close due to specific gating mechanisms (passive transport). Those mechanisms can be driven by different factors, such as ligand binding (ligand-gated channels), change in mechanical stress (mechanically-gated channels) or voltage changes across the membrane (voltage-gated channels). Ligand-gated ion channels control the ability of the channels to open and close in response to the binding of specific molecules to the receptors that are located in the pocket of the ion channels. Fast voltage-gated ion channels have the ability to change their conformation (open-close) when the electrical potential across the membrane is changing [113]. Ion channels are present not only in the

electrically excitable cells such as nervous or muscle systems, where they mediate electrical signal propagation but also in all kind of other cells, e.g. inner ear hair cells [114]. For this, the fast voltage-gated ion channels are of the biggest interest, since they are a necessary condition for the signal propagation. The conclusion of the Donnan equilibrium leads to two consequences, namely a chemical gradient from the concentration differences and a resulting electric field due to the fact that those unevenly distributed ions inside and outside of the membrane are charged. When only considering the K+ ions in the equilibrium state as a first approximation, the Nernst equation is gained:

$$V = \frac{RT}{zF} \cdot \ln \frac{C_{out}}{C_{in}}$$

where R is universal gas constant, z is valency of charge of ion, F is Faraday constant, T is absolute temperature; C_{out} and C_{in} are ionic concentrations outside and inside the cellular membrane.

The concentration of potassium ions is higher inside the cell since the positive charges are compensated by the negative charges of the non-permeable anions. The resting potential of the cell is at about –80mV at 37°C, which is as a first-order approximation in an agreement with the resting potentials in animal cells ranging from –20mV to –200mV, depending on the organism and cell type [113]. However, taking into considerations only K^+ ions and its chemical concentrations is not enough to explain the action potential formation in neuronal cells. Having a biochemical description of the membrane allows describing the membrane as an electrochemical equivalent circuit picture. The specialized fast voltage-gated ion channels are seen as transistors, which, depending on the membrane potential, increase their conductance for the specific current types. Those currents are given by the ion fluxes of K^+, Na^+, Cl^- and Ca^{2+}. While Ca^{2+} influx is undoubtedly relevant for example in postsynaptic signal amplification, known as homosynaptic facilitation, or the monitoring of Ca^{2+} via calcium imaging, it can be neglected in a first simplification of the Goldman equation, even though calcium ions have the highest chemical gradient with a concentration ratio of 10000:1 of outside to inside of the cell [113]. Similarly, the Cl^- ions that play an important role as the calcium antagonist and inhibit post-synaptic potential rises are also neglected. Taking all the considerations into account, the Goldman equation is simplified to:

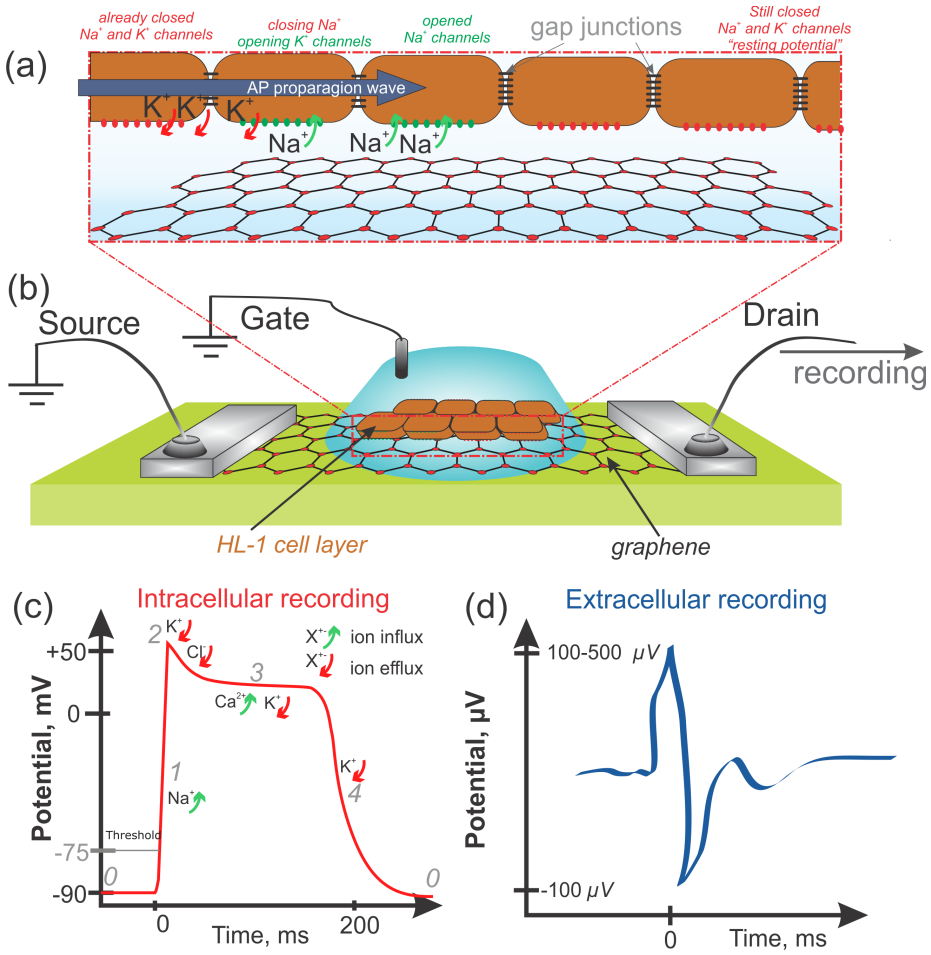

Figure 6.19: Schematic representation of (a) HL-1 cardial cellular layer on top of (b) GFET channel. The Ap propagation along with ionic flows inside and outside of cellular membrane are schematically shown. (c) represents dinamics of cardiac AP if recorded as intracellular potential, while a corresponding etracellular/membrane potential, which is rather a derivative of the intracellular signal is shown in (d).

$$V = E_0 \cdot \ln \frac{P_{K^+}[K^+]_{out} + P_{Na^+}[Na^+]_{out}}{P_{K^+}[K^+]_{in} + P_{Na^+}[Na^+]_{in}}$$

Experimentally, it is expected that the resting potential overall species is lower than the calculated one by about 10mV. This discrepancy is due to the fact that the equations do not factor in the Na^+/K^+-pumps, which are needed to keep the potential at rest and are, within one cycle, pumping out three Na+ ions while pumping in two K^+ ions. If a single cardiac-line cell or a cellular layer is placed on top of an electrode or a transistor, the coupling model will be exactly similar to the one in Figure 6.19a with associated ionic flow through the cellular layer. HL-1 cells, upon maturation, are grown into a continuous layer, which *"beats"* continuously and

the electrical signals are propagated through the layer via formed gap junctions. Gap junctions are a kind of electrical synapses, that directly connected to each other, and the cytoplasms of the (neighboring) cells are connected by intracellular channels. This allows direct transmission of the electrical ionic currents and other species with almost no transmission delay. The resting membrane potential of skeletal muscle is about -90 mV. The depolarization of the membrane, that is essentially the basis of electrical signal propagation in electrogenic cells happens when a certain threshold is over-reached. At this threshold potential, the fast sodium channels open (See Fig. 6.19c) and, due to the chemical gradient, flow into the cell. In cardiac cells, the voltage-gated sodium channels threshold lies around –75 mV. The stimulus needs to depolarize the membrane to this level, where the values in the Goldman equation turn from $P_{K^+} > P_{Na^+}$ to $P_{Na^+} > P_{K^+}$. This phase is called depolarization. The depolarization phase ends at a plateau, which can without external stimuli maximally be at the equilibrium potential for Na^+ +55 mV, depending on a species. After 2-3 ms of the depolarization, Na^+ channels inactivate and stay in this state until the membrane potential return back to its initial negative value. This process is called re-polarization At the same time slower voltage-gated K^+ and Ca^{2+} channels open and re-polarize the activated membrane and bring it back to the negative or even lower resting potential. The cardiac action potential lasts milliseconds due to a slow re-polarization of the Ca^{2+} channels with the slightly prolonged re-polarization period up to the 200 milliseconds After reaching the threshold, which is about -90 mV, action potential is initiated and is presented in few steps. The whole process can be shortly summarized as follows:

- rapid de-polarization(0);
- rapid re-polarization phase(1);
- prolonged plateau of re-polarization (2) that is characterized by slow openings of voltage-gated Ca^{2+} channels;
- late rapid re-polarization (3);
- initial membrane potential (4).

While Figure 6.19a shows the above-presented dynamics of the ionic flow of corresponding potentials, these are intracellular potentials. What is then recorded by a

GFET is a rather membrane potential, or an extracellular potential. The schematic representation of such extracellular recording in shown in 6.19d and represents a rather 1st order derivative of the intracellular signal, yet it can be used to correspond to the main bioelectrical features of the cell.

6.2.3 Modulated ischemia/reperfusion on GFETs

Myocardial infarction (MI), commonly known as a heart attack, occurs when blood flow decreases or stops to a part of the heart, causing damage to the heart muscle. Often it occurs in the center or left side of the chest and lasts for more than a few minutes. The discomfort may occasionally feel like heartburn. Other symptoms may include shortness of breath, nausea, feeling faint, a cold sweat, or feeling tired. About 30% of people have atypical symptoms. Women more often present without chest pain and instead have neck pain, arm pain, or feel tired. Among those over 75 years old, about 5% have had an MI with little or no history of symptoms. An MI may cause heart failure, an irregular heartbeat, cardiogenic shock, or cardiac arrest, and even myocardial ischemia. Myocardial ischemia is responsible for angina, unstable angina, and, less commonly, shortness of breath secondary to ischemic left ventricular dysfunction (angina equivalent) as well as cardiac arrhythmias. Myocardial ischemia occurs when blood flow to your heart is reduced, preventing it from receiving enough oxygen. The reduced blood flow is usually the result of a partial or complete blockage of your heart's arteries (coronary arteries). It is also might cause serious abnormal heart rhythms. Treatment for myocardial ischemia involves improving blood flow to the heart muscle. Treatment may include medications, a procedure to open blocked arteries or bypass surgery. Making heart-healthy lifestyle choices is important in treating and preventing myocardial ischemia.

If impaired blood flow to the heart lasts long enough, it triggers a process called the ischemic cascade. The ischemic cascade is a series of biochemical reactions that are initiated in the aerobic tissues after seconds to minutes of ischemia (inadequate blood supply) [115]. This is typically secondary to stroke, injury, or cardiac arrest due to a heart attack. Most ischemic cells that die, do so due to the activation of chemicals produced during and after ischemia [116] . The ischemic cascade usually goes on for two to three hours but can last for days, even after normal blood flow returns [117]. A cascade is a series of events in which one event triggers the next, in a linear fashion. Thus, "ischemic cascade" is actually a misnomer, since the events

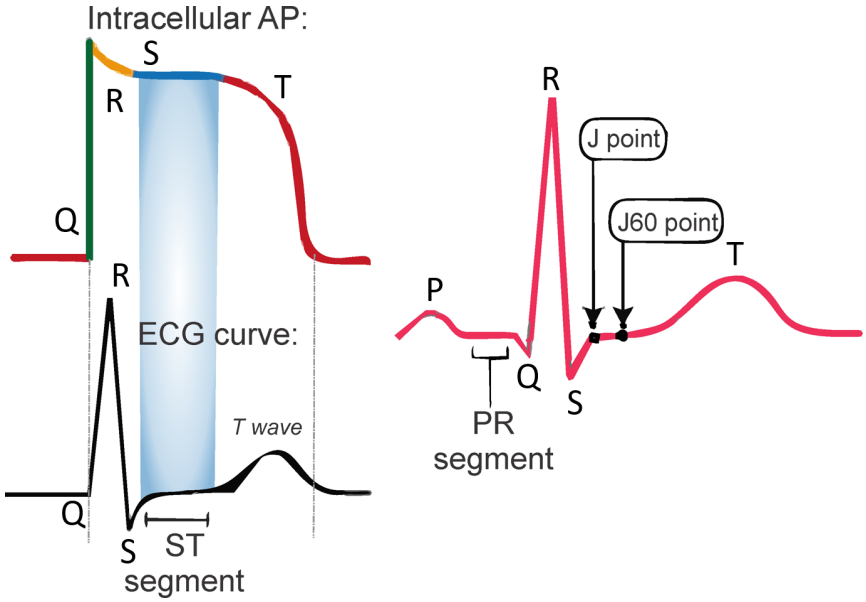

Figure 6.20: Action potential inside a (heart tissue) cell and a corresponding electrocardiogram curve that can be recorded with ST-, and PR-segments marked.

are not always linear: in some cases they are circular, and sometimes one event can cause or be caused by multiple events [118]. In addition, cells receiving different amounts of blood may go through different chemical processes. Despite these facts, the ischemic cascade can be generally characterized as follows:

1. Lack of oxygen causes the cells normal process for making adenosine triphosphate (ATP) for energy to fail.

2. The cell producing lactic acid to prepare for anaerobic metabolism.

3. ATP-reliant ion transport pumps fail, causing the cell to become depolarized, allowing ions, including calcium (Ca^{2+}), to flow into the cell.

4. Intracellular calcium levels get too high and ion pumps can no longer transport calcium out of the cell.

5. The presence of calcium triggers the release of the excitatory amino acid neurotransmitter glutamate.

6. Glutamate stimulates AMPA (amino-3-hydroxy-5-methyl-4-isoxazolepropionic acid) receptors, or quisqualate receptors, and Ca^{2+} -permeable NMDA (N-methyl-D-aspartate) receptors, which open to allow more calcium into cells.

7. Excess of calcium causes the generation of harmful chemicals like free radicals, reactive oxygen species, and calcium-dependent enzymes.

8. Cell membrane is broken down by phospholipases and becomes more permeable, and more ions and harmful chemicals flow into the cell.

9. Mitochondria break down, releasing toxins and apoptotic factors into the cell.

10. The caspase-dependent apoptosis cascade is initiated, causing cells to "commit suicide".

11. If the cell dies through necrosis, it releases glutamate and toxic chemicals into the environment around it.

12. If and when the reperfusion occurs, a number of factors lead to reperfusion injury.

13. An inflammatory response is mounted, and phagocytic cells engulf damaged tissue.

As a result, the heart cells in the area of the blocked coronary artery die (infarction), mainly through necrosis, and do not grow back. A collagen scar forms in their place. When an artery is blocked, cells lack oxygen, needed to produce ATP in mitochondria. ATP is required for the maintenance of electrolyte balance, particularly through the Na/K ATPase. This leads to an ischemic cascade of intracellular changes, necrosis, and apoptosis of affected cells [119]. Cells in the area with the worst blood supply, just below the inner surface of the heart (endocardium), are most susceptible to damage [8]. Ischemia first affects this region, the subendocardial region, and tissue begins to die within 15-30 minutes of loss of blood supply. The dead tissue is surrounded by a zone of potentially reversible ischemia that progresses to become a full-thickness transmural infarct [119]. The initial "wave" of infarction can take place over 3-4 hours [119]. These changes are seen on gross pathology and cannot be predicted by the presence or absence of Q waves on an ECG [8]. The position, size, and extent of an infarct depends on the affected artery, totality of the blockage, duration of the blockage, the presence of collateral blood vessels, oxygen demand, and success of interventional procedures [120], [121]. Tissue death and myocardial scarring alter the normal conduction pathways of the heart and weaken affected areas. The size and location put a person at risk of abnormal heart

rhythms (arrhythmias) or heart block, aneurysm of the heart ventricles, inflammation of the heart wall following infarction, and rupture of the heart wall that can have catastrophic consequences [122]. In prolonged ischemia (60 minutes or more), hypoxanthine is formed as a breakdown product of ATP metabolism. The enzyme xanthine dehydrogenase acts in reverse, that is as a xanthine oxidase as a result of the higher availability of oxygen. This oxidation results in molecular oxygen being converted into highly reactive superoxide and hydroxyl radicals.

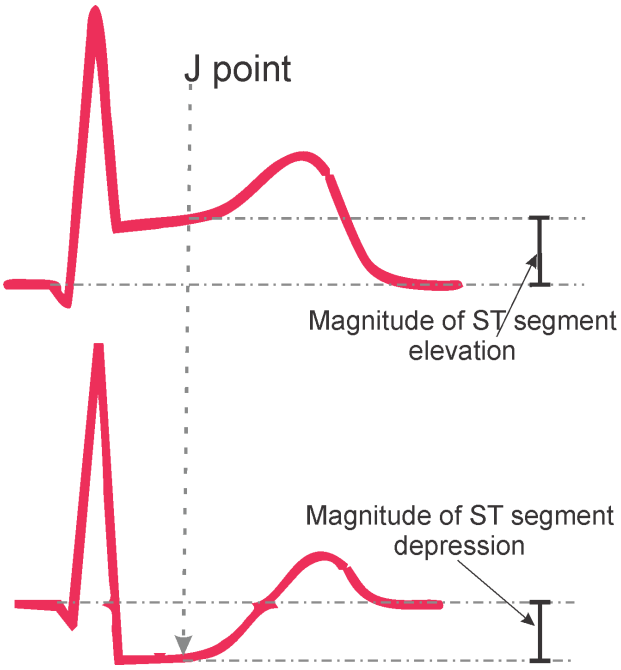

Figure 6.21: Elevation and depression of the ST-segment as a result of ischemia.

The most important parameters in understanding ischemia and recorded APs is the shape of T-wave, duration and elevation/depression of the ST segment as can be seen from Figure 6.20. ST segment is the plateau phase intracellularly as well as extracellularly. Acute ischemia is almost always confined to a specific area, *restricting* the membrane potential change. Consequently, an electrical potential difference occurs, therefore displacing the ST-segment up or down (see Figure 6.21). The T-wave represents the rapid repolarization phase, whose shape, direction and amplitude typically can be related to a great number of studies. Since the T-wave and ST-segment are adjacent, it is important to consider both of them for the overall discussion of ischemia. The J-point and J60 point (that is 60 ms further from J-point) are the figures of merit that are used in order to later evaluate the depression and elevation of ST-T complexes as a result of ischemia (see Figure 6.21). The

ST segment elevation/depression is measured from the baseline to the potential of J-point.

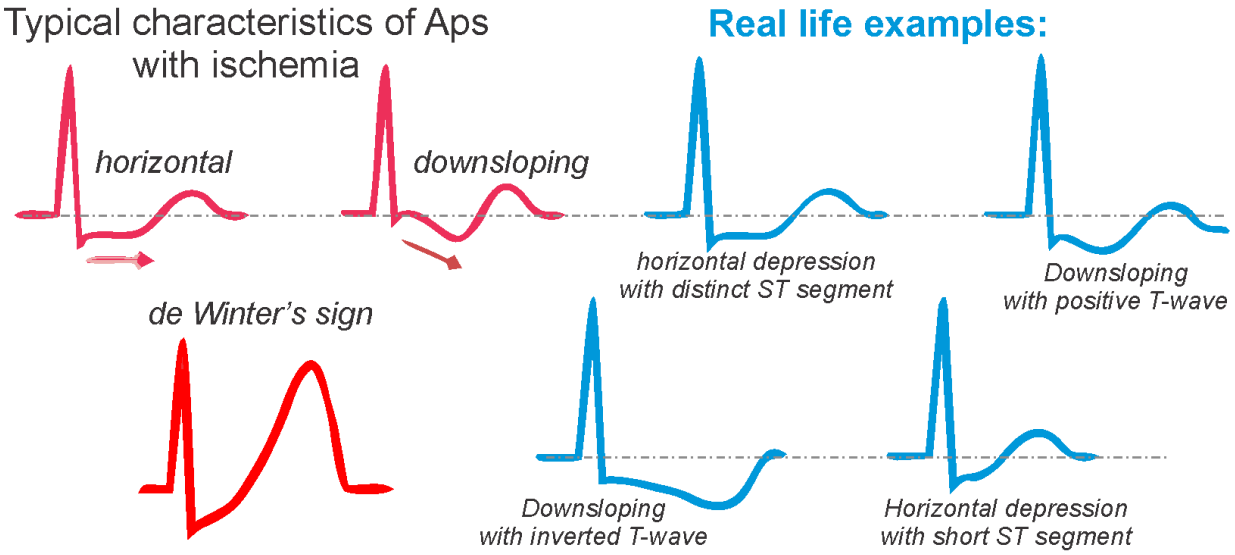

Figure 6.22: Action potentials that are classical with ischemia including different cases downsloping and horizontal depression of ST segments along with positive or negative T-waves.

Reperfusion injury or reperfusion insult, sometimes called ischemia-reperfusion injury (IRI) or re-oxygenation injury, is the tissue damage caused when blood supply returns to tissue (reperfusion) after a period of ischemia or lack of oxygen (anoxia or hypoxia). The absence of oxygen and nutrients from blood during the ischemic period creates a condition in which the restoration of circulation results in inflammation and oxidative damage through the induction of oxidative stress rather than (or along with with) restoration of normal function. Excessive nitric oxide produced during reperfusion reacts with superoxide to produce the potent reactive species peroxynitrite. Such radicals and reactive oxygen species attack cell membrane lipids, proteins, and glycosaminoglycans, causing further damage. They may also initiate specific biological processes by redox signaling.

Once the GFETs are fabricated as described in the experimental section, they were further prepared for cell culture experiments and study of cardiac ischemia states. To model the cardiac ischemia, HL-1 cell line was chosen as a model culture. Growth and typical recordings of HL-1 regional activity have been previously reported to be done not only via MEAs [106,107], but also via Si-FETs [123] as well as GFETs [124]. HL-1 cell line was chosen as a representative model because similarly to the heart tissue, it forms a confluent layer on a surface, where the individual cells are connected

to each other through gap junctions, and the action potentials (APs) propagate through the layer by means of influx and efflux of K^+ and Na^+ ions (mainly these two, but Ca^{2+} and Cl^- also play a role). Additionally, a mature HL-1 culture also has several pacemaker cells, that are special kind of cells, that constantly and regularly create the membrane over-potential (causing to start AP wave). Figure 6.24 shows the schematics of a confluent HL-1 cellular layer on top of a GFET before modulated ischemia.

To summarize, there are miocardal ischemica may cause a set of different changes to the ST-T segment (see Figure 6.22):

- ST elevated;
- ST depressed;
- T-wave diminishes in amplitude (flat T-waves);
- T-wave increases in amplitude (hyperacute T-waves);
- T-wave becomes negative (T-wave inversion);
- de-Winter‘s sign (see fig. 6.22), that is an exception from the rule. This sign implies presence of of upsloping ST-segment depression with clear T-wave, which is a sign of acute ischemia, most commonly caused by a proximal occlusion of the left anterior descending artery.

At the beginning, on each graphene FET chip, HL-1 cells have been seed and grown in normal Claycomb medium (similar to those described in the previous section). For ischemia modeling, standard Claycomb medium had been exchanged with the nutrient-deficient medium (ischemic buffer) containing 1.2mM calcium chloride ($CaCl_2$), 0.5mM magnesium chloride ($MgCl_2$), 115mM sodium chloride (NaCl), 5mM potassium chloride (KCl), 5mM 4-(2-hydroxyethyl)- piperazine-1-ethanesulfonic acid (HEPES), pH 5.8-6.0, supplemented with deoxy glucose. After 12 hours, the ischemic period was converted to a reperfusion period by ischemic medium exchange with Claycomb medium. Control HL-1 cells were cultured in freshly prepared Claycomb Medium during the final part of the experiment after Ischemia/Reperfusion injuries.

Figure 6.23 shows a series of time trace recordings of APs from the ischemic cells grown on top of the GFETs. Similarly to the described above, there is a clear

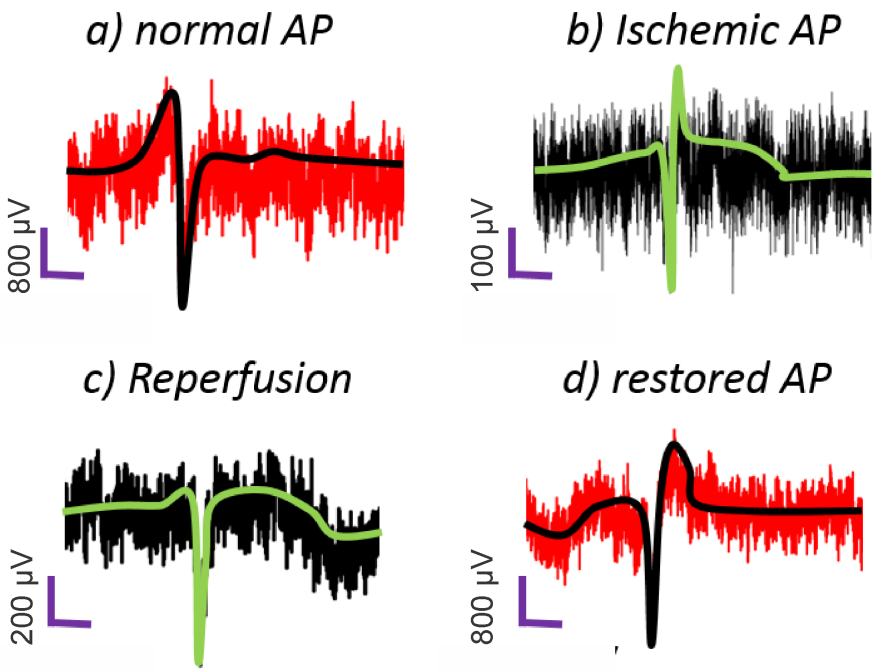

Figure 6.23: Depressed ST segment corresponding to indication of ischemia state.

indication of signal propagation through the cellular layer, meaning a rather live tissue. A closer look into the numerous time traces was given and the APs were analyzed for their shape and signal amplitude (similarly to the published works). Damaged ischemic cell tissue has chances of restoring tissue via early stages of reperfusion by the restoration of blood flow to cells. If re-perfusion is generating relatively quickly then ischemic constructive damages can disappear. The result in Fig. 6.23 shows the time-dependent recovery of the recorded action potential. It is clearly shown that the action potential shape has acquired a proper shape, according to the originally recorded action potential signals. However, it is noticeable that the restored action potential propagates in an inverse way. Such changes of ST segment may occur after the restored ionic exchange in K^+ and Ca^+ channels. Figure 6.24 shows the optical image of the HL-1 cells before and after the induced ischemia. Due to reproducible ischemia, the active confluent layer of cardiac HL-1 cells is no longer bound together. The breaks in the grown cellular layer can be clearly observed.

As a summary of this part of work, many cardiac HL-1 cells were grown to form the grown homogeneous layer. Exchanged ischemic medium caused replacing process of newly grown cardiac cells. Moreover, by looking at the shape of some cells, it can be concluded that ischemia caused the form distortion for some of them. Heart

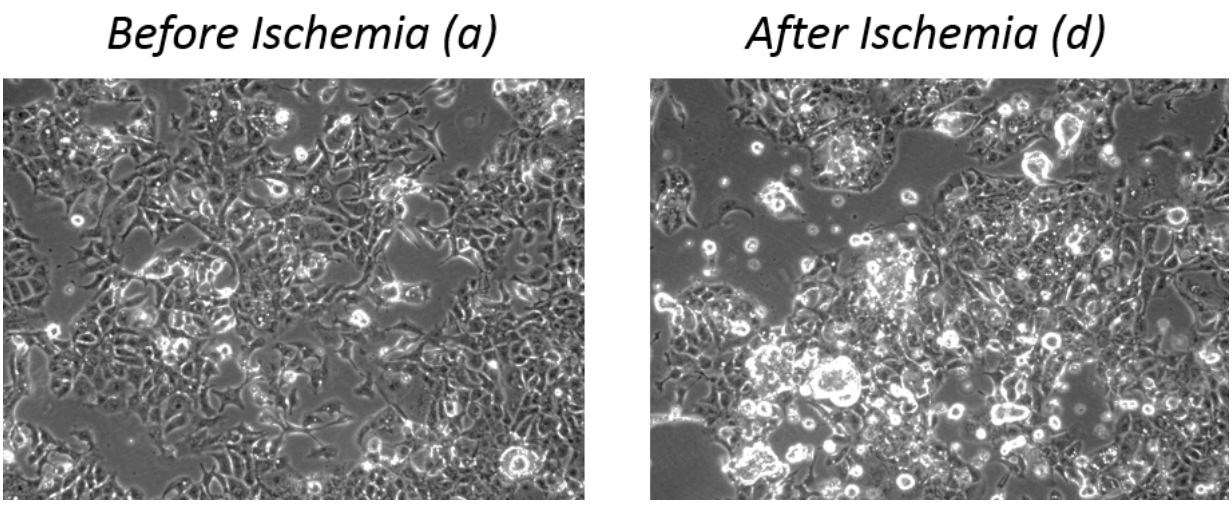

Figure 6.24: (a) normally formed confluent layer of HL-1 cardiac cell line; (b) destroyed cell layer by introduced influence of Ischemic buffer.

diseases and their research are among the vital directions not only in science but also in human life. More and more novel techniques and important discoveries are being added. Therefore, our results allow to understand the importance of research in this area. It is important to understand the processes at the cellular level, as well as to the nature of the molecules and substances responsible for these cellular processes. The presented techniques in this work allow covering the area of studying the heart diseases in every aspect. Moreover, these techniques are suitable for detecting diseases at their early development stages.

Chapter 7

Conclusions and Outlook

In this work I presented, discussed, fabricated and utilized several kinds of biosensors for the detection of biomolecules as well as for electrical activity monitoring of electrogenic cells. The main goal of my work was focused on construction of reliable, accurate, and (ideally) reusable technique for detection of specific biomolecules that are involved in important biochemical processes inside the human organisms. During the work, the microfluidic channel in Zeonex material with low losses was fabricated and used in combination with the WGM resonator (see chapter 4). Electrolyte-insulator-semiconductor structures (see chapter 5) were applied for understanding the biochemical processes at the liquid-solid interface, and optimization of silicon- and graphene-based FET biosensors (see chapter 6) for the detection of cardiac-related biomarkers. In order to perform biosensing experiments, numerous surface modification techniques have been developed, utilized, and improved. For the immobilization protocols that have not been included in the main text of the thesis, please refer to the appendix D.

First of all, in the chapter 4, whispering-gallery-mode resonators, that operate in a K-band microwave frequency range were analyzed from the viewpoint of their applicability for biosensing. To develop the biosensor for bioliquid measurements, the microfluidic channel was customly designed in order to supply the biochemical liquids under study to the resonator region with the maximum of the electro-magnetic field during measurements. The system was found extremely sensitive to the tiniest amount of bioanalytes dissolved in water. Upon the flow of the analyte into the fluidic channel, the changes in the resonance frequency (position/shift) and its shape (quality factor) were recorded. The complex permittivity value of a liquid under test was obtained using calibration monogram plotted on the basis of a COMSOL-based

modeling and series of experimental measurements of liquids with known values of permettivities. In this way, a distinct difference in the response to the presence of water, acetone, methanol, ethanol, and propanol in the microfluidic chamber was recorded for the calibration of the biosensor. More significantly, I demonstrated that the system is sensitive to the two most important antioxidant-specific biomarkers: glutathione and ascorbate in aqueous solutions. These substances reflect concentrations of reactive oxygen species inside of the organism and may be helpful to restore the balance state as well as to prevent many forms of diseases, including cardiac dysfunctions. With this technique I was able to record as low concentrations as **10 µg/L**.

In Chapter 5 of this work I introduced and discussed the biosensor technique based on capacitive electrolyte-insulator (EIS) sensors. The devices are of the great interest for the biosensing due to the simplicity of fabrication and their functional applicability for characterization of very thin-film dielectric layers, important functional layers, as well as for determination the sensor sensitivity. The sensors consist of a thin-film insulator(oxide) layers on top of a Si chip. Silicon dioxide layer was typically used as the topmost layer due to (1) the simplicity of it‘s fabrication in the cleanroom, (2) suitability to upscale the immobilization technologies for the EIS and for FET structures. A direct “pick-and-place an aptamer on a surface” method is not possible chemically since most of the biomolecules require to be immobilized on the surface. During the work, several important immobilization protocols were developed. They allowed to establish a connection of antibodies or aptamers to the surface of the insulator as well as to enhance non-specific binding sites, and to eliminate non-specific sensing. Overall, presented research shows that EIS structures are very robust and multifunctional components for the biosensing technique, that in this case allowed us to perform the characterization of such cardiac biomarkers as Troponin I and C-reactive protein via different approaches:

1. **Antibody**-antigen based biosensing

   with concentration down to **1 µg/L**.
2. **Aptamer**-antigen based biosensing

   with concentration down to **0.01 µg/L**.

In Chapter 6 I continued with more elaborated biosensors, namely the field-effect transistor based biosensors. This part of the work is focused on two kinds of struc-

tures:

1. **Silicon**-NW FETs

   with SiO_2 dielectric on top, allowing us to use the developed immobilization protocols for the EIS structures, described in Chapter 5 of this work. Transport and noise characteristics of silicon-based FETs were studied before and after successful immobilization of C-reactive protein molecules as well as cardiac Troponin I molecules with concentrations down to 0.1 µg/L.
2. **Graphene**-based FETs (GFETs)

   with rather different surface properties but superior liquid stability and performance, allowing new functionalities.

   dynamics of cardiac ischemia arrest was studied in HL-1 cell culture grown directly on the sensors.

Both Si-FETs and GFETs have been used to successfully record and to study the extracellular action potentials from an electrogenic cardiac cell line, HL-1. However, GFETs structures have demonstrated a larger signal-to-noise ratio and stability as well as durability of the devices, therefore they were used to study ischemia. In section 6.2 it is shown that the recordings of APs, their amplitude and shape changes allow obtaining signals accordingly to different stages of introduced ischemia arrest in the HL-1 cell culture. The recordings of APs by GFETs demonstrated clear features in APs corresponding to different stages of the ischemia. These findings are very important to take this work forward in order to develop the detection of ischemia state even *in vivo* at early stage. Usage of graphene is essential in this biosensors because the devices can be easily fabricated in form of flexible and even stretchable as well as implanted structures into living tissue.

As an outlook, the applicability of WGM resonator technique operating on a higher frequency (170 GHz) compared with 34 GHz studied in this work will allow to decrease the liquid volume under test down to 0.1-1 µg/L. In future the enhancement of sensitivity and selectivity of both Si- and graphene-based biosensors can be obtained with the utilization of aptamers as surface functionalization agents. While the development of aptamer-SiO_2 and aptamer-graphene attachment are two very different techniques, they are becoming more and more commonly utilized. It is expected that our technology cane be integrated in advanced biosensors and a number

of challenged will be solved toward recording the analytes with concentrations down to 1 ng/L.

Acknowledgments

First of all I would like to thank **Prof. Svetlana Vitusevich** for the great supervision, constant support, scientific discussions and help in many aspects of scientific and real life.

Prof. A. Offenhausser – thank you for the opportunity to do scientific research in Forschungszentrum Juelich.

Ihor Zadorozhnyi, Volodymyr Handzuik, Yurii Kutovyi – thank you for always being in collaboration work as a part of the project, help with all electrical measurements and for the great four years together. It was great to work with you!

Dr. Dirk Mayer – for discussing, helping, understanding and realization of the chemical parts of all experiments related to this project.

Michael Prömpers and **Marko Banzet** – for the clean-room guidance, support and help with fabrication processes.

Dr. Vanessa Maybeck – thank you for being the mentor in the cell culture routine and in all related experiments and data interpretation.

Bettina Breuer - for taking care of all cell-related preparations and support in cell culture labs.

Fabian Brings – for the teaching and helping with electronics of the cell-related measurement set-ups.

Dr. Andreea Belu – thank you for the fun part of these years.

Dr. Dmitry Kireev – thank you for believing in me and support throughout my journey.

my Family – thank you for always being on my side no matter what.

Appendices

Appendix A

Cell culture, daily care and protocols

Chip Preparation and culture HL-1 Cardiac Cell Line

Reagents acquired: coating Fibronectin/Gelatin, autoclaved beaker, 100% ethanol, 60mm Petri dish.

1. Take a Fibronectin/Gelatin aliquot from a freezer in into sterile bench;
2. Take an autoclaved beaker;
3. Fill beaker with a pure 100% ethanol;
4. Immerse chips into the beaker with ethanol;
5. Close beaker with aluminum foil and leave it for 10–15 min;
6. Move beaker into the bench;
7. Take chips from solution, dry then with N_2 gun;
8. Place cleaned chips in a 60mm Petri dish;
9. In each chip add desired amount of Fib/Gel;
10. Place chips in Incubator and leave for 60 min;
11. After 45 minutes while chips are at the incubator you can start split cells;
12. Prepare the following reagents: Trypsin (2 mL), T-25 flask, Claycomb Medium, falcon tube (15 mL), pipette (5 mL);
13. Transfer T-25 flask with cells from incubator to bench;

14. Using glass suction take off a 99% of liquid;
15. Add 1mL of Trypsin, wash cells for 1 min, aspirate immediately;
16. Add 1 mL of Trypsin and return T-25 flask to incubator for 5 min;
17. Transfer T-25 flask with cells and Trypsin from incubator to bench;
18. Add 5 mL Claycomb Medium and transfer all 6 mL to a falcon tube (15 mL);
19. Centrifuge for 5 min at 1700 RPM at RT.
20. After centrifuge you will see a precipitate in falcon tube. Aspirate all liquid in falcon tube close enough to this precipitate.
21. Re-suspend cells in 1 mL of Claycomb Medium Pre-fill a new T-25 flask with 5 mL of Claycomb Medium.
22. Prepare the following reagents: Bidest water, centrifuged cells in 15 mL falcon tube, Claycomb medium;
23. Bring to the bench Bidest Water and Chips from incubator;
24. Suck out liquid from Chips;
25. Place solution of fibronectin and gelatin (5 μg/ml and 0.2 mg/ml) in double distilled water;
26. Incubate the protein solution on the chips at 37°C, 5% CO_2, for 1 hour;
27. Wash Chips with Bidest Water x3 times and dry with N_2 gun;
28. Add to each Chip desired amount of cells;
29. After centrifuge you will see a precipitate in falcon tube. Aspirate all liquid in falcon tube close enough to this precipitate;
30. Transfer desired amount of cells into each chip;
31. Wait 30 min;
32. Add to each chip some Claycomb Medium;
33. Grow at 37°C, 5% CO_2;

34. Preparation of Supplemented Claycomb medium:
    - Take an autoclaved glass bottle;
    - Mix stock Claycomb Medium, FBS, Penn/Strep, L-glutamine, and nor-A;
    - See Table A.1 for details on concentrations
    - Mix all chemicals step by step in autoclaved glass bottle starting from Medium;
    - Cover bottle with aluminum foil since it is light sensitive.
    - Put your bottle in a refrigerator 4°C.

Feeding Cells:

- Take your Medium from refrigerator to the water bath for 5 min;
- Put T-25 flask with cells and Medium to bench;
- Using glass suction take off 90% of liquid.
- Place your T-25 flask inclined.
- Add desired amount of Medium to your flask. (5 mL - one night, 10 mL - over weekend). Close your T-25 flask and return it to incubator.

Table A.1: Supplemented Claycomb medium used for HL-1 cells. The listed below substances are added into Claycomb medium with specified concentrations.

Substance	Add volume	Stock solution	Final Concentration
Claycomb medium	100 ml	—	—
Fetal bovine serum	11.2 ml	—	10% (v/v)
Penicillin Streptomycin	1.14ml	10^4 units/ml 10^4 µg/ml	100 units/ml 100 µg/ml
Norepinephrine	1.14ml	10 mM	0.1 mM
L-glutamine	1.14ml	200 mM	2 mM

Terg-A-zyme cleaning

In order to carefully remove a cellular layer from a chip's surface after each culture, a Terg-A-zyme assisted cleaning is performed. Terg-A-zyme is a concentrated anionic detergent with protease enzyme typically used ultrasonic cleaning. The overall protocol is given below:

1. Prepare a 1% Terg-A-zyme solution in DI water;
2. Soak a chip in the 1% Terg-A-Zyme solution for at least one hour;
3. Rinse thoroughly with running water.

List of Chemicals

Table A.2: List of chemicals used for cell culture with embryonic rat cortical neurons and HL-1.

Substance	Supplier
Claycomb medium	Sigma-Aldrich
ethanol	Riedel-de Haën
Bovine serum albumin	Sigma-Aldrich
fibronectin	Sigma-Aldrich
GBSS	Sigma-Aldrich
gelatin	Sigma-Aldrich
glucose	Sigma-Aldrich
glutaraldehyde	Sigma-Aldrich
HEPES	Sigma-Aldrich
isopropanol	Merck
KCl	Sigma-Aldrich
KH_2PO_4	Sigma-Aldrich
L-glutamine	Life Technologies
$MgCl_2$	Sigma-Aldrich
NaCl	Sigma-Aldrich
NaOH	Sigma-Aldrich
norepinephrine	Sigma-Aldrich
penicillin/streptomycin	Life Technologies
trypsin EDTA	Life Technologies
terg-A-zyme	Sigma-Aldrich
2-Deoxy-D-glucose	Sigma-Aldrich
DMEM	Fisher Scientific
GPTES	Sigma-Aldrich
APTES	Sigma-Aldrich

Table A.2: List of chemicals (continued).

Substance	Supplier
L-glutathione reduced	Sigma-Aldrich
L-ascorbic acid	Sigma-Aldrich
Anti-CRP antibody	Sigma-Aldrich
Monoconal Anti-CRP antibody	Sigma-Aldrich
PrEST Antigen CRP	Sigma-Aldrich
Monoconal Anti-TNNI3 antibody	Sigma-Aldrich
Anti-TNNI3 antibody	Sigma-Aldrich
PrEST Antigen TNNI3	Sigma-Aldrich
Glycine	Sigma-Aldrich

The chemicals used for all cell culture related protocols are listed here and were supplied by one of the following companies:

- Sigma-Aldrich Chemie GmbH, Taufkirchen, Germany (Sigma-Aldrich)
- Life Technologies GmbH, Darmstadt, Germany (Life Technologies)
- Merck KGaA, Darmstadt, Germany (Merck)

Table A.3: Recipe for phosphate buffered saline (PBS). The reagents were dissolved in bi-distilled water, and the pH-value was adjusted to 7.4 with NaOH.

Chemical	Concentration (mmol/l)
NaCl	137
KCl	2.7
Na_2HPO_4	8.1
KH_2PO_4	1.47

Ethics statement. The experiments were done with the approval of the Landesumweltamt für Natur, Umwelt und Verbraucherschutz Nordrhein-Westfalen, Recklinghausen, Germany, number 84-02.04.2015.A173.

Table A.4: Ischemic buffer: Consists of a mixture of DMEM, non-essencial amino acids pH=6.2. The final concentration of the overall solution is as follows:

Chemical	Name	Concentration
NaCl	sodium chloride	118 mM
KCl	potassium chloride	12 mM
$MgCl_2$	magnesium dichloride	0.49 mM
$CaCl_2$	calcium chloride	0.9 mM
HEPES	(4-(2-hydroxyethyl)-1-piperazineethanesulfonic acid)	4 mM
$C_3H_5NaO_3$	sodium lactate	20 mM
$C_6H_{12}O_5$	deoxyglucose	5 mM
$NaHCO_3$	sodium bicarbonate	6.25 mM
NaH_2PO_4	sodium dihydrogen phosphate	0.2 mM
KH_2PO_4	potassium phosphate	0.8 mM

Appendix B

Cleanroom fabrication steps

Metallization

A double layer of LOR-3B and AZ nLOF-2020 was always used for metallization. The overall process is described below:

- **Dehydration:** 150°C anneal on a hotplate for at least 5–10 minutes.
- **Spin-coating:** LOR-3B, 3000 rpm, with ramp, closed lid, 5 ml, disperse around the whole wafer, otherwise causing problems;
- **Soft bake:** 150°C, 5 minutes, hotplate;
- **Spin-coating:** AZ nLOF-2020, 3000 rpm, with ramp, closed lid, 3 ml;
- **Soft bake:** 100°C, 2 minutes, hotplate;
- **Exposure:** i–line, 40 mJ/cm^2;
- **Post-exposure bake:** 110°C, 1 minute, hotplate;
- **Develop:** in AZ 326 MIF for approximately 33-35 seconds;
- **Washing:** water cascade, drying with N_2 gun;
- **e-beam assisted evaporation of the desired metal stack**
- **Lift–off** in acetone overnight. Following clean in IPA, AZ 326 MIF, and water cascade

Defining graphene areas

Using AZ-5214e resist as a common, thick and easy photoresist.

- **Dehydration:** 150°C, for at least 5–10 minutes, hotplate.
- **Spin-coating:** AZ-5214e, 3000 rpm, with ramp, closed lid, 3 ml;
- **Soft bake:** 110°C, 1 minute, hotplate;
- **Exposure:** i–line, 50 mJ/cm^2;
- **Develop:** in AZ 326 MIF for approximately 60–70 seconds. The margin depends on the structure and external parameters;
- **Washing:** water cascade, drying with N_2 gun;
- **Oxygen plasma**, Barrel Reactor TePla Gigabatch 310M, 300W, 200 sccm, 10 minutes;
- **Remove AZ-5214e** in acetone for 10 minutes;
- **Clean** in IPA and N_2 blow dry.

Passivation

- **Dehydration:** 150°C, for at least 5–10 minutes, hotplate.
- **Spin-coating:** VM-652 adhesion promoter (always use a fresh one), 3000 rpm, closed lid, 3 ml;
- **Spin-coating:** HD-8820, 5000 rpm, closed lid, 3-4 ml, disperse directly from a bottle;
- **Slow soft bake:** up to 120°C and 4 min;
- **Exposure:** i–line, 250 mJ/cm^2;
- **Develop:** in AZ 326 MIF for 75-90 seconds;
- **Washing:** water cascade, drying with N_2 gun;
- **Hard bake in a convection furnace:** up to 350°C.

Appendix C

Fabrication details

Thin-film dielectric layers

1. **RCA cleaning**.

   Piranha (H_2O_2 + H_2SO_4 (1:3)).

   SC-1 (DI water, NH_4, 30% H_2O_2 (5:1:1)) at 75-80°C, 10 minutes.

   SC-2 (DI water, 29% hydrochloric acid, 30% H_2O_2 (7:1:1)) at 75-80°C, 10 minutes.

   HF (DI water, 48% hydrofluoric acid, (50:1)) at 20-25°C, 1-2 minutes.

2. **Oxidation** of silicon active layer (2 nm - 30 nm). Dry oxygen atmosphere, 1000°C, 30 minutes.

3. **Spin-coating** of AZ-5214 (3 ml) as a protective layer, 3000 rpm, 30 sec, 5 sec pre-acceleration, closed lid.

4. Buffered oxide **etching** to remove native oxide from backside (BOE, 30% NH_4, (10:1)).

5. **Metallization** of approximately 50nm aluminum for good ohmic contact.

   Thermal **annealing** 350°C, hotplate, 5 minutes .

6. **Dicing** into 10x10 mm^2 pieces.

7. Removing the protective resist.

   Washing in acetone (5min), IPA, and drying with N_2 gun.

Si NW FETs

1. **RCA cleaning**.

   Piranha (H_2O_2 + H_2SO_4 (1:3)).

   SC-1 (DI water, NH_4, 30% H_2O_2 (5:1:1)) at 75-80°C, 10 minutes.

   SC-2 (DI water, 29% hydrochloric acid, 30% H_2O_2 (7:1:1)) at 75-80°C, 10 minutes.

2. **Oxidation** of silicon active layer. Dry oxygen atmosphere, 1000°C, 30 minutes

3. **Photolithography**

   Dehydration at 180°C, hotplate, 5-10 minutes, cooldown 5sec.

   Spin-coating of adhesion promoter HMDS (3 ml), 6000 rpm, 1 minute, 5 sec pre-acceleration, closed lid.

   Spin-coating of AZ-5214 (3 ml), 4000 rpm, 1 minute, 5 sec pre-acceleration, closed lid.

   Soft-bake 90°C, hotplate, 5 minutes.

   Exposure 7 mW/cm^2, 6s, without alignment.

   Developing in AZ 326 MIF, 45 sec (depending on the structure)

   Clean in water cascade and drying with N_2 gun.

4. **Patterning** oxide mask in CHF_3 plasma, 1 minute

5. **Removing** AZ-5214 in acetone, then IPA and drying with N2 gun.

6. **Etching** of the silicon active layer, 5% TMAH, at 90°Cfor 15 seconds

7. **Photolithography** using AZ-5214 (the procedure is described above).

8. Forming nanoribbon pattern onto silicon oxide mask in CHF_3 plasma, 1 minute

9. Removing AZ-5214 in acetone, then IPA and drying with N_2 gun.

10. **Patterning** of nanoribbons, 5% TMAH, at 90°Cfor 15 seconds Removing of silicon oxide mask, 1% HF, for 6 min. 30 sec.

11. **Ion implantation**

    Photolithography using AZ-5214 (the procedure is described above)

    Ion implantation (p-type - B, 6 keV, 10^{15} cm^{-2}; n-type - As, 8 keV, 5x10^{14} cm^{-2}.)

    Cleaning in acetone (8-10 hours)

    RCA cleaning (see 1st step)

    Annealing for dopant activating, at 1000°C, 5s for boron; 950°C, 30s for arsenic

12. Forming of back gate opening

    Photolithography using AZ-5214 (the procedure is described above)

    Etching of back gate opening, 10%HF, 3 min

    Removing AZ-5214 in acetone, then IPA and drying with N_2 gun

13. **Metallization** by aluminum for good ohmic contact (see Appendix C)

14. **Metallization** by Ti/Au (see Appendix C)

15. **Passivation** (see Appendix C)

16. **Dicing**

    Spin-coating of AZ-5214 (3 ml) as a protective layer, 3000 rpm, 30 sec, 5 sec pre-acceleration, closed lid.

    Soft-bake 90°C, hotplate, 5 minutes

    Dicing into 5x5 mm^2 pieces.

17. **Washing** in acetone (5min), IPA, and drying with N_2 gun.

GFETs

- **Wafer:** 4-inch, SiO_2/Si with 285nm of SiO_2;
- **1st Metallization:** (10/50 nm) Ti/Au, see details in B;
- **Graphene transfer** see Ref. [125];

- **Define graphene areas:** Oxygen plasma, see details in B;
- **2nd Metallization:** (10/100 nm Ti/Au, see details in B;
- **Passivation:** 3-4 µm thick polyimide HD-8820, details in B;
- **Dicing** GFETs into 11×11 mm^2.

Appendix D

Immobilization Protocols

D.1 Aptamer Immobilization Protocol

Aptamer should be stored at -20°C for long time and at 4°C in fridge for short time (during immobilization protocol). The aptamer solution should be properly thawed and frozen. Aptamer should be activated (at 60°C, or better at 90°C degrees - it depends on its structure).

Solutions required for the following protocol:

- 10mM PBS pH=7.4, 9.0, 10.0;
- 0.1% Tween-20 dissolved in PBS buffer;
- 100mM Ethanolamine dissolved in PBS buffer.
- APTES.

The step-by-step protocol:

1. Surface cleaning (standard procedures);
2. Plasma activation (oxygen plasma with low power can be used);
3. Silanization (APTES), see section D.2;
4. Surface annealing at hot plate (150°C, 3-5 min);
5. Aptamer thawing at 95°C for 1-3 minutes, then cool down to room temperature (10-15 min);

6. Preparation of working aptamer concentration (in 10mM PBS buffer with pH = 7.4);
7. Aptamer activation (at 60°C for 1-3 min);
8. Immobilization could be done at different temperatures (4°C, RT, 37°C) and can take from 3 hours up to 12 hours
9. Remove unbounded aptamers by washing with 10mM PBS buffer with pH = 9.0;
10. Blocking with Tween-20 solution (at RT for 30-45 minutes)
11. * 100mM ethanolamine solution can be used as alternative (at RT for 1 hour)
12. Removing excess by washing with 10mM PBS buffer with pH = 10.0;
13. Perform electrical measurements

D.2 Protein Immobilization Protocols

Immobilization Protocols v.1 (*with amino -NH_2*): for Antibodies and Aptamers:

1. Surface activation (chemical or Oxygen Plasma);
2. Silanize with 1% APTES in Glove Box (5.0 mbar, 1h), see section D.2;
3. Clean with 1mM Acetic acid, dry on a hot plate 100°C3-5 min;
4. Immerse in 50% Glutaraldehyde solution (at RT, 1h);
5. Clean with PBS solution, dry with nitrogen;
6. Immobilize antibodies dissolved in 10mM PBS pH=7.4 (at RT, 1h - 2h);
7. Clean with PBS solution, dry with nitrogen;
8. Block with 0.5M ethanolamine (at RT, 30 min - 45 min);
9. Clean with PBS solution, dry with nitrogen;
10. Measure with different Antigen concentrations.

Immobilization Protocol v.2 (*with epoxy*):

1. Surface activation (chemical or Oxygen Plasma);
2. Silanize with 1% GPTES/GOPS in Glove Box (5.0 mbar, 1h) see section D.2;
3. Clean and Dry with hot plate 100°C, 3-5 min;
4. Immobilize Antibodies dissolved in 10mM PBS pH=7.4 (at RT, 1h - 2h);
5. Clean with PBS solution, Dry with nitrogen;
6. Block with 0.5M ethanolamine (at RT, 30 min - 45 min);
7. Clean with PBS solution, Dry with nitrogen;
8. Measure with different Antigen concentrations.

Immobilization Protocol v.3 *(with 1,1-carbobyldiimidazole, CDI): zero-length cross-linker*

1. Surface activation (chemical or Oxygen Plasma);
2. Silanize with 1% APTES in Glove Box (5.0 mbar, 1h), see section D.2;
3. Immerse in mixture of CDI and acetate buffer pH=5.0 (at RT, 2h);
4. Clean with PBS solution, Dry with nitrogen;
5. Dissolve Antibody in PBS pH=7.0;
6. Immobilize Antibodies (at RT, 1h - 2h);
7. Clean with PBS solution, Dry with nitrogen;
8. Block with 0.5M ethanolamine (at RT, 15 min);
9. Clean with PBS solution, Dry with nitrogen;
10. Measure with different Antigen concentrations;

Immobilization Protocol v.4 *(maleimide activated): cannot be used with glycine!*

1. Surface activation (chemical or Oxygen Plasma);
2. Silanize with 1% APTES in Glove Box (5.0 mbar, 1h), see section D.2;
3. Activate with SMCC (succinimidyl 4-(N-maleimidomethyl) cyclohexane -1-carboxylate) in PBS (at RT, for 30 min);
4. Clean with PBS solution, Dry with nitrogen;
5. Immobilize Antibodies dissolved in 10mM PBS pH=7.4 (at RT, 1h - 2h);
6. Clean with PBS solution, Dry with nitrogen;
7. Block with 0.5M ethanolamine (at RT, 30 min - 45 min);
8. Clean with PBS solution, Dry with nitrogen;
9. Measure with different Antigen concentrations;

Immobilization Protocol v.5 *(with gold nanoparticles)*:

1. Surface activation (hard Oxygen Plasma)
2. Silanize with 1% APTES in Glove Box (5.0 mbar, 1h), see section D.2;
3. Cover surface with solution of nanoparticles with desired size (at RT, 4h - 12 h the longer time the better adhesion);
4. Clean with sufficient amount of DI water, Dry carefully with nitrogen;
5. Prepare in PBS and dilute EDC/NHS ester with Antibodies in ration 1:1:1;
6. Stir mixture for 1h;
7. Immobilize Antibodies on nanoparticles (at RT, 1h - 2h);
8. Clean with PBS solution, Dry with nitrogen;
9. Block with 0.5M ethanolamine (at RT, 30 min - 45 min);
10. Clean with PBS solution, Dry with nitrogen;
11. Measure with different Antigen concentrations;

Immobilization Protocol v.6 *(on gold with UV-light)*:

1. Surface activation (Oxygen Plasma);
2. Silanize with 1% APTES in Glove Box (5.0 mbar, 1h), see section D.2;
3. Cover surface with solution of nanoparticles with desired size (at RT, 4h - 12 h the longer time the better adhesion);
4. Clean with sufficient amount of DI water, Dry carefully with nitrogen;
5. Prepare Antibody solution for immobilization;
6. Cover surface with Antibody solution;
7. Employ UV pulses to produce free thiols to bind gold (at RT, without bright light, for 1 min);
8. Measure with different Antigen concentrations.

Glove-Box Silanization protocols

GPTES:

1. heat the sample inside the glove box (N_2 atmosphere) at 150°C for 5-10 min;
2. place the sample into a desiccator;
3. apply 150 μL of GPTES solution;
4. pump down and open Ar gas supply in order to establish approximately 5 mBar pressure inside the desiccator;
5. continue the process for 90 minutes;
6. turn off the pump, Ar, and unload the samples.

APTES:

1. heat the sample inside the glove box (N_2 atmosphere) at 100°C for 1-2 min;
2. place the sample into a desiccator;

3. apply 150-300 μL of APTES solution;
4. pump down and open Ar gas supply in order to establish approximately 5 mBar pressure inside the desiccator;
5. continue the process for 60 minutes;
6. turn off the pump, Ar, and unload the samples.
7. anneal the sample inside the glove box (N_2 atmosphere) at 150°C for 1-2 min;

Details on processing the chemicals

1. **Glutaraldehyde**:

   dissolved down to 2.5% in 0.1M Phosphate Buffer;

   Add 500ul of 50% glutaraldehyde to 5ml of stock buffer solution;

   Adjust with distilled water to a final volume of 10 ml.

2. **Aptamers**:

   Defrosting at 95°C for 5 min, or 37°C for 15 min;

   Dissolve 100 μL in 1 mL of 10mM PBS buffer with pH of7.4.

3. **Ethanolamine**:

   500mM;

   Add 0.15ml of ethanolamine to 4.8 ml of 0.01M PBS pH=7.4.

4. **Glycine**:

   0.192M;

   Dissolve 1.44 grams of Glycine to a final volume of 100 ml with water or buffer.

5. Elution Buffer

   100mM citric acid pH=5.0.

Bibliography

[1] Hasan, A. *et al.* Recent Advances in Application of Biosensors in Tissue Engineering. *BioMed Research International* **2014**, 1–18 (2014). URL http://www.hindawi.com/journals/bmri/2014/307519/.

[2] Srinivasan, S., Gunasekaran, P. & Rajendhran, J. Fundamentals of Molecular Biology. In *Current Developments in Biotechnology and Bioengineering*, February, 59–80 (Elsevier, 2017). URL https://linkinghub.elsevier.com/retrieve/pii/B9780444636683000032.

[3] Stahmann, M. A. The proteins. composition, structure, and function. volume iii. second edition. *Journal of the American Chemical Society* **88**, 1085–1086 (1966). URL https://doi.org/10.1021/ja00957a059.

[4] Liang, H. W., Huang, Y. P. & Pan, S. L. Parkinson disease and risk of acute myocardial infarction: A population-based, propensity score-matched, longitudinal follow-up study. *American Heart Journal* **169**, 508–514 (2015). URL http://dx.doi.org/10.1016/j.ahj.2014.11.018.

[5] Licastro, F. *et al.* Sharing pathogenetic mechanisms between acute myocardial infarction and Alzheimer's disease as shown by partially overlapping of gene variant profiles. *Journal of Alzheimer's Disease* **23**, 421–431 (2011). URL http://dx.doi.org/10.3233/JAD-2010-090871.

[6] Hamilton, R. G. The Human IgG Subclasses pp 1–76 (1987). URL https://doi.org/10.1016/0167-5699(91)90154-L.

[7] Hodges, R. S., Heaton, R. J., Parker, J. M., Molday, L. & Molday, R. S. Antigen-antibody interaction. synthetic peptides define linear antigenic determinants recognized by monoclonal antibodies directed to the cytoplasmic carboxyl terminus of rhodopsin. *Journal of Biological Chemistry* **263**,

11768–11775 (1988). URL http://www.jbc.org/content/263/24/11768.abstract.

[8] Thygesen, K. *et al.* Third Universal Definition of Myocardial Infarction. *Circulation* **126**, 2020–2035 (2012). URL https://www.ahajournals.org/doi/10.1161/CIR.0b013e31826e1058.

[9] Mythili, S. & Malathi, N. Diagnostic markers of acute myocardial infarction (Review). *Biomedical Reports* 743–748 (2015). URL http://www.spandidos-publications.com/10.3892/br.2015.500.

[10] Chacko, S., Haseeb, S., Glover, B. M., Wallbridge, D. & Harper, A. The role of biomarkers in the diagnosis and risk stratification of acute coronary syndrome. *Future Science OA* **4**, FSO251 (2018). URL http://www.future-science.com/doi/10.4155/fsoa-2017-0036.

[11] Pasceri, V., Willerson, J. T. & Yeh, E. T. H. Direct proinflammatory effect of c-reactive protein on human endothelial cells. *Circulation* **102**, 2165–2168 (2000). URL https://www.ahajournals.org/doi/abs/10.1161/01.CIR.102.18.2165.

[12] Wang, M. S., Black, J. C., Knowles, M. K. & Reed, S. M. C-reactive protein (CRP) aptamer binds to monomeric but not pentameric form of CRP. *Analytical and Bioanalytical Chemistry* **401**, 1309–1318 (2011). URL https://www.ncbi.nlm.nih.gov/pubmed/21725632.

[13] Yasojima, K., Schwab, C., McGeer, E. G. & McGeer, P. L. Human neurons generate C-reactive protein and amyloid P: Upregulation in Alzheimer's disease. *Brain Research* **887**, 80–89 (2000). URL https://doi.org/10.1016/S0006-8993(00)02970-X.

[14] Yasojima, K., Schwab, C., McGeer, E. G. & McGeer, P. L. Generation of C-reactive protein and complement components in atherosclerotic plaques. *American Journal of Pathology* **158**, 1039–1051 (2001). URL http://dx.doi.org/10.1016/S0002-9440(10)64051-5.

[15] Osmand, A. P. *et al.* Characterization of C-reactive protein and the complement subcomponent C1t as homologous proteins displaying cyclic pentameric symmetry (pentraxins). *Proceedings of the National Academy of*

Sciences of the United States of America **74**, 739–43 (1977). URL https://doi.org/10.1073/pnas.74.2.739.

[16] Potempa, L. A., Yao, Z.-Y., Ji, S.-R., Filep, J. G. & Wu, Y. Solubilization and purification of recombinant modified C-reactive protein from inclusion bodies using reversible anhydride modification. *Biophysics Reports* **1**, 18–33 (2015). URL http://link.springer.com/10.1007/s41048-015-0003-2.

[17] Swanson, S. J. & Mortensen, R. F. Binding and immunological properties of a synthetic peptide corresponding to the phosphorylcholine-binding region of C-reactive protein. *Molecular Immunology* **27**, 679–687 (1990). URL https://doi.org/10.1016/0161-5890(90)90011-N.

[18] Chan, D. & Ng, L. L. Biomarkers in acute myocardial infarction. *BMC Medicine* **8**, 34 (2010). URL https://doi.org/10.1186/1741-7015-8-34.

[19] Wolfe Barry, J. A., Barth, J. H. & Howell, S. J. Cardiac troponins: Their use and relevance in anaesthesia and critical care medicine. *Continuing Education in Anaesthesia, Critical Care and Pain* **8**, 62–66 (2008).

[20] Wu, A. H. B. Cardiac troponin: Friend of the cardiac physician, foe to the cardiac patient. *Circulation* **114**, 1673–1675 (2006).

[21] Al-Otaiby, M. A., Al-Amri, H. S. & Al-Moghairi, A. M. The clinical significance of cardiac troponins in medical practice. *Journal of the Saudi Heart Association* **23**, 3–11 (2011). URL http://dx.doi.org/10.1016/j.jsha.2010.10.001.

[22] Wells, S. M. & Sleeper, M. Cardiac troponins. *Journal of Veterinary Emergency and Critical Care* **18**, 235–245 (2008). URL https://doi.org/10.1111/j.1476-4431.2008.00307.x.

[23] Parmacek, M. S. & Solaro, R. J. Biology of the troponin complex in cardiac myocytes. *Progress in cardiovascular diseases* **47**, 159–76 (2004). URL https://doi.org/10.1016/j.pcad.2004.07.003.

[24] Andersen, A.-D., Poulsen, K. A., Lambert, I. H. & Pedersen, S. F. HL-1 mouse cardiomyocyte injury and death after simulated ischemia and reperfusion: roles of pH, Ca2+-independent phospholipase A2, and Na+/H+ ex-

change. *American journal of physiology. Cell physiology* **296**, C1227–C1242 (2009).

[25] Streng, A. S. *et al.* Cardiac troponin in ischemic cardiomyocytes: Intracellular decrease before onset of cell death. *Experimental and Molecular Pathology* **96**, 339–345 (2014). URL http://dx.doi.org/10.1016/j.yexmp.2014.02.012.

[26] Yoo, E. M., Chintalacharuvu, K. R., Penichet, M. L. & Morrison, S. L. Myeloma expression systems. *Journal of Immunological Methods* **261**, 1–20 (2002). URL http://linkinghub.elsevier.com/retrieve/pii/S0022175901005592.

[27] Kern, W. The evolution of silicon wafer cleaning technology. *Journal of The Electrochemical Society* **137**, 1887–1892 (1990). URL http://jes.ecsdl.org/content/137/6/1887.abstract.

[28] Moldovan, A. *et al.* Simple cleaning and conditioning of silicon surfaces with uv/ozone sources. *Energy Procedia* **55**, 834 – 844 (2014). URL http://www.sciencedirect.com/science/article/pii/S1876610214012910.

[29] Alves, N. J., Kiziltepe, T. & Bilgicer, B. Oriented surface immobilization of antibodies at the conserved nucleotide binding site for enhanced antigen detection. *Langmuir* **28**, 9640–9648 (2012). URL https://pubs.acs.org/doi/10.1021/la301887s.

[30] Aissaoui, N., Bergaoui, L., Landoulsi, J., Lambert, J. F. & Boujday, S. Silane layers on silicon surfaces: mechanism of interaction, stability, and influence on protein adsorption. *Langmuir* **28**, 656–665 (2012). URL http://www.ncbi.nlm.nih.gov/pubmed/22107153.

[31] Zeng, X., Xu, G., Gao, Y. & An, Y. Surface wettability of (3-Aminopropyl)triethoxysilane self-assembled Monolayers. *Journal of Physical Chemistry B* **115**, 450–454 (2011). URL https://pubs.acs.org/doi/abs/10.1021/jp109259b.

[32] Gunda, N. S. K., Singh, M., Norman, L., Kaur, K. & Mitra, S. K. Optimization and characterization of biomolecule immobilization on silicon substrates using (3-aminopropyl)triethoxysilane (APTES) and glutaraldehyde linker. *Applied*

Surface Science **305**, 522–530 (2014). URL http://dx.doi.org/10.1016/j.apsusc.2014.03.130.

[33] Trilling, A. K., Harmsen, M. M., Ruigrok, V. J., Zuilhof, H. & Beekwilder, J. The effect of uniform capture molecule orientation on biosensor sensitivity: Dependence on analyte properties. *Biosensors and Bioelectronics* **40**, 219–226 (2013). URL http://dx.doi.org/10.1016/j.bios.2012.07.027.

[34] Vashist, S. K., Dixit, C. K., MacCraith, B. D. & O'Kennedy, R. Effect of antibody immobilization strategies on the analytical performance of a surface plasmon resonance-based immunoassay. *Analyst* **136**, 4431–4436 (2011). URL http://xlink.rsc.org/?DOI=c1an15325k.

[35] Yuan, Y., Yin, M., Qian, J. & Liu, C. Site-directed immobilization of antibodies onto blood contacting grafts for enhanced endothelial cell adhesion and proliferation. *Soft Matter* **7**, 7207–7216 (2011). URL http://dx.doi.org/10.1039/C1SM05086A.

[36] Liu, Y., Guo, C. X., Hu, W., Lu, Z. & Li, C. M. Sensitive protein microarray synergistically amplified by polymer brush-enhanced immobilizations of both probe and reporter. *Journal of Colloid and Interface Science* **360**, 593–599 (2011). URL http://dx.doi.org/10.1016/j.jcis.2011.05.030.

[37] Park, J. W., Cho, I. H., Moon, D. W., Paek, S. H. & Lee, T. G. ToF-SIMS and PCA of surface-immobilized antibodies with different orientations. *Surface and Interface Analysis* **43**, 285–289 (2011). URL https://onlinelibrary.wiley.com/doi/abs/10.1002/sia.3440.

[38] Bergström, G. & Mandenius, C. F. Orientation and capturing of antibody affinity ligands: Applications to surface plasmon resonance biochips. *Sensors and Actuators, B: Chemical* **158**, 265–270 (2011). URL https://doi.org/10.1016/j.snb.2011.06.017.

[39] Bereli, N., Sener, G., Yavuz, H. & Denizli, A. Oriented immobilized anti-LDL antibody carrying poly(hydroxyethyl methacrylate) cryogel for cholesterol removal from human plasma. *Materials Science and Engineering C* **31**, 1078–1083 (2011). URL https://doi.org/10.1016/j.msec.2011.03.008.

[40] Balevicius, Z. *et al.* Evaluation of intact- and fragmented-antibody based immunosensors by total internal reflection ellipsometry. *Sensors and Actuators, B: Chemical* **160**, 555–562 (2011). URL http://dx.doi.org/10.1016/j.snb.2011.08.029.

[41] Baio, J. E., Cheng, F., Ratner, D. M., Stayton, P. S. & Castner, D. G. Probing orientation of immobilized humanized anti-lysozyme variable fragment by time-of-flight secondary-ion mass spectrometry. *Journal of Biomedical Materials Research - Part A* **97 A**, 1–7 (2011). URL https://onlinelibrary.wiley.com/doi/abs/10.1002/jbm.a.33025.

[42] Della Ventura, B., Schiavo, L., Altucci, C., Esposito, R. & Velotta, R. Light assisted antibody immobilization for bio-sensing. *Biomedical Optics Express* **2**, 3223 (2011). URL https://www.osapublishing.org/boe/abstract.cfm?uri=boe-2-11-3223.

[43] Huy, T. Q. *et al.* A novel biosensor based on serum antibody immobilization for rapid detection of viral antigens. *Talanta* **86**, 271–277 (2011). URL http://dx.doi.org/10.1016/j.talanta.2011.09.012.

[44] Chen, H., Huang, J., Lee, J., Hwang, S. & Koh, K. Surface plasmon resonance spectroscopic characterization of antibody orientation and activity on the calixarene monolayer. *Sensors and Actuators, B: Chemical* **147**, 548–553 (2010). URL http://dx.doi.org/10.1016/j.snb.2010.03.033.

[45] Chaudhary, S. *et al.* Controlled short-linkage assembly of functional nanoobjects. *Applied Surface Science* **300**, 22–28 (2014). URL http://linkinghub.elsevier.com/retrieve/pii/S0169433214002402.

[46] Piehler, J., Brecht, A., Valiokas, R., Liedberg, B. & Gauglitz, G. A high-density poly(ethylene glycol) polymer brush for immobilization on glass-type surfaces. *Biosensors and Bioelectronics* **15**, 473–481 (2000). URL https://doi.org/10.1016/S0956-5663(00)00104-4.

[47] Han, Y., Mayer, D., Offenhäusser, A. & Ingebrandt, S. Surface activation of thin silicon oxides by wet cleaning and silanization. *Thin Solid Films* **510**, 175–180 (2006). URL https://doi.org/10.1016/j.tsf.2005.11.048.

[48] Zhang, Q., Huang, R. & Guo, L.-H. One-step and high-density protein immobilization on epoxysilane-modified silica nanoparticles. *Science Bulletin* **54**, 2620–2626 (2009). URL http://link.springer.com/10.1007/s11434-009-0210-7.

[49] Wang, Z. H. & Jin, G. Silicon surface modification with a mixed silanes layer to immobilize proteins for biosensor with imaging ellipsometry. *Colloids and Surfaces B: Biointerfaces* **34**, 173–177 (2004). URL https://doi.org/10.1016/j.colsurfb.2003.12.012. 9809069v1.

[50] Cheng, S. *et al.* Field effect transistor biosensor using antigen binding fragment for detecting tumor marker in human serum. *Materials* **7**, 2490–2500 (2014). URL https://www.mdpi.com/1996-1944/7/4/2490.

[51] Vedrenne, C. & Arnaud, J. Whispering-gallery modes of dielectric resonators. *IEE Proceedings H Microwaves, Optics and Antennas* **129**, 183 (1982). URL http://digital-library.theiet.org/content/journals/10.1049/ip-h-1.1982.0037.

[52] Karimi, E., Zito, G., Piccirillo, B., Marrucci, L. & Santamato, E. Hypergeometric-Gaussian Modes **32**, 3053–3055 (2007). URL http://dx.doi.org/10.1364/OL.32.003053. 0712.0782.

[53] Wu, Y. *et al.* A unique ka-band measurement system based on quasi-optical dielectric resonator technology for studying small superconducting samples. *IEEE Transactions on Applied Superconductivity* **23**, 0–3 (2013). URL https://ieeexplore.ieee.org/document/6384691.

[54] Krupka, J., Tobar, M. E., Hartnett, J. G., Cros, D. & Le Floch, J. M. Extremely high-Q factor dielectric resonators for millimeter-wave applications. *IEEE Transactions on Microwave Theory and Techniques* **53**, 702–711 (2005). URL https://ieeexplore.ieee.org/document/1393215.

[55] Zychowicz, T., Krupka, J. & Mazierska, J. Measurements of conductivity of thin gold films at microwave frequencies employing resonant techniques. *Asia-Pacific Microwave Conference Proceedings, APMC* **1**, 572–574 (2006). URL https://ieeexplore.ieee.org/document/4429490.

[56] Yang, J., Giessen, H. & Lalanne, P. Simple analytical expression for the peak-frequency shifts of plasmonic resonances for sensing. *Nano Letters* **15**, 3439–3444 (2015). URL https://pubs.acs.org/doi/10.1021/acs.nanolett.5b00771.

[57] Protsenko, I. A., Barannik, A. A., Cherpak, N. T. & Kharchenko, M. S. Radiation Losses of Sapphire WGM Resonators : Effects of Dielectric Disk Shape 960–963 (2015).

[58] Barannik, A. A. *et al.* Contactless exploration of graphene properties using millimeter wave response of WGM resonator. *Applied Physics Letters* **113** (2018). URL https://aip.scitation.org/doi/10.1063/1.5041335.

[59] Protsenko, I. A. *et al.* Accurate permittivity characterization of liquids by means of WGM resonator with microfluidic. *Proceedings - 2013 International Kharkov Symposium on Physics and Engineering of Microwaves, Millimeter and Submillimeter Waves, MSMW 2013* 538–540 (2013). URL https://ieeexplore.ieee.org/document/6622132.

[60] Gubin, A. I. *et al.* Whispering-gallery mode resonator technique for characterization of small volumes of biochemical liquids in microfluidic channel. *2011 41st European Microwave Conference* 615–618 (2011).

[61] Gubin, A. I. *et al.* Whispering-Gallery-Mode Resonator Technique With Microfluidic Channel for Permittivity Measurement of Liquids. *IEEE Transactions on Microwave Theory and Techniques* **63**, 2003–2009 (2015). URL https://ieeexplore.ieee.org/document/7097100.

[62] Rae, C. D. & Williams, S. R. Glutathione in the human brain: Review of its roles and measurement by magnetic resonance spectroscopy. *Analytical Biochemistry* **529**, 127 – 143 (2017). URL http://www.sciencedirect.com/science/article/pii/S0003269716304341.

[63] Monacelli, F., Acquarone, E., Giannotti, C., Borghi, R. & Nencioni, A. Vitamin c, aging and alzheimer‘s disease. *Nutrients* **9** (2017). URL http://www.mdpi.com/2072-6643/9/7/670.

[64] Naumova, N. *et al.* Microwave characterization of low-molecular-weight antioxidant specific biomarkers. *Biochimica et Biophys-*

ica Acta (BBA) - General Subjects **1863**, 226–231 (2019). URL https://doi.org/10.1016/j.bbagen.2018.10.013https://linkinghub.elsevier.com/retrieve/pii/S0304416518303349.

[65] Basey-Fisher, T. H. *et al.* Microwave debye relaxation analysis of dissolved proteins: Towards free-solution biosensing. *Applied Physics Letters* **99**, 233703 (2011). URL https://doi.org/10.1063/1.3665413.

[66] Su, J. Label-Free biological and chemical sensing using whispering gallery mode optical resonators: Past, present, and future. *Sensors (Switzerland)* **17**, 1–18 (2017). URL https://www.mdpi.com/1424-8220/17/3/540.

[67] Xavier, J., Vincent, S., Meder, F. & Vollmer, F. Advances in optoplasmonic sensors - Combining optical nano/microcavities and photonic crystals with plasmonic nanostructures and nanoparticles. *Nanophotonics* **7**, 1–38 (2018). URL https://doi.org/10.1515/nanoph-2017-0064.

[68] Kim, D. C. & Dunn, R. C. Integrating whispering gallery mode refractive index sensing with capillary electrophoresis separations using phase sensitive detection. *Analytical Chemistry* **88**, 1426–1433 (2016). URL https://doi.org/10.1021/acs.analchem.5b04187. PMID: 26651379.

[69] Poghossian, A. *et al.* Field-effect sensors with charged macromolecules: Characterisation by capacitance-voltage, constant-capacitance, impedance spectroscopy and atomic-force microscopy methods. *Biosensors and Bioelectronics* **22**, 2100–2107 (2007).

[70] Lee, C.-S., Kim, S. K. & Kim, M. Ion-sensitive field-effect transistor for biological sensing. *Sensors* **9**, 7111–7131 (2009). URL http://www.mdpi.com/1424-8220/9/9/7111.

[71] Gilles, S. & Jülich, F. Chemical modification of silicon surfaces for the application in soft lithography. *Berichte-Forschungszentrum Julich Jul* **4249** (2007). URL http://juser.fz-juelich.de/record/57361.

[72] Sun, C. Q., Pan, L. K., Fu, Y. Q., Tay, B. K. & Li, S. Size Dependence of the 2p-Level Shift of Nanosolid Silicon. *The Journal of Physical Chemistry B* **107**, 5113–5115 (2003). URL http://pubs.acs.org/doi/abs/10.1021/jp0272015.

[73] Iwata, S. & Ishizaka, A. Electron spectroscopic analysis of the SiO2/Si system and correlation with metal-oxide-semiconductor device characteristics. *Journal of Applied Physics* **79**, 6653–6713 (1996). URL https://aip.scitation.org/doi/10.1063/1.362676.

[74] Thiviyanathan, V. & Gorenstein, D. G. Aptamers and the next generation of diagnostic reagents. *Proteomics. Clin. Appl.* **6**, 563–573 (2012). URL https://www.ncbi.nlm.nih.gov/pubmed/23090891.

[75] Dorraj, G. S., Rassaee, M. J., Latifi, A. M., Pishgoo, B. & Tavallaei, M. Selection of dna aptamers against human cardiac troponin i for colorimetric sensor based dot blot application. *Journal of Biotechnology* **208**, 80 – 86 (2015). URL http://www.sciencedirect.com/science/article/pii/S0168165615002230.

[76] Hlukhova, H., Menger, M., Offenhäusser, A. & Vitusevich, S. Highly Sensitive Aptamer-Based Method for the Detection of Cardiac Biomolecules on Silicon Dioxide Surfaces. *MRS advances* **3**, 1535 – 1541 (2018). URL https://doi.org/10.1557/adv.2018.332.

[77] Hauser, J. R. & Ahmed, K. Characterization of ultra-thin oxides using electrical C-V and I-V measurements. In *American Institute of Physics Conference Series*, vol. 449 of *American Institute of Physics Conference Series*, 235–239 (1998). URL https://aip.scitation.org/doi/abs/10.1063/1.56801.

[78] Hulme, E. C. & Trevethick, M. A. Ligand binding assays at equilibrium: validation and interpretation. *British Journal of Pharmacology* **161**, 1219–1237. URL https://bpspubs.onlinelibrary.wiley.com/doi/abs/10.1111/j.1476-5381.2009.00604.x.

[79] Jo, H. *et al.* Electrochemical aptasensor of cardiac troponin i for the early diagnosis of acute myocardial infarction. *Analytical Chemistry* **87**, 9869–9875 (2015). URL https://doi.org/10.1021/acs.analchem.5b02312.

[80] Shen, S.-H., Cheng, H., Kao, T.-Y., Chen, M.-J. & Lin, C.-T. Silicon-based Multi-nanowire Biosensor with High-k Dielectric and Stacked Oxide Sensing Membrane for Cardiac Troponin I Detection. *Procedia Engineering* **87**, 648–651 (2014). URL http://dx.doi.org/10.1016/j.proeng.2014.11.571.

[81] Zhou, W., Dai, X. & Lieber, C. M. Advances in nanowire bioelectronics. *Reports Prog. Phys.* **80**, 016701 (2017). URL http://stacks.iop.org/0034-4885/80/i=1/a=016701?key=crossref.e7b8cb3e7b09303b0a4e664d543f900b.

[82] Choi, B. *et al.* A bottom-gate silicon nanowire field-effect transistor with functionalized palladium nanoparticles for hydrogen gas sensors. *Solid-State Electronics* **114**, 76 – 79 (2015). URL http://www.sciencedirect.com/science/article/pii/S0038110115002282.

[83] Gao, A. *et al.* Enhanced Sensing of Nucleic Acids with Silicon Nanowire Field Effect Transistor Biosensors. *Nano Letters* **12**, 5262–5268 (2012). URL http://pubs.acs.org/doi/10.1021/nl302476h.

[84] Mu, L. *et al.* Silicon nanowire field-effect transistors - a versatile class of potentiometric nanobiosensors. *IEEE Access* **3**, 287–302 (2015). URL https://ieeexplore.ieee.org/document/7089167.

[85] Sciuto, E. L. *et al.* Functionalization of Bulk SiO2 Surface with Biomolecules for Sensing Applications: Structural and Functional Characterizations. *Chemosensors* **6**, 59 (2018). URL http://www.mdpi.com/2227-9040/6/4/59.

[86] Pachauri, V. & Ingebrandt, S. Biologically sensitive field-effect transistors: from isfets to nanofets. *Essays In Biochemistry* **60**, 81–90 (2016). URL http://essays.biochemistry.org/content/60/1/81.

[87] Tabata, O., Asahi, R., Funabashi, H., Shimaoka, K. & Sugiyama, S. Anisotropic etching of silicon in tmah solutions. *Sensors and Actuators A: Physical* **34**, 51 – 57 (1992). URL http://www.sciencedirect.com/science/article/pii/092442479280139T.

[88] Pud, S. *et al.* Liquid and back gate coupling effect: toward biosensing with lowest detection limit. *Nano Lett.* **14**, 578–84 (2014). URL http://www.ncbi.nlm.nih.gov/pubmed/24392670.

[89] Knopfmacher, O. *et al.* Nernst limit in dual-gated Si-nanowire FET sensors. *Nano letters* **10**, 2268–74 (2010). URL http://pubs.acs.org/doi/abs/10.1021/nl100892yhttp://www.ncbi.nlm.nih.gov/pubmed/20499926.

[90] Kaisti, M. Detection principles of biological and chemical fet sensors. *Biosensors and Bioelectronics* **98**, 437 – 448 (2017). URL http://www.sciencedirect.com/science/article/pii/S0956566317304517.

[91] Gao, N. *et al.* General strategy for biodetection in high ionic strength solutions using transistor-based nanoelectronic sensors. *Nano Letters* **15**, 2143–2148 (2015). URL https://pubs.acs.org/doi/10.1021/acs.nanolett.5b00133.

[92] Kim, K. S., Lee, H.-S., Yang, J.-A., Jo, M.-H. & Hahn, S. K. The fabrication, characterization and application of aptamer-functionalized Si-nanowire FET biosensors. *Nanotechnology* **20**, 235501 (2009). URL http://www.ncbi.nlm.nih.gov/pubmed/19448297.

[93] Lee, M.-H. Quantitative measurements of C-reactive protein using silicon nanowire arrays. *International Journal of Nanomedicine* **3**, 117 (2008). URL https://www.ncbi.nlm.nih.gov/pmc/articles/PMC2526356/.

[94] Kwon, S. M., Kang, G. B., Kim, Y. T., Kim, Y.-H. & Ju, B.-K. In-situ detection of c-reactive protein using silicon nanowire field effect transistor. *Journal of Nanoscience and Nanotechnology* **11**, 1511–1514 (2011). URL https://www.ncbi.nlm.nih.gov/pubmed/21456224.

[95] De, A., van Nieuwkasteele, J., Carlen, E. T. & van den Berg, A. Integrated label-free silicon nanowire sensor arrays for (bio)chemical analysis. *Analyst* **138**, 3221–3229 (2013). URL http://dx.doi.org/10.1039/C3AN36586G.

[96] Ridker, P. M., Hennekens, C. H., Buring, J. E. & Rifai, N. C-reactive protein and other markers of inflammation in the prediction of cardiovascular disease in women. *New England Journal of Medicine* **342**, 836–843 (2000). URL https://doi.org/10.1056/NEJM200003233421202.

[97] Ridker, P. M., Rifai, N., Rose, L., Buring, J. E. & Cook, N. R. Comparison of c-reactive protein and low-density lipoprotein cholesterol levels in the prediction of first cardiovascular events. *New England Journal of Medicine* **347**, 1557–1565 (2002). URL https://doi.org/10.1056/NEJMoa021993.

[98] Salvo, P. *et al.* Sensors and biosensors for c-reactive protein, temperature and ph, and their applications for monitoring wound healing: A review. *Sensors* **17** (2017). URL http://www.mdpi.com/1424-8220/17/12/2952.

[99] Kim, K. *et al.* Silicon nanowire biosensors for detection of cardiac troponin I (cTnI) with high sensitivity. *Biosensors and Bioelectronics* **77**, 695–701 (2016). URL http://dx.doi.org/10.1016/j.bios.2015.10.008.

[100] Takeda, S., Yamashita, A., Maeda, K. & Maéda, Y. Structure of the core domain of human cardiac troponin in the Ca2+-saturated form. *Nature* **424**, 35 (2003). URL https://doi.org/10.1038/nature01780.

[101] Park, J.-S. *et al.* A highly sensitive and selective diagnostic assay based on virus nanoparticles. *Nature nanotechnology* **4**, 259–264 (2009). URL https://www.nature.com/articles/nnano.2009.38.

[102] Lin, T.-W. *et al.* Label-free detection of protein-protein interactions using a calmodulin-modified nanowire transistor. *Proceedings of the National Academy of Sciences of the United States of America* **107**, 1047–52 (2010). URL http://www.pnas.org/cgi/doi/10.1073/pnas.0910243107.

[103] Kutovyi, Y. *et al.* Origin of noise in liquid-gated Si nanowire troponin biosensors. *Nanotechnology* **29**, 175202 (2018). URL http://stacks.iop.org/0957-4484/29/i=17/a=175202?key=crossref.5524eea3ffec8221168f432ac8fe59fa.

[104] Chiang, P.-L. *et al.* Nanowire transistor-based ultrasensitive virus detection with reversible surface functionalization. *Chemistry - An Asian Journal* **7**, 2073–2079. URL https://onlinelibrary.wiley.com/doi/abs/10.1002/asia.201200222.

[105] Zadorozhnyi, I. *et al.* Towards pharmacological treatment screening of cardiomyocyte cells using Si nanowire FETs. *Biosensors and Bioelectronics* **137**, 229–235 (2019). URL https://doi.org/10.1016/j.bios.2019.04.038https://linkinghub.elsevier.com/retrieve/pii/S095656631930329X.

[106] Maybeck, V. *et al.* Boron-doped nanocrystalline diamond microelectrode arrays monitor cardiac action potentials. *Adv. Healthc. Mater.* **3**, 283–289 (2014). URL http://doi.wiley.com/10.1002/adhm.201300062.

[107] Hofmann, B. *et al.* Light induced stimulation and delay of cardiac activity. *Lab Chip* **10**, 2588 (2010). URL http://xlink.rsc.org/?DOI=c003091k.

[108] Natarajan, A. R., Rong, Q., Katchman, A. N. & Ebert, S. N. Intrinsic cardiac catecholamines help maintain beating activity in neonatal rat cardiomyocyte cultures. *Pediatr. Res.* **56**, 411–7 (2004). URL http://www.ncbi.nlm.nih.gov/pubmed/15333759.

[109] Besl, B. & Fromherz, P. Transistor array with an organotypic brain slice: field potential records and synaptic currents. *European Journal of Neuroscience* **15**, 999–1005. URL https://onlinelibrary.wiley.com/doi/abs/10.1046/j.1460-9568.2002.01943.x.

[110] Cohen-Karni, T., Qing, Q., Li, Q., Fang, Y. & Lieber, C. M. Graphene and Nanowire Transistors for Cellular Interfaces and Electrical Recording. *Nano Lett.* **10**, 1098–1102 (2010). URL http://pubs.acs.org/doi/abs/10.1021/nl1002608.

[111] Kireev, D. & Offenhäusser, A. Graphene & two-dimensional devices for bioelectronics and neuroprosthetics. *2D Mater.* **5** (2018). URL http://iopscience.iop.org/article/10.1088/2053-1583/aad988.

[112] Bendali, A. *et al.* Purified Neurons can Survive on Peptide-Free Graphene Layers. *Adv. Healthc. Mater.* **2**, 929–933 (2013). URL http://doi.wiley.com/10.1002/adhm.201200347.

[113] Kandel, E. R., Schwartz, J. H. & Jessel, T. M. *Principles of Neural Science* (2000).

[114] Zdebik, A. A., Wangemann, P. & Jentsch, T. J. Potassium ion movement in the inner ear: Insights from genetic disease and mouse models. *Physiology* **24**, 307–316 (2009). URL https://doi.org/10.1152/physiol.00018.2009.

[115] Lu, J. *et al.* Effects of ischaemia-mimetic factors on isolated rat ventricular myocytes. *Experimental Physiology* **90**, 497–505 (2005). URL https://physoc.onlinelibrary.wiley.com/doi/full/10.1113/expphysiol.2004.029421.

[116] Chiong, M. *et al.* Cardiomyocyte death: Mechanisms and translational implications. *Cell Death and Disease* **2**, e244–11 (2011). URL http://dx.doi.org/10.1038/cddis.2011.130.

[117] Minasian, S. M., Galagudza, M. M., Dmitriev, Y. V., Kurapeev, D. I. & Vlasov, T. D. Myocardial protection against global ischemia with Krebs-Henseleit buffer-based cardioplegic solution. *Journal of Cardiothoracic Surgery* **8**, 1–9 (2013). URL https://www.ncbi.nlm.nih.gov/pubmed/23547937.

[118] Ginsberg, M. D. Neuroprotection for ischemic stroke: Past, present and future. *Neuropharmacology* **55**, 363–389 (2008). URL https://linkinghub.elsevier.com/retrieve/pii/S0028390807003814.

[119] Buja, L. M. Myocardial ischemia and reperfusion injury. *Cardiovascular Pathology* **14**, 170–175 (2005). URL https://doi.org/10.1016/j.carpath.2005.03.006.

[120] Abney, S. & Raton, B. Book Reviews. *Journal of Orthodontics* **39**, 139–139 (2012). URL http://www.tandfonline.com/doi/full/10.1179/1465312512Z.00000000017.

[121] Baer, S. Acute myocardial infarctions. *JAMA: The Journal of the American Medical Association* **118**, 248 (1942). URL https://jamanetwork.com/journals/jama/article-abstract/253344.

[122] Kutty, R. S., Jones, N. & Moorjani, N. Mechanical Complications of Acute Myocardial Infarction. *Cardiology Clinics* **31**, 519–531 (2013). URL http://dx.doi.org/10.1016/j.ccl.2013.07.004.

[123] Ingebrandt, S., Vu, X. T., Eschermann, J. F., Stockmann, R. & Offenhäusser, A. Top-Down Processed SOI Nanowire Devices for Biomedical Applications. *ECS Transaction* **35**, 3–15 (2011). URL http://ecst.ecsdl.org/content/35/7/3.abstract.

[124] Kireev, D. *et al.* Graphene transistors for interfacing with cells: towards a deeper understanding of liquid gating and sensitivity. *Sci. Rep.* **7**, 6658 (2017). URL http://www.nature.com/articles/s41598-017-06906-5.

[125] Kireev, D. *et al.* High throughput transfer technique: Save your graphene. *Carbon N. Y.* **107** (2016). URL https://doi.org/10.1016/j.carbon.2016.05.058.

Author's List of Publications

Y. Kutovyi, I. Zadorozhnyi, V. Handziuk, **H. Hlukhova**, N. Boichuk, M. Petrychuk, S. Vitusevich. Temperature-Dependent Noise and Transport in Silicon Two-Layer Nanowire FETs. *Phys. Status Solidi B*, 1800636 (2019).

N. Naumova, **H. Hlukhova**, A. Barannik, A. Gubin, I. Protsenko, N. Cherpak, S. Vitusevich. Microwave characterization of low-molecular-weight antioxidant specific biomarkers. *Biochimica et Biophysica Acta* **1863**(1), 226-231 (2019).

H. Hlukhova, M. Menger, S. Vitusevich and A. Offenhaeusser. Highly Sensitive Aptamer-Based Method for the Detection of Cardiac Biomolecules on Silicon Dioxide Surfaces. *MRS Advances*, **3**(27), 1535-1541 (2018).

Y. Kutovyi, I. Zadorozhnyi, V. Handziuk, **H. Hlukhova**, N. Boichuk, M. Petrychuk, S. Vitusevich. Liquid-Gated Two-Layer Silicon Nanowire FETs: Evidence of Controlling Single-Trap Dynamic Processes. *Nano Lett.* **18**, 7305-7313 (2018).

N. Naumova, **H. Hlukhova**, S. Vitusevich, A. Barannik, A. Gubin, I. Protsenko, N. Cherpak. Real-time microwave characterization of low-molecular-weight antioxidant biomarkers. *DPG Spring Meeting 2018*, Berlin, 2018.

Y. Kutovyi, I. Zadorozhnyi, **H. Hlukhova**, V. Handzuik, M. Petrychuk, A. Ivanchuk, and S. Vitusevich. Origin of Noise in Liquid-Gated Silicon Nanowire Troponin Biosensors. *Nanotechnology* **29**(17), 175202 (2018).

A. Gubin, I. Protsenko, A. Barannik, **H. Hlukhova**, N. Cherpak and S. Vitusevich. Liquids Microwave Characterization Technique Based on Quartz WGM Resonator with Microfluidic Chip. *2018 48th European Microwave Conference (EuMC)*, Madrid, 2018, pp. 206-209.

I. Zadorozhnyi, J. Li, **H. Hlukhova**, V. Handzuik, Y. Kutovyi, M. Petrychuk, S. Vitusevich and A. Offenhaeusser. Effect of Gamma Irradiation on Dynamics of Charge Exchange process between Single Trap and Nanowire. *Small* **14**(2), 1702516 (2017).

I. Zadorozhnyi, **H. Hlukhova**, Y. Kutovyi, M. Petrychuk, V. Sydoruk, V. Handzuik and S. Vitusevich. Analysis of Charge States in GaN-based Nanoribbons Using Transport and Noise Studies. *2017 International Conference on Noise and Fluctuations (ICNF)*, Vilnius, 2017, 17031842.

I. Zadorozhnyi, Y. Kutovyi, **H. Hlukhova**, M. Petrychuk and S. Vitusevich. Hooge‘s parameter in Si-NW FET with different widths. *2017 International Conference on Noise and Fluctuations (ICNF)*, Vilnius, 2017, 17047078.

Y. Kutovyi, I. Zadorozhnyi, **H. Hlukhova**, M. Petrychuk and S. Vitusevich. Low-Frequency Noise in Si-NW FETs for electrical biosensing. *2017 International Conference on Noise and Fluctuations (ICNF)*, Vilnius, 2017, 17047119.

I. Protsenko, A. Barannik, N. Cherpak, M. Kharchenko, **H. Hlukhova** and S. Vitusevich. Radiation Losses of Sapphire WGM Resonators: Effects of Disk Shape. *2015 European Microwave Conference (EuMC)*, Paris, 2015, pp. 960-963.